

2

AD-A267 260



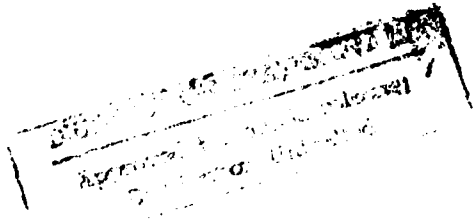
ACOUSTIC WAVES IN BAFFLED  
LIQUID-PROPELLANT ROCKET ENGINES  
(AFOSR Grant No. 91-0171)

Final Report  
Submitted to

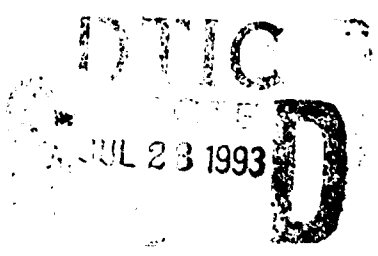
Air Force Office of Scientific Research  
AFOSR/NA  
Bolling AFB, D. C. 20332-0001

Prepared  
by

Vigor Yang, M. W. Yoon, and J. M. Wicker  
Department of Mechanical Engineering  
The Pennsylvania State University  
University Park, PA 16801



May 1993



93-16917



93



## SUMMARY

This document serves as the final report of the research program, "Acoustic Waves in Complicated Geometries and Their Interactions with Liquid-Propellant Droplet Combustion," sponsored by the Air Force Office of Scientific Research, Grant No. 91-0171. The major purpose of this research is to develop a comprehensive theoretical analysis within which multi-dimensional acoustic waves in baffled combustors and their mutual coupling with liquid-propellant combustion can be properly treated.

During this report period from March 14, 1991 to May 14, 1993, a unified linear and nonlinear acoustic analysis for baffled combustion chambers has been developed. The linear investigation proceeds by solving a generalized wave equation derived from the conservation equation for a two-phase mixture, utilizing perturbation expansions of flow variables. Nonlinear acoustic study of baffled chambers is conducted by means of an approximate analysis which takes into account second- and third-order nonlinear gas dynamics and combustion response. Results suggest three important effects of baffles on transverse modes of combustion instability. First, transverse waves can be longitudinalized inside baffle compartments. This may decouple combustion response from oscillatory motions if the processes near the injector face are sensitive to transverse variations in pressure. Second, severe restriction of the transverse component of acoustic velocity fluctuations is observed in baffle compartments. This may be key in stabilizing systems with velocity-sensitive combustion. Third, the frequency of oscillation is decreased with the addition of baffles, in agreement with experiments. One potentially destabilizing effect of baffles is the observed pressure concentration at the injector face. Pressure

sensitive processes in this region may enhance instability. Limit cycles are observed for both two- and three-dimensional baffled chambers. Their most remarkable characteristic is high-frequency modulation of the limit cycle amplitude. In addition, the conditions for the existence of spinning oscillations are treated in depth.

Some of the results obtained from this research have led to the following two publications.

1. Yang, V., Yoon, M.W., and Wicker, J.M., "Nonlinear Pressure Oscillations in Baffled Combustion Chambers," AIAA Paper 93-0233, presented at the 31st AIAA Aerospace Sciences Meeting, January 1993.
2. Yang, V., Yoon, M.W., and Wicker, J.M., "Linear and Nonlinear Acoustic Waves in Liquid-Propellant Rocket Engines," presented at the First International Symposium on Liquid-Rocket Combustion Instability, January 1993.

Accession For	
NTIS	DTIC
USDA	NSA
State	DOE
By	Date
A-1	

## TABLE OF CONTENTS

	Page
LIST OF TABLES .....	vi
LIST OF FIGURES .....	vii
NOMENCLATURE .....	x
ACKNOWLEDGEMENTS .....	xiv
Chapter 1 INTRODUCTION .....	1
1.1 General Features of Combustion Instabilities in Liquid-Propellant Rocket Engines .....	3
1.2 Mechanisms of Baffle Operation .....	9
1.3 Research Objective .....	11
1.4 Early Works on Experimental and Theoretical Investigation of Baffles .....	12
1.5 Early Works on Nonlinear Combustion Instability .....	17
1.6 Thesis Outline .....	19
Chapter 2 THEORETICAL FORMULATION .....	21
2.1 Conservation Equations for a Two-Phase Flow .....	21
2.2 Nonlinear Wave Equation .....	27
Chapter 3 LINEAR ACOUSTIC WAVES IN BAFFLED CHAMBERS .....	30
3.1 Linear Acoustic Oscillations .....	30
3.2 Two-Dimensional Baffled Chamber .....	36
3.2.1 Acoustic Field in Baffle Compartments .....	36
3.2.2 Acoustic Field in Main Combustion Chamber .....	39
3.2.3 Matching of Acoustic Fields in Baffle Compartments and Main Chamber .....	40

3.3	Three-Dimensional Baffled Chamber .....	44
3.3.1	Acoustic Field in Baffle Compartments .....	44
3.3.2	Acoustic Field in Main Combustion Chamber .....	46
3.3.3	Matching of Acoustic Fields in Baffle Compartments and Main Chamber .....	47
3.4	Results and Discussion of Linear Acoustic Analysis .....	50
3.4.1	in Two-Dimensional Baffled Chamber .....	50
3.4.2	in Three-Dimensional Baffled Chamber .....	64
Chapter 4	NONLINEAR SPINNING TRANSVERSE OSCILLATIONS ...	70
4.1	Problem Formulation .....	70
4.2	Nonlinear Spinning Oscillations .....	77
4.2.1	First Tangential Mode .....	78
4.2.2	First Tangential/First Radial Modes .....	83
4.2.3	First Tangential/Second Tangential Modes .....	88
4.2.4	First Tangential/First Radial/Second Tangential Modes ..	95
Chapter 5	NONLINEAR ACOUSTIC WAVES IN BAFFLED CHAMBERS .....	102
5.1	Nonlinear Acoustic Oscillations .....	102
5.2	Results and Discussion of Nonlinear Acoustic Analysis .....	110
Chapter 6	CONCLUSIONS AND FUTURE WORK .....	122
REFERENCES	.....	125
APPENDIX	CHARACTERISTIC EQUATION FOR THE FREQUENCY	131

## LIST OF TABLES

	Page
Table 1 History of Combustion Instabilities in Liquid-Propellant Rocket Engines .....	2
Table 2 Values of $C_{nm}$ for a Two-Dimensional Chamber .....	113
Table 3 Values of $C_{nm}$ for a Three-Dimensional Chamber .....	113

## LIST OF FIGURES

	Page
Figure 1.1 Particle Trajectories for Standing and Spinning Tangential Modes .....	7
Figure 1.2 Schematic of a Liquid-Propellant Rocket Engine with Injector-Face Baffles .....	10
Figure 3.1 Schematic of a Three-Dimensional Baffled Combustion Chamber .....	31
Figure 3.2 Schematic of a Two-Dimensional Baffled Combustion Chamber .....	37
Figure 3.3 Comparison between Analytical and Numerical Results for Acoustic Pressure Contours in Baffled Chambers; $L_b = 0.4 H$ ...	51
Figure 3.4 Effect of Baffle Length on the Acoustic Pressure Field in a One-Baffle Chamber; the First Transverse Mode .....	53
Figure 3.5 Effect of Baffle Length on the Acoustic Pressure Field in a Two-Baffle Chamber; the First Transverse Mode .....	55
Figure 3.6 Effect of Baffle Length on the Acoustic Pressure Field in a Two-Baffle Chamber; the Second Transverse Mode .....	56
Figure 3.7 Acoustic Pressure and Velocity for the First Transverse Mode in a Two-Baffle Chamber .....	58
Figure 3.8 Effect of Baffle Length on the Acoustic Pressure Field (a) One-Baffle Chamber; the Second Transverse Mode (b) Two-Baffle Chamber; the Third Transverse Mode .....	59
Figure 3.9 Effect of Baffle Length on the Frequency of the First Transverse Mode; Two-Dimensional Chamber .....	61

Figure 3.10	Acoustic Velocity Field of the First Transverse Mode in a One-Baffle Chamber (a) Acoustic Vector Plot (b) Distributions of Transverse Acoustic Velocity at Various Axial Locations .....	63
Figure 3.11	Effect of Baffle Length on the Frequency of the First Tangential Mode; Three-Dimensional Chamber .....	65
Figure 3.12	Acoustic Pressure Contours of the First Tangential Mode at Various Cross Sections for a Three-Dimensional Baffled Chamber .....	67
Figure 3.13	Acoustic Velocity Vectors of the First Tangential Mode at Various Cross Sections for a Three-Dimensional Baffled Chamber .....	69
Figure 4.1	An Example Showing the Existence of Stable Limit Cycle; the First Tangential Mode .....	82
Figure 4.2	An Example Showing the Existence of Stable Limit Cycle; the First Tangential/First Radial Modes .....	87
Figure 4.3	Illustration of the Necessary and Sufficient Conditions for Stable Limit Cycles; the First Tangential/Second Tangential Modes .....	96
Figure 4.4	An Example Showing the Existence of Stable Limit Cycle; the First Tangential/Second Tangential Modes .....	97
Figure 4.5	An Example Showing the Existence of Stable Limit Cycle; the First Tangential/First Radial/Second Tangential Modes ...	101
Figure 5.1	Block Diagram Showing the Energy Transfer Relation among Modes .....	111

Figure 5.2	An Example Showing the Existence of Limit Cycle for Two-Dimensional Chamber; the First and Second Transverse Modes .....	115
Figure 5.3	An Example Showing the Existence of Limit Cycle for Three-Dimensional Chamber; the First Tangential/First Radial Modes .....	117
Figure 5.4	An Example Showing the Existence of Limit Cycle for Three-Dimensional Chamber; the First Tangential/Second Tangential Modes .....	118
Figure 5.5	An Example Showing the Existence of Limit Cycle for Three-Dimensional Chamber; the First Tangential/Second Tangential/First Radial Modes ...	119
Figure 5.6	Time History of the Pressure Amplitude for Three-Dimensional Chamber; the First Tangential/Second Tangential/First Radial Modes ...	120

## NOMENCLATURE

$A_I$	Injector admittance
$A_m^\mu$	Eigenfunction expansion coefficients in a two-dimensional chamber
$A_N$	Nozzle admittance
$A_{Nt}^\mu$	Eigenfunction expansion coefficients in a three-dimensional chamber
$A_{nij}$	Nonlinear Parameters defined by Eq. (5.12)
$\bar{a}$	Speed of sound in mixture
$B_n^c$	Eigenfunction expansion coefficients in a two-dimensional chamber
$B_{nij}$	Nonlinear Parameters defined by Eq. (5.12)
$B_{nt}^c$	Eigenfunction expansion coefficients in a three-dimensional chamber
$C_{mb}$	Equation (3.25)
$C_{nc}$	Equation (3.34)
$C_{nm}$	Equation (5.7)
$\bar{C}_p$	Mass-averaged specific heat at constant pressure
$\bar{C}_v$	Mass-averaged specific heat at constant volume
$D_{ni}$	Linear Parameters defined by Eqs. (4.13a) and (5.12a)
$E_{ni}$	Linear Parameters defined by Eqs. (4.13b) and (5.12b)
$E_n^2$	Euclidian norm
$e_0$	Specific total internal energy of gas phase
$\mathcal{E}_n$	Acoustic energy density of $n$ th mode
$F_n$	Forcing function
$f_1$	Equation (2.32a)
$f_2$	Equation (2.32b)
$f_3$	Equation (2.32c)

$\mathcal{F}$	Force of interaction between liquid and gas phases
$G_m$	Equation (3.46a)
$G_{mn}$	Equation (4.11)
$G_{N1s}$	Equation (3.69a)
$H$	Height of chamber
$H_n$	Equation (3.46b)
$H_{mn}$	Equation (4.11)
$H_{nt}$	Equation (3.69b)
$h_0$	Stagnation enthalpy of liquid phase
$h_1$	Equation (2.30a)
$h_2$	Equation (2.30b)
$h_3$	Equation (2.30c)
$\Delta H_v$	Heat of combustion
$I_{mn}$	Equation (4.11)
$J$	Bessel function
$k$	Wave number
$L$	Length of chamber
$M$	Mach number
$N$	Number of baffle blades
$\mathbf{n}$	Unit outward normal vector
$p$	Pressure
$Q$	Rate of energy release
$\mathbf{q}$	Heat flux vector
$q_{mb,1}, q_{mb,2}$	Equation (3.23)
$q_{nc,1}, q_{nc,2}$	Equation (3.32)
$R$	Radius of chamber
$\bar{R}$	Mass-averaged gas constant
$r_n$	Time-varying amplitude of limit cycle
$\mathcal{R}$	Combustion response function

$S$	Cross section area
$T$	Temperature
$t$	Time
$u$	Velocity
$V$	Volume
$v$	Radial component of acoustic velocity
$w$	Tangential component of acoustic velocity
$W$	Equation (2.21)
$X$	Phase difference, Eqs. (4.23), (4.47), (4.65) and (4.96)
$X_1$	Phase difference, Eq. (4.96)
$Y$	Phase difference, Eqs. (4.47), (4.65) and (4.96)
$Y_1$	Phase difference, Eq. (4.96)
$Z$	Phase difference, Eqs. (4.65) and (4.96)

#### *Greek Symbols*

$\alpha_n$	Growth constant of $n$ th mode
$\alpha_{ni}$	Linear coupling parameter
$\bar{\gamma}$	Specific heat ratio
$\zeta_n$	Axial distribution function, Eq. (3.1)
$\eta_n$	Amplitude of $n$ th mode
$\theta_m$	Modified wave number, Eq. (3.16)
$\theta_n$	Frequency shift of $n$ th mode
$\theta_{ni}$	Linear coupling parameter
$\lambda$	Eigenvalue for stable limit cycles
$\nu_n$	Frequency modulation, Eq. (4.25)
$\xi_n$	Phase, Eq. (4.25)
$\rho$	Density
$\vec{\tau}_v$	Viscous stress tensor
$\Phi$	Dissipation function

$\phi_n$	Phase
$\psi_n$	Normal mode function
$\Omega$	Complex frequency
$\Omega_{ni}$	Frequency differences, Eqs. (4.47) and (4.65)
$\omega_n$	Radian frequency of $n$ th normal mode
$\dot{\omega}_l$	Burning rate

### Superscripts

$(\bar{\quad})$	Mean
$(\quad)'$	Fluctuation
$(\hat{\quad})$	Complex amplitude of acoustic quantity
$(\quad)^c$	Main chamber
$(\quad)^\mu$	$\mu$ th baffle compartment
$(\tilde{\quad})$	Dominant mode

### Subscripts

$(\quad)_0$	Values in a limit cycle
$(\quad)_b$	Baffle compartment
$(\quad)_c$	Main chamber
$(\quad)_{cR}$	Combustion response
$(\quad)_g$	Gas phase
$(\quad)_l$	Liquid phase
$(\quad)_p$	Pressure coupled-
$(\quad)_v$	Radial velocity coupled-
$(\quad)_w$	Tangential velocity coupled-

## CHAPTER 1

### INTRODUCTION

Combustion instabilities have long plagued liquid-propellant rocket engine designers and developers. The essential cause of this problem is the high rate of oscillatory energy release within a volume in which energy losses are relatively small. If compensating influences acting to attenuate the oscillations are weak, then unsteady motions in a combustor may give rise to excessive chamber pressures and heat transfer rates, resulting in decreased performance at best, or catastrophic failure of the engine at worst. Table 1 (assembled from Refs. 1-8) presents some practical examples in which pressure oscillations have had serious impact on specific engine development programs. As this table shows, high frequency instabilities have remained an insidious problem throughout the entire history of U.S. rocket programs, particularly in liquid oxygen (LOX)/RP-1 and chemical storable systems.

Because instabilities arise from sources entirely internal to the system, an external observer perceives the result as the dynamical behavior of a self-excited system capable of exciting and sustaining oscillations over a broad range of frequencies. Typically, the oscillations grow out of a reinforcement between the inherent noise of the combustion process and the numerous characteristic acoustic modes of the feed-system/combustion chamber combination, rather than from any external influence.

Three inherent characteristics of the combustion chamber environment provide ideal conditions for the initiation of instability. First, combustion chambers are

Table 1. History of Combustion Instabilities in Liquid-Propellant Rocket Motors

PROJECT	MOTOR	ORGANIZATION CONTRACTOR	PROPELLANTS	THRUST (lbf)	PERFORMANCE (%)	CHAMBER PRESSURE (psia)	INSTABILITY ENCOUNTERED	STABILIZATION DERIVES	INJECTOR TYPE	REFERENCES
Mercury	Redstone A-7	NASA/USAF Rocketdyne	Alcohol LOX	78,000	95.0	315.0	-	-	Like doublet	1,6
Mercury	Atlas MA-5	NASA/USAF/Rocketdyne	RP-1 LOX	165,000	95.5	577.0	Not with baffles	7 compartment copper baffles	Like doublet and triplet	1,6
Gemini	Titan II 1st Stage	USAF/NASA Aerojet	50% N <sub>2</sub> H <sub>4</sub> } A50 50% UDMH } N <sub>2</sub> O <sub>4</sub>	236,400	97.2	783.0	POGO Mode ±2.5g	Standpipe inserted into N <sub>2</sub> O <sub>4</sub> feedlines	Like doublet	2,5,6,8
Gemini	Titan II 2nd Stage	USAF/NASA Aerojet	50% N <sub>2</sub> H <sub>4</sub> } A50 50% UDMH } N <sub>2</sub> O <sub>4</sub>	100,000	97.4	827.0	Longitudinal mode	7 compartment copper baffles	Quadrant	2,5,6,8
Apollo Saturn IB S-1B stage	H-1	NASA Rocketdyne	RP-1 LOX	204,300	97.3	705.0	Instability pre-sent during bomb tests	7 compartment copper baffles	Like doublet and triplet	3,6
Apollo Saturn IB S-1VB Saturn V S-1I, 1VB	J-2	NASA Rocketdyne	LH <sub>2</sub> LOX	230,000	98.6	686.0	1800 Hz First Tangential Mode	3 compartment aluminum baffles	Coaxial	3,6,7,8
Apollo Saturn V S-1C	F-1	NASA/Rocketdyne	RP-1 LOX	1,552,000	93.8	1128.0	500 Hz First Tangential Mode	13 compartment copper baffles	Like doublet	3,6,7,8
Apollo/Lunar module ascent	LMAE	NASA Bell	50% N <sub>2</sub> H <sub>4</sub> } A50 50% UDMH } N <sub>2</sub> O <sub>4</sub>	3,500	97.1	120.0	First Radial Third Tangential modes	3 compartment baffles	Unlike doublet	3,4,6,7,8
Apollo Lunar descent VTR-10	LMDE	NASA TRW	50% N <sub>2</sub> H <sub>4</sub> } A50 50% UDMH } N <sub>2</sub> O <sub>4</sub>	9,850	96.2	104.0	-	3 compartment aluminum baffles	Coaxial pintle	3,4,6,7,8
Space Shuttle	SSME	NASA Rocketdyne	LH <sub>2</sub> LOX	408,750	99.6	3,277	-	7 compartment baffles	Coaxial	6

almost entirely closed. This condition favors excitation of unsteady motions over a broad range of frequencies. Second, the internal processes tending to attenuate unsteady motions are weak relative to the driving energy, thus providing circumstances that allow sustained modes of instability. Third, and perhaps most important, the energy required to drive unsteady motions is an exceedingly small fraction of the heat released by combustion. In typical instances, less than 0.1 percent of the heat release is sufficient to initiate and sustain the severe pressure oscillation.<sup>9</sup>

### **1.1 General Features of Combustion Instability in Liquid-Propellant Rocket Engines**

Compared with solid rocket motors and other liquid-fueled propulsion systems, the combustion processes within a liquid rocket engine have several characteristics that produce distinctive differences in the pressure oscillations observed. First, except for highly volatile fuels, such as hydrogen and methane, most propellants are injected into the chamber as a spray of liquid droplets and undergo a sequence of atomization, vaporization, mixing, and combustion processes. Each process may serve as either a driving or damping mechanism, depending on its sensitivity to the local flow oscillations. Second, the combustion chamber is directly connected to the propellant supply system through the injectors. Interactions between the unsteady motions in the chamber and the oscillatory behavior of the feedlines may affect the stability characteristics of the engine. Third, the occurrence of instabilities depends intimately on the operating sequence of the engine. For example, the sudden liquefaction or gasification of liquid propellant in the feedline during the

transient start-up and shut-down phases may trigger instabilities;<sup>10</sup> hence, design criteria must make provision for transient as well as steady-state mechanisms for initiating combustion instabilities. Fourth, the propellant also frequently serves as the coolant for a regeneratively cooled system. The heat transfer and other engine performance requirements may have a strong impact on the stability characteristics through their influences on the propellant flow conditions in the injection system. A well known example is the triggering of instabilities in the J-2 engine by decreasing the gaseous hydrogen injection temperature.<sup>11</sup>

Combustion instabilities are a particularly complex phenomenon for which several modes of oscillations have been commonly observed. They are often classified according to their spatial structures and driving mechanisms as low, intermediate, and high frequency instabilities. Low frequency instabilities, also known as 'chugging' or POGO instabilities, received much attention during the 1950s and 1960s as a serious problem with the Jupiter, Thor, Atlas, and Titan launch vehicles. The underlying mechanism lies in the coupling between the fluid dynamics in the combustion chamber and the propellant supply system. Other effects such as propellant pump cavitation and gas entrapment in the feedline may also contribute to driving POGO instabilities. Characteristically, this mode corresponds to the vibrations of a Helmholtz resonator, with a frequency range between a few and several hundred Hz. Since techniques for preventing their occurrence are now well established,<sup>12,13</sup> 'chugging' instabilities are no longer a serious design problem.

Intermediate frequency instabilities, also known as 'buzz', are more prevalent in medium size engines (25,000 to 250,000 N thrust) than in large engines. They are

evidenced by a growing coherence of combustion noise at a particular frequency. Two sources may give rise to their occurrence. The first is associated with the interactions between the unsteady combustion in the chamber and a specific portion of the propellant feed system. The second arises from the coupling between entropy waves and acoustic motions in the chamber. It is well established that for bi-propellant rocket engines, fluctuations of the reactant mixture ratio may lead to entropy waves, which then interact with the nonuniform mean velocity field in the nozzle to generate acoustic waves. In general, the 'buzz' instabilities are more noisy than damaging, with the amplitude of pressure oscillation rarely greater than 5 percent of the mean chamber pressure, although in some cases detrimental high frequency oscillations can be triggered by this mode. Comprehensive discussions of 'buzz' instabilities and entropy waves are given in Refs. 14 and 15.

High frequency instabilities, often called 'screeching' or 'screaming,' are the most common and vexatious, and are characterized by reinforcing the interactions between acoustic oscillations and combustion processes inside the thrust chamber. Depending upon the response of combustion processes to chamber oscillations, energy can be fed into acoustic waves such that their amplitude grows. The most destructive result of these large amplitude pressure excursions is the increased heat transfer to the chamber walls and injector face. Burn-throughs can occur in a few seconds or less, causing complete failure of the engine.

This type of instability is usually characterized by well defined frequencies and mode shapes that correspond closely to the classical acoustic modes of the chamber. Fundamental modes of high frequency instabilities are thus categorized as longitudinal and transverse, according to the spatial character of unsteady

motions within the combustion chamber. Longitudinal modes propagate along in the axial direction of the chamber, with no variation in the transverse plane and are usually observed in chambers with large length-to-diameter ratios. Transverse modes exhibit no axial variation in oscillatory behavior, but propagate radially and tangentially along planes perpendicular to the chamber axis. For contemporary rocket engine designs in which the chamber aspect ratio and nozzle contraction ratio are relatively small, pure transverse modes of oscillations dominate because of the effective damping of the longitudinal oscillations by the nozzle and the distribution of the combustion along the chamber. For this reason, combined modes comprised of the superposition of longitudinal and transverse modes are also rarely observed in typical liquid rocket engines. Furthermore, longitudinal modes are usually less destructive than transverse modes, so theoretical studies such as this one should fully address transverse modes of combustion instability.

Each transverse mode may exist in three forms: radial, standing tangential, and spinning tangential waves. The differences between standing and spinning tangential modes can be clearly seen in Fig. 1.1, which shows the particle trajectories for the standing and the spinning modes of oscillations in a simulated F-1 engine combustion chamber.<sup>16</sup> Particles move back and forth for the standing mode of oscillation, but have an epicyclic trajectory around the chamber in the tangential direction for the spinning mode of oscillation. The standing mode particle trajectory can be explained by the fact that the acoustic velocity varies oppositely in consecutive cycles with respect to the fixed pressure nodal surface. The situation is similar for the spinning modes of oscillation, except now the pressure nodal surfaces rotate with angular frequency corresponding to the modal frequency; therefore,

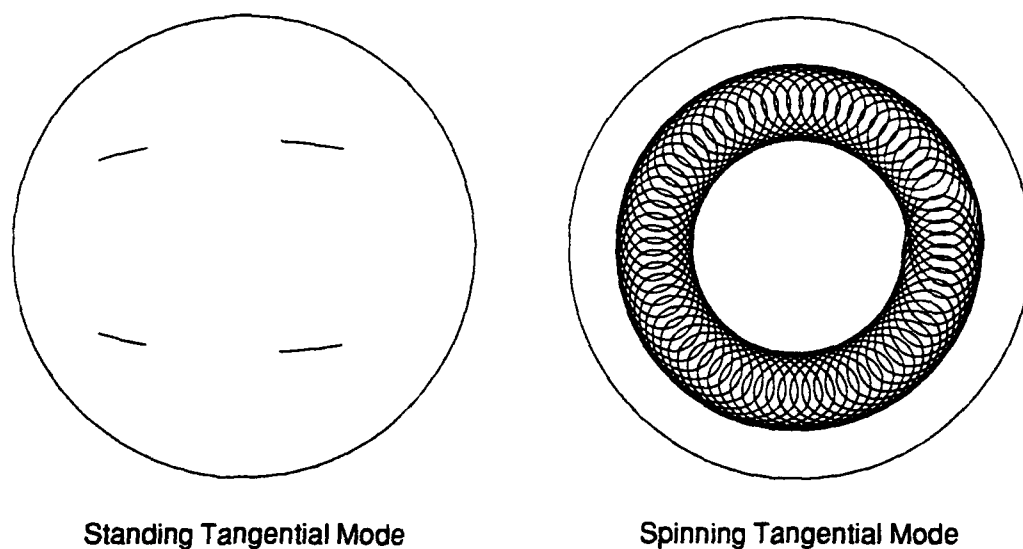


Figure 1.1 Particle Trajectories for Standing and Spinning Tangential Modes

particles move in a net circular fashion as time elapses. Spinning wave motions seem to be usually more detrimental because of their effectiveness in agitating gas molecules in transverse directions, thus enhancing heat transfer to the chamber walls. However, spinning waves may also be accompanied by an increase in combustion efficiency, presumably due to accelerated mixing processes. This phenomenon of increased efficiency accompanied by decreased stability is a common trade-off in rocket engine designs, and the ability to design for both efficiency and stability simultaneously represents one potential payoff for instability research.

Several possible mechanisms have been proposed that may be responsible for

driving the spinning mode of combustion instability. Of the various intermediate processes occurring during the combustion, atomization, vaporization, droplet interaction, mixing of the vaporized propellants and chemical kinetics are the most sensitive processes to the oscillations of velocity and pressure. For discussion purposes, the non-steady effects considered here can be divided into two groups: effects associated with atomization and vaporization, and effects related to the mixing process.

The atomization and jet breakup process, and its relationship to spray formation through pressure, temperature and velocity perturbations, can affect the energy release characteristics of the gas phase, and thus the stability of the combustor. The vaporization process that is directly related to the local pressure, temperature, and velocity, will be affected by oscillations in these quantities. Furthermore, there can be mixture ratio gradients in the vapor because of the stratification of the liquid spray in the liquid propellant injector. If the transverse acoustic field is imposed on such a spray, the vapor will be displaced relative to the droplet, causing mixture ratio oscillations in the vicinity of each vaporizing droplet. Hence, there will be an oscillation in the burning rate, which can couple with the acoustic field to produce a spinning mode of combustion instability.

When the vaporization rate becomes extremely high, it is possible that a droplet is heated rapidly through its critical temperature. With droplet shattering, clouds of the very fine secondary droplets are rapidly gasified. In such cases, the burning rate could be controlled by the rate of gas-phase mixing. Again, this oscillation of the burning rate is coupled with the transverse acoustic fields to generate the spinning mode of instability.

## 1.2 Mechanisms of Baffle Operation

To provide a cure for combustion instabilities, or to at least limit the amplitudes to acceptable values, passive control devices (such as injector-face baffles, acoustic absorbers, liners, cavities, and quarter-wave tubes) can be used. In particular, baffles can provide significant stabilizing effects on pressure oscillations, especially on spinning transverse modes of instability in liquid rocket engines, and have been widely used since 1954.<sup>17</sup> A typical configuration consists of flat plates extending into the chamber perpendicularly from the injector face, arranged in a radial and/or circumferential pattern, as shown in Fig. 1.2.

Three mechanisms have been proposed to explain successful elimination of instabilities by baffles. These are (1) the modification of acoustic properties, such as oscillation frequency and waveform, in combustion chambers; (2) the restriction of unsteady motions between baffle blades, and the subsequent protection of the sensitive mechanisms for instabilities; and (3) the damping of oscillations by vortex shedding, flow separation, and viscous dissipation. Specific examples of the first mechanism include reduction of the transverse pressure gradient near the injector face and the blocking of wave paths associated with certain modes. Spinning modes, for instance, are practically unheard of in baffled combustion chambers due to the baffle blade boundary conditions. The shielding function of baffles mentioned above helps to minimize coupling between parts of the combustion processes from oscillatory motions. This is important where velocity sensitivity is a concern, or where triggering of an instability in the baffle region is a possibility. The third mechanism of baffle operation—energy damping—can either attenuate the oscillations

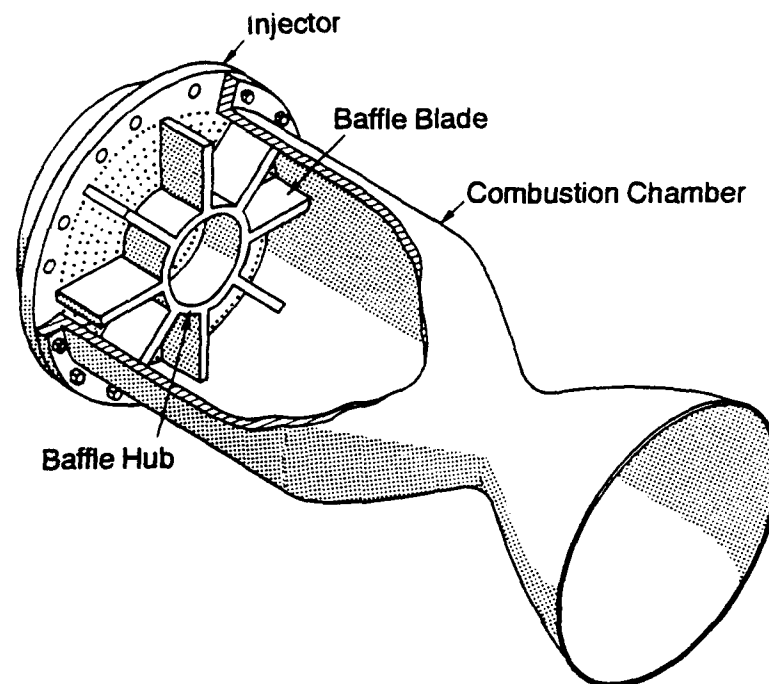


Figure 1.2 Schematic of a Liquid-Propellant Rocket  
Engine with Injector-Face Baffles

to within acceptable levels, or extract enough energy so that the reinforcing feedback between combustion and chamber acoustics is destroyed. It should be noted that it is possible that more than one mechanism operates at the same time in a baffled chamber, but some may dominate, depending on the specific engine parameters.

### 1.3 Research Objective

At a recent JANNAF workshop,<sup>18</sup> it was suggested that acoustic wave interaction in the baffled region is one of the most important parts in the study of combustion instability for liquid-propellant rocket engines. Because combustion instability is a consequence of the sensitivity of combustion processes to ambient flow oscillation, any realistic investigation into the engine stability behavior must accommodate a thorough treatment of the wave structure within the baffled combustion chamber. However, because of the complex nature of acoustic flow in the baffled region, the effects of baffles on wave motions have never been completely understood quantitatively. At present, there are no well-defined criteria for the selection of baffle configurations that will lead to the stable operation of an engine. As a result, most designs in use today are based on experiences with similar combustor configurations, propellant combinations, and operating conditions, thereby making the development of a new system a costly trial-and-error process.<sup>19</sup> Since injector-face baffles provide the most significant stabilization effects on pressure oscillations, a basic understanding of the oscillatory flow structure in that region appears to be a prerequisite in treating combustion instabilities in baffled liquid rocket engines.

The primary purpose of this work is to develop a theoretical analysis within which multi-dimensional acoustic waves in a baffled combustion chamber can be properly treated. Emphasis is placed on the combustion instability behavior of a baffled combustion chamber and the damping mechanisms of the baffle as described in the previous section.

Two other focuses in this study are the examination of nonlinear spinning wave motions in the unbaffled chamber, and the development of a nonlinear baffle analysis. The treatment of nonlinear spinning oscillations is crucial due to their relevance to baffle analysis and their frequent occurrence in practical rocket systems. Since no analytical work capable of treating nonlinear instability in baffled combustion chambers exists, introduction of such a methodology is highly desired and necessary if questions regarding nonlinear oscillations in physical chambers are to be addressed.

#### **1.4 Early Works on Experimental and Theoretical Investigation of Baffles**

Several experimental investigations have furnished results which lend valuable insight into the physical mechanisms of baffles. Experiments using non-reacting or 'cold' flow allow detailed research of fluid dynamic phenomena. Such a study was conducted by Wieber,<sup>20</sup> who examined the acoustic behavior of a 6-inch diameter cylindrical chamber under the influence of various baffle patterns, as well as different injector shapes, chamber lengths, and nozzle contraction angles. Decay coefficients of pressure oscillations corresponding to the first transverse mode were measured for unbaffled configurations and compared with internal surface area-to-volume ratios of the chamber. A positive correlation was discovered, suggesting that viscous wall losses were responsible for acoustic wave attenuation. When baffles were added, however, acoustic attenuation increased, but no correlation with the internal surface area was found. A more complicated damping mechanism than simple skin friction alone is required to fully explain the functions of baffles. Wieber further observed

that transverse modes were not only damped much more effectively by baffles than were longitudinal modes, but that the reduction in frequency from the unbaffled case was also much stronger, presumably due to relatively longer acoustic particle paths. Another cold flow investigation into the workings of baffles was initiated by Torda and Patel;<sup>21</sup> their experimental set-up elucidated vortical motion within a baffle cavity as a result of transverse flow across the open end of the cavity. The presence of circulating flow was clearly observed. Viscous damping within these vortices are thought to be a possible mechanism of baffle operation.

Empirical efforts based on reacting or 'hot' flow tests can yield data more readily applicable to actual rocket systems. Hannum et al.<sup>22</sup> experimented 17 different baffle designs for a hydrogen-oxygen engine with a 20,000 lbf thrust. In tests with at least a 2-inch baffle, stability was improved from the unbaffled chamber cases. For baffle compartments above a certain size,\* longer blade lengths were required for stability as the cavity dimension was increased. Below this size, all baffle configurations required the same blade length for stability, independent of compartment measurement. Interpretation of these data is not conclusive, but one possible explanation is that baffles protect the sensitive combustion zone from pressure and velocity fluctuations. Specifically, a certain blade length corresponding to the extent of the sensitive combustion zone could be required in all cases as a minimum for stability. For larger baffle cavities, a longer blade would be needed to impede the influence of the main chamber oscillation as acoustic waves

---

\* Compartment size was defined as the maximum compartment dimension measured parallel to the injector face. For cases of noncongruent cavities, an average weighted according to the number of each cavity style was used.

propagate more easily through larger areas. Although no relation between stability and internal surface area was presented, speculation of skin friction as a damping mechanism is prompted by some results. In one case, a 2-inch 3-blade radial baffle became unstable when it was burned and eroded back to 1.6 inches in length. An egg-crate configuration was stable for only 0.5 inch blades, perhaps due to the greater amount of surface area per length available for viscous loss. This conclusion is difficult to substantiate, since similar behavior is not consistently observed throughout the data.

Vincent et al.<sup>23</sup> conducted tests similar to those of Ref. 22, but used a smaller engine with storable propellants. Trends were found that mirrored the findings of Ref. 22 in spite of the differences in the experimental engine itself. A sweeping summary of important outcomes from several experimental baffle programs was completed by Hefner.<sup>24</sup> Among those surveyed were the Apollo Service Module Engine, First Stage and Second Stage Titan/Gemini, Transtage, and the Gemini Stability Improvement Program (GEMSIP). Specific findings are too numerous to mention here, but clearly illustrate the labyrinthine nature of baffle data reduction, as well as the dearth of fundamental interpretive understanding regarding baffles. Hence, it is essential to formulate a theoretical framework suitable for systematic treatment of baffles and appropriate deciphering of experimental baffle test results.

The first analytical treatment of acoustic motions in baffled chambers was undertaken by Reardon<sup>25</sup> in an effort to explain stability data from the GEMSIP program. The model considered three-dimensional oscillations in the main chamber with only one-dimensional longitudinal oscillations allowed in the baffle compartments. Combustion was assumed to be concentrated at the injector

face and modeled with a time-lag theory.<sup>26</sup> Matching of acoustic admittances in both regions at the interface provided sufficient conditions for determining the linear characteristics of the entire oscillatory field. This approximation yielded a moderately good estimate of the normal-mode frequency reduction caused by the baffles. However, since none of the continuity requirements on acoustic pressure, velocity, and energy flux across the interface were fulfilled, no accurate results of acoustic wave structures can be obtained. Implementation of this model in predicting engine stability is subject to question.

Oberg et al.<sup>27,28</sup> developed a more elaborate model that takes into account multi-dimensional wave motions in baffled cavities. The homogeneous Helmholtz equation for linear acoustic waves in the entire chamber formed the backbone of the analysis. The effect of mean flow was ignored, with the combustion response and nozzle damping treated as boundary conditions. Separate solutions were constructed using Green's functions for baffle compartments and the main chamber. The acoustic pressure and axial velocity in each region were then matched at the interface by means of a variational-iteration technique to determine the complex wave numbers of unsteady motions. Reasonable results were obtained for frequencies in two-dimensional chambers, but no solutions for cylindrical and annular chambers were reported due to some numerical difficulties. The major limitation of this theory is its erroneous prediction of engine stability behavior rendered by oversimplification of the physical processes. Essentially, this model treats an inviscid flowfield with concentrated combustion at the injector face. The resulting solution predicts a pressure rise in the forward region of the chamber, leading to a destabilizing influence of baffles in accordance with the Rayleigh

criterion.<sup>29</sup> A worsening of stability with increasing baffle length is obtained, rather than improvement as found experimentally. To circumvent this problem, an empirical modification that allows spatial variation of the combustion response factor along the injector face was later incorporated in the analysis to match experimental observations.<sup>30</sup>

In light of Oberg's findings, it is evident that alteration of acoustic wave structure by baffles alone can not explain the mechanisms responsible for baffle damping. The stabilizing influence must be associated with other means, such as viscous dissipation, vortex shedding, and distributed combustion response, which can override the driving effect of wave alteration. Baer and Mitchell<sup>31</sup> established a linear acoustic analysis, with emphasis placed on the fluid dynamic losses along the baffle blades. The formulation assumes concentrated combustion at the injector face within the confines of the time-lag theory, and solves for the acoustic velocity potential using an eigenfunction-expansion technique. The strong flow variations near the baffle tips are treated analytically by means of a matched asymptotic expansion method. A turbulent boundary layer is then ascertained in the vicinity of a finite thickness baffle. Although results considering viscous loss within this boundary layer yielded realistic acoustic decay rates, the conclusion that such dissipation is the dominant influence of baffles may be unjustified. For instance, vortical structures induced by acoustic motions along baffle blades and convected downstream into the main chamber may play an important role in dissipating energy and deserve a systematic investigation. Thorough investigation of these vortices using information gained from an acoustic study of baffled chambers is done by Wicker.<sup>32</sup>

## 1.5 Early Works on Nonlinear Combustion Instability

Spinning transverse modes of instability have very often been seen in the combustion chambers and it has been found to be related to the coupling of combustion processes with the oscillations in flow variables. Several analytical and experimental studies<sup>14,26,33,34</sup> have confirmed that the pressure-sensitive time lag concept ( $n - \tau$  model) can be applied to the analysis of transverse as well as longitudinal mode of high frequency instability. According to Reardon's experiment,<sup>35</sup> it is not sufficient to explain transverse modes of instability completely by the pressure sensitivity theory only. An additional combustion rate sensitivity must be considered for the transverse pressure oscillations. He found that the perturbations of radial and tangential velocity components have a strong influence on the combustion process rates in a manner analogous to that of pressure perturbations for the  $n - \tau$  model. Reardon et al.<sup>36</sup> predicted that the tangential velocity perturbation had a strong destabilizing effect on the spinning mode but had no effect on the standing mode of instability. Oberg et al.<sup>37</sup> also reached this conclusion—that simple pressure coupling cannot describe the spinning wave motions in the baffled combustion chamber and that some means of including the velocity coupling effect are necessary. Several investigators<sup>38,39</sup> addressed the importance of this mechanism. Thus, a conclusion can be drawn that velocity coupling as well as pressure coupling plays an important role in the spinning tangential mode of oscillations; therefore, the effects of velocity perturbation must be taken into account separately from the effect of pressure coupling in the nonlinear spinning analysis.

The analysis of nonlinear instability behavior in baffled combustion chambers is

another part of this work. Although studies that have been conducted in the pursuit of understanding nonlinear phenomena have not specifically addressed baffled combustion chambers, valuable building blocks have been laid in a foundation used in the current study. For instance, Sirignano and Crocco<sup>40</sup> first treated nonlinear wave motions in a combustor in 1964. Using a perturbation scheme with characteristic coordinates, they found that shock waves are the source of nonlinear losses responsible for the existence of the limit cycle. Crocco and Mitchell<sup>41</sup> treated the pure transverse mode in an annular chamber of very small radial extent using a nonlinear perturbation method with stretched coordinates. In their study, the unsteady combustion processes were represented by the sensitive time-lag ( $n - \tau$ ) model.

Zinn and co-workers<sup>42,43</sup> took a different approach to the problem of nonlinear transverse oscillations in a liquid-propellant rocket engine. Using Galerkin's method, with the expression of nonlinear solutions as an expansion of classical acoustic modes, they were able to derive a system of second-order ordinary differential equations governing the time-dependent amplitude of each acoustic mode. This system was then solved numerically to find the amplitudes and thus to predict the existence and behavior of limit cycles. Owing to certain assumptions, including the form assumed for the mean flow field, the extent to which the results may be valid for the other combustion systems could not be addressed. Furthermore, conclusions were based on numerical calculations of special problems, thereby obscuring possible generality.

Independent of the works cited above, the approximate analysis for nonlinear unsteady motion was developed by Culick<sup>44</sup> and allows expression of the compli-

cated nonlinear problem in terms of simpler equations. In addition to using the Galerkin's method and spatial averaging, the method of time-averaging developed by Krylov and Bogoliubov<sup>45</sup> was incorporated to produce a system of first-order ordinary differential equations for the time-varying modal amplitudes. This allowed for a more convenient analysis than the second-order equations provided by spatial averaging alone. By expanding the pressure field in terms of normal acoustic modes of the chamber, Culick showed that the nonlinear behavior could be equivalently represented by the equations for a system of nonlinear oscillators. Application of this work to motions in combustion chambers was discussed further by Culick,<sup>46</sup> with special emphasis on problems related to solid-propellant rocket motors. These general ideas have recently been summarized in Yang and Culick,<sup>47</sup> Kim,<sup>48</sup> and Culick and Yang.<sup>9</sup> This methodology is an invaluable tool for studying the effect of nonlinear gas dynamics on the formation of limit cycles, and is an important part of the present work.

## 1.6 Thesis Outline

In Chapter 2, a generalized wave equation for a two-phase mixture is derived utilizing perturbation expansions of flow variables to study the oscillatory flowfield in a baffled combustor. The formulation allows for acoustic wave motion, droplet vaporization and combustion, mean-flow/acoustics coupling, and two-phase interaction.

In Chapter 3, linear acoustic behavior is studied for two-dimensional rectangular and three-dimensional cylindrical baffled combustion chambers. The unsteady motions are expressed as a synthesis of transverse eigenfunctions of the acoustic

wave equation in the baffle compartments and the main chamber separately. The oscillatory fields in these two regions are matched at the interface by requiring continuity of acoustic pressure and axial velocity. This procedure eventually leads to solutions characterizing the unsteady flow structures in the entire chamber. Strong effects of baffles on the wave forms in a combustion chamber are clearly shown, and the effects of the baffles on stability are explained from these results.

In Chapter 4, nonlinear spinning transverse oscillations in a cylindrical unbaffled chamber are studied. Velocity effects are taken into consideration through a linear combustion response function. Using this approach, linear coupling between modes due to the combustion response is found to exist and to play an important role in the spinning modes of instability. The conditions for the existence and the stability of the limit cycle are also examined for several combinations of the spinning modes.

In Chapter 5, nonlinear acoustic analysis is performed for two-dimensional rectangular and three-dimensional cylindrical baffled combustion chambers. The full nonlinear solution for the baffled combustors is formulated in a manner analogous to Culick's approximate method. By expressing the nonlinear solution as a series of the linear modes obtained from the linear acoustic analysis, time-varying amplitudes can be assigned as coefficients in the series. When the entire expansion is substituted into the original nonlinear equation, integration over the chamber volume yields a set of second order ordinary differential equations in terms of the time-varying amplitudes. The solution of these equations gives information regarding nonlinear phenomenon such as limit cycles.

## CHAPTER 2

### THEORETICAL FORMULATION

Probably the most important fundamental characteristic of combustion instabilities is that for a first approximation they may be viewed as perturbations of classical acoustic motions. The principal perturbations are due to the combustion processes, the associated mean flow, and the boundary conditions imposed at the inlet and exhaust planes. Treating these perturbations within the framework of classical acoustics has been successful because the main departures, while crucial in defining the real problems, are often small perturbations in some sense. Therefore, it is desirable to seek the theoretical formulation that, when all perturbations vanish, reduces directly to a representation of classical wave motion in an enclosure. The analysis, therefore, starts with the establishment of a generalized wave equation for a two-phase mixture, with emphasis placed on the behavior of the liquid phase and its interaction with the gas flow, matters that are common to all liquid-fueled systems.

#### 2.1 Conservation Equations for a Two-Phase Flow

Analysis of flows in liquid rocket engines must be based on the conservation equations for a gas containing liquid droplets. A proper analysis must account for the differences between fuel and oxidizer and for a broad range of sizes of liquid droplets. However, because of uncertainties in the actual flow properties, it is

inappropriate to use a completely general formulation. To simplify the analysis, a two-phase mixture in the combustion chamber is assumed, with a mass-averaged gas comprising all gaseous species, including inert species, reactants, and combustion products. The liquid phase is treated as a mass-averaged fluid comprising fuel and/or oxidizer droplets. The complete set of conservation equations thus comprises those for the gas and those for the liquid; then, the equations are combined to form a set that governs the motions of a single medium. This idea was first applied to solid propellant rocket systems by Culick and Yang,<sup>9</sup> and this analysis follows their approach. The conservation equations for this two-phase mixture are given below.

Conservation of Mass (gas)

$$\frac{\partial \rho_g}{\partial t} + \nabla \cdot (\rho_g \mathbf{u}_g) = \dot{\omega}_l \quad (2.1)$$

Conservation of Mass (liquid)

$$\frac{\partial \rho_l}{\partial t} + \nabla \cdot (\rho_l \mathbf{u}_l) = -\dot{\omega}_l \quad (2.2)$$

Conservation of Momentum

$$\frac{\partial}{\partial t} (\rho_g \mathbf{u}_g + \rho_l \mathbf{u}_l) + \nabla \cdot (\rho_g \mathbf{u}_g \mathbf{u}_g + \rho_l \mathbf{u}_l \mathbf{u}_l) + \nabla p = \nabla \cdot \vec{\tau}_v \quad (2.3)$$

Conservation of Energy

$$\frac{\partial}{\partial t} (\rho_g e_{g0} + \rho_l h_{l0}) + \nabla \cdot (\rho_g \mathbf{u}_g e_{g0} + \rho_l \mathbf{u}_l h_{l0}) + \nabla \cdot (p \mathbf{u}_g) = Q + \nabla \cdot \mathbf{q} \quad (2.4)$$

where the subscripts  $g$  and  $l$  refer to mass-averaged quantities for gas and liquid phases, respectively. Evaporative and reactive conversion of mass from liquid to

the gas phase occurs at the rate  $\dot{\omega}_l$  (mass/sec-vol.). The viscous stress tensor is symbolized by  $\vec{\tau}_v$  and specific total internal energy of the gas and the liquid stagnation enthalpy are represented by  $e_{g0}$  and  $\hat{h}_{l0}$ , respectively. Furthermore,  $Q$  is the rate of energy released by homogeneous reactions in the gas phase (energy/sec-vol.), and  $\mathbf{q}$  represents the heat flux (conduction) vector.

With simple manipulations, the momentum and energy equations can be written

$$\rho_g \frac{\partial \mathbf{u}_g}{\partial t} + \rho_g \mathbf{u}_g \cdot \nabla \mathbf{u}_g + \nabla p = \nabla \cdot \vec{\tau}_v + \mathbf{F}_l - (\mathbf{u}_g - \mathbf{u}_l) \dot{\omega}_l \quad (2.5)$$

$$\begin{aligned} \rho_g C_v \frac{\partial T_g}{\partial t} + \rho_g C_v \mathbf{u}_g \cdot \nabla T_g + p \nabla \cdot \mathbf{u}_g = & Q + Q_l + \nabla \cdot \mathbf{q} + \Phi \\ & + (\hat{h}_{l0} - e_{g0}) \dot{\omega}_l \\ & + \mathbf{u}_g \cdot (\mathbf{u}_g - \mathbf{u}_l) \dot{\omega}_l + (\mathbf{u}_l - \mathbf{u}_g) \cdot \mathbf{F}_l \end{aligned} \quad (2.6)$$

where  $\Phi$  is the dissipation function. The force of interaction between the gas and liquid,  $\mathbf{F}_l$ , is defined as

$$\mathbf{F}_l = -\rho_l \left[ \frac{\partial \mathbf{u}_l}{\partial t} + \mathbf{u}_l \cdot \nabla \mathbf{u}_l \right] \quad (2.7)$$

and the heat release associated with chemical reactions and heat transfer between the phases,  $Q_l$ , is

$$Q_l = -\rho_l \left[ \frac{\partial \hat{h}_l}{\partial t} + \mathbf{u}_l \cdot \nabla \hat{h}_l \right] \quad (2.8)$$

The enthalpy of the liquid  $\hat{h}_l$  includes the heat release associated with the transformation from liquid to gas.

The density  $\rho$  for the mixture is defined as

$$\rho = \rho_g + \rho_l = \rho_g(1 + C_m) \quad (2.9)$$

and the liquid phase to the gas phase density ratio is given as  $C_m = \rho_l/\rho_g$ . Mass-averaged specific heats for the mixture are defined in the usual fashion.<sup>49,50</sup>

$$\bar{C}_v = \frac{C_v + C_m C_l}{1 + C_m}, \quad \bar{C}_p = \frac{C_p + C_m C_l}{1 + C_m} \quad (2.10)$$

The system of governing equations is completed by introducing the perfect-gas law for the mixture,

$$p = \rho \bar{R} T_g \quad (2.11a)$$

where  $\bar{R}$  is the gas constant for the mixture

$$\bar{R} = \bar{C}_p - \bar{C}_v \quad (2.11b)$$

Strictly,  $C_m$  must be treated as a dependent variable, since any nonuniformity in the mean flowfield, or unsteady motions, will cause the liquid droplets to slip relative to the gas. However, if the droplets are dispersed uniformly in the gas,  $C_m$  is approximately constant throughout the chamber. This assumption is true in the solid propellant rocket, but not as valid in liquid-fueled systems. But even though  $C_m$  may vary significantly, the mass-averaged thermodynamic properties are not greatly affected. Based on this assumption, therefore, the momentum and energy equations may be written in a more convenient form involving the mass-averaged properties of the two-phase mixture.

$$\rho \frac{\partial \mathbf{u}_g}{\partial t} + \rho \mathbf{u}_g \cdot \nabla \mathbf{u}_g + \nabla p = \nabla \cdot \boldsymbol{\tau}_v + \delta \mathbf{F}_l + \delta \mathbf{u}_l \dot{\omega}_l \quad (2.12)$$

$$\rho \bar{C}_v \left[ \frac{\partial T_g}{\partial t} + \mathbf{u}_g \cdot \nabla T_g \right] + p \nabla \cdot \mathbf{u}_g = Q + \delta Q_l + \nabla \cdot \mathbf{q} + \Phi + (\bar{h}_{l0} - e_{g0}) \dot{\omega}_l - \mathbf{u}_g \cdot \delta \mathbf{u}_l \dot{\omega}_l + \delta \mathbf{u}_l \cdot \mathbf{F}_l \quad (2.13)$$

where

$$\delta \mathbf{F}_l = -\rho_l \left[ \frac{\partial \delta \mathbf{u}_l}{\partial t} + \delta \mathbf{u}_l \cdot \nabla \mathbf{u}_g + \delta \mathbf{u}_l \cdot \nabla \mathbf{u}_l + \mathbf{u}_g \cdot \nabla \delta \mathbf{u}_l \right] \quad (2.14)$$

$$\delta Q_l = -\rho_l \left[ \frac{\partial \delta \bar{h}_l}{\partial t} + \delta \mathbf{u}_l \cdot \nabla \delta \bar{h}_l + \delta \mathbf{u}_l \cdot \nabla (C_l T_g) + \mathbf{u}_g \cdot \nabla \delta \bar{h}_l \right] \quad (2.15)$$

and  $\delta \mathbf{u}_l = \mathbf{u}_l - \mathbf{u}_g$ ,  $\delta \bar{h}_l = \bar{h}_l - C_l T_g$ . The energy equation (2.13) is combined with Eqs. (2.1) and (2.2) to give the equation for the pressure:

$$\begin{aligned} \frac{\partial p}{\partial t} + \mathbf{u}_g \cdot \nabla p + \bar{\gamma} p \nabla \cdot \mathbf{u}_g = \frac{\bar{R}}{\bar{C}_v} \left[ Q + \delta Q_l + \nabla \cdot \mathbf{q} + \Phi \right. \\ \left. + [(\bar{h}_{l0} - e_{g0}) - \mathbf{u}_g \cdot \delta \mathbf{u}_l] \dot{\omega}_l + \delta \mathbf{u}_l \cdot \mathbf{F}_l \right] \\ - \bar{R} T_g [\nabla \cdot (\rho_g \mathbf{u}_g) + \nabla \cdot (\rho_l \mathbf{u}_l)] \\ + \bar{R} T_g \mathbf{u}_g \cdot \nabla \rho + \rho \bar{R} T_g \nabla \cdot \mathbf{u}_g \end{aligned} \quad (2.16)$$

The chief purpose of the preceding exercise is to establish the forms of the equations that account for the presence of liquid, and that will provide a good first approximation for the speed of sound for the unperturbed motions, namely,

$$\bar{a} = \sqrt{\bar{\gamma} \bar{R} T_g} = \left[ \frac{\bar{\gamma}}{1 + C_m} \frac{p}{\rho_g} \right]^{\frac{1}{2}} \quad (2.17)$$

This formula explicitly shows that the propagation of small disturbances is governed by the elasticity of the gas (related to the pressure), and by the inertia of the two-phase mixture, represented by the factor  $(1 + C_m) \rho_g$ . Now the conservation equations can be expressed in a form emphasizing the view that combustion

instabilities are unsteady motions best regarded as perturbations of classical acoustics. The framework for the analysis is based on the sum of the continuity equations (2.1) and (2.2), the momentum equation (2.12), and the energy equation (2.16) written in terms of the pressure, with the source terms in a general form.

### Continuity Equation

$$\frac{\partial \rho}{\partial t} + \mathbf{u}_g \cdot \nabla \rho = \mathcal{W} \quad (2.18)$$

### Momentum Equation

$$\rho \frac{\partial \mathbf{u}_g}{\partial t} + \rho \mathbf{u}_g \cdot \nabla \mathbf{u}_g = -\nabla p + \mathcal{F} \quad (2.19)$$

### Energy Equation

$$\frac{\partial p}{\partial t} + \bar{\gamma} p \nabla \cdot \mathbf{u}_g = -\mathbf{u}_g \cdot \nabla p + \mathcal{P} \quad (2.20)$$

For the circumstances treated above,

$$\mathcal{W} = -\rho \nabla \cdot \mathbf{u}_g - \nabla \cdot (\rho_l \delta \mathbf{u}_l) \quad (2.21)$$

$$\mathcal{F} = \nabla \cdot \vec{\tau}_v + \delta \mathbf{F}_l + \delta \mathbf{u}_l \dot{\omega}_l \quad (2.22)$$

$$\begin{aligned} \mathcal{P} = \frac{\bar{R}}{\bar{C}_v} \left[ Q + \delta Q_l + \nabla \cdot \mathbf{q} + \Phi + [(\bar{h}_{l0} - e_{g0}) - \mathbf{u}_g \cdot \delta \mathbf{u}_l] \dot{\omega}_l \right. \\ \left. + \delta \mathbf{u}_l \cdot \mathbf{F}_l - \bar{C}_v T_g \nabla \cdot (\rho_l \delta \mathbf{u}_l) \right] \end{aligned} \quad (2.23)$$

## 2.2 Nonlinear Wave Equation

To derive a nonlinear wave equation governing the unsteady motions in the chamber, the dependent variables are first decomposed into mean and fluctuating parts,

$$\begin{aligned}
 \rho(\mathbf{r}, t) &= \bar{\rho}(\mathbf{r}) + \rho'(\mathbf{r}, t) \\
 \mathbf{u}_g(\mathbf{r}, t) &= \bar{\mathbf{u}}_g(\mathbf{r}) + \mathbf{u}'_g(\mathbf{r}, t) \\
 p(\mathbf{r}, t) &= \bar{p}(\mathbf{r}) + p'(\mathbf{r}, t) \\
 &\vdots
 \end{aligned}
 \tag{2.24}$$

It is assumed that the mean quantities are time-invariant and the fluctuating parts are small perturbations. Although variation of the mean quantities is typically small in actual rocket engines, spatial dependence is allowed for in the general formulation.

To the second order in fluctuations, Eqs. (2.11a), (2.18), (2.19) and (2.20) can be rewritten in their perturbed forms, giving a complete set of equations for the six unknowns:  $\rho'$ ,  $p'$ ,  $T'_g$ , and the three velocity components.

$$\frac{\partial \rho'}{\partial t} + \bar{\mathbf{u}}_g \cdot \nabla \rho' + \mathbf{u}'_g \cdot \nabla \bar{\rho} + \mathbf{u}'_g \cdot \nabla \rho' = \mathcal{W}'
 \tag{2.25}$$

$$\begin{aligned}
 \bar{\rho} \frac{\partial \mathbf{u}'_g}{\partial t} + \nabla p' &= -\bar{\rho} [\bar{\mathbf{u}}_g \cdot \nabla \mathbf{u}'_g + \mathbf{u}'_g \cdot \nabla (\bar{\mathbf{u}}_g + \mathbf{u}'_g)] \\
 &\quad - \rho' \frac{\partial \mathbf{u}'_g}{\partial t} + \mathcal{F}'
 \end{aligned}
 \tag{2.26}$$

$$\begin{aligned}
 \frac{\partial p'}{\partial t} + \bar{\gamma} \bar{p} \nabla \cdot \mathbf{u}'_g &= -\bar{\gamma} p' \nabla \cdot (\bar{\mathbf{u}}_g + \mathbf{u}'_g) - (\bar{\mathbf{u}}_g + \mathbf{u}'_g) \cdot \nabla p' \\
 &\quad - \mathbf{u}'_g \cdot \nabla \bar{p} + \mathcal{P}'
 \end{aligned}
 \tag{2.27}$$

$$p' = \bar{R}(\rho' \bar{T}_g + \bar{\rho} T'_g) + \bar{R} \rho' T'_g \quad (2.28)$$

Since acoustic waves manifest themselves by the presence of pressure oscillations, and pressure signals are easily measured and processed, the wave equation can be most conveniently written in terms of pressure fluctuation  $p'$ . Consequently, taking the time derivative of Eq. (2.27) and substituting Eq. (2.26) for  $\partial \mathbf{u}'_g / \partial t$  yields

$$\nabla^2 p' - \frac{1}{\bar{a}^2} \frac{\partial^2 p'}{\partial t^2} = h = h_1 + h_2 + h_3 \quad (2.29)$$

where

$$\begin{aligned} h_1 = & -\nabla \cdot \left[ \bar{\rho} (\bar{\mathbf{u}}_g \cdot \nabla \mathbf{u}'_g + \mathbf{u}'_g \cdot \nabla \bar{\mathbf{u}}_g) + \rho' \bar{\mathbf{u}}_g \cdot \nabla \bar{\mathbf{u}}_g \right] \\ & + \frac{1}{\bar{a}^2} \left[ \bar{\gamma} \frac{\partial p'}{\partial t} \nabla \cdot \bar{\mathbf{u}}_g + \frac{\partial \mathbf{u}'_g}{\partial t} \cdot \nabla \bar{p} + \bar{\mathbf{u}}_g \cdot \nabla \frac{\partial p'}{\partial t} \right] \end{aligned} \quad (2.30a)$$

$$\begin{aligned} h_2 = & -\nabla \cdot \left[ \bar{\rho} (\mathbf{u}'_g \cdot \nabla \mathbf{u}'_g) + \rho' \bar{\mathbf{u}}_g \cdot \nabla \mathbf{u}'_g + \rho' \frac{\partial \mathbf{u}'_g}{\partial t} \right] \\ & + \frac{1}{\bar{a}^2} \left[ \frac{\partial}{\partial t} (\mathbf{u}'_g \cdot \nabla p') + \bar{\gamma} \frac{\partial}{\partial t} (p' \nabla \cdot \mathbf{u}'_g) \right] \end{aligned} \quad (2.30b)$$

$$h_3 = \nabla \cdot \mathcal{F}' - \frac{1}{\bar{a}^2} \frac{\partial \mathcal{P}'}{\partial t} \quad (2.30c)$$

Here, the subscripts 1, 2 and 3 represent the linear effects, second order nonlinear gas dynamics, and the effect of source terms such as combustion and viscous dissipation, respectively.

Boundary conditions set on the gradient of  $p'$  are found by taking the scalar product of the outward normal vector with the perturbed momentum equation, and

then applying appropriate acoustic admittance functions along the surface of the field.

$$\mathbf{n} \cdot \nabla p' = -\mathbf{n} \cdot \mathbf{f} = -\mathbf{n} \cdot (\mathbf{f}_1 + \mathbf{f}_2 + \mathbf{f}_3) \quad (2.31)$$

where

$$\mathbf{f}_1 = \left[ \bar{\rho} \frac{\partial \mathbf{u}'_g}{\partial t} + \bar{\rho} [\bar{\mathbf{u}}_g \cdot \nabla \mathbf{u}'_g + \mathbf{u}'_g \cdot \nabla \bar{\mathbf{u}}_g] \right] \quad (2.32a)$$

$$\mathbf{f}_2 = \left[ \rho' \frac{\partial \mathbf{u}'_g}{\partial t} + \bar{\rho} (\mathbf{u}'_g \cdot \nabla \mathbf{u}'_g) \right] \quad (2.32b)$$

$$\mathbf{f}_3 = -\mathcal{F}' \quad (2.32c)$$

If all perturbations are absent, functions  $h$  and  $\mathbf{f}$  vanish, and the wave equation for the pressure in classical acoustics with the boundary condition for a rigid wall,  $\mathbf{n} \cdot \nabla p' = 0$ , is recovered.

## CHAPTER 3

### LINEAR ACOUSTIC WAVES IN BAFFLED CHAMBERS

The effects of baffles on acoustic motions in combustion chambers have not been understood quantitatively due to the complicated chamber geometry and associated difficulty of analyzing the flowfield in the baffle region. Since the elimination of combustion instabilities is the most important but least understood aspect of baffle design, this chapter deals with the linear stability behavior of baffled combustion chambers as well as the actual physical processes responsible for suppressing unsteady motions. The wave equation derived in Chapter 2 is applied to the baffled combustion chamber domain to investigate the acoustic wave characteristics for both two- and three-dimensional chambers.

#### 3.1 Linear Acoustic Oscillations

For a three-dimensional cylindrical baffled combustion chamber as shown in Fig. 3.1, a direct treatment of the wave equation, subject to the appropriate boundary conditions, appears to be formidable because of the geometric complexity imposed by the baffles. To facilitate the formulation, the form of the acoustic field solution is constructed in two parts: the baffle compartments and the main chamber. Since the spatial variations of acoustic motions are quite different in the baffle compartments and the main chamber, the oscillatory fields in these two regions are best treated separately. The eigenfunction expansion technique is adopted to solve

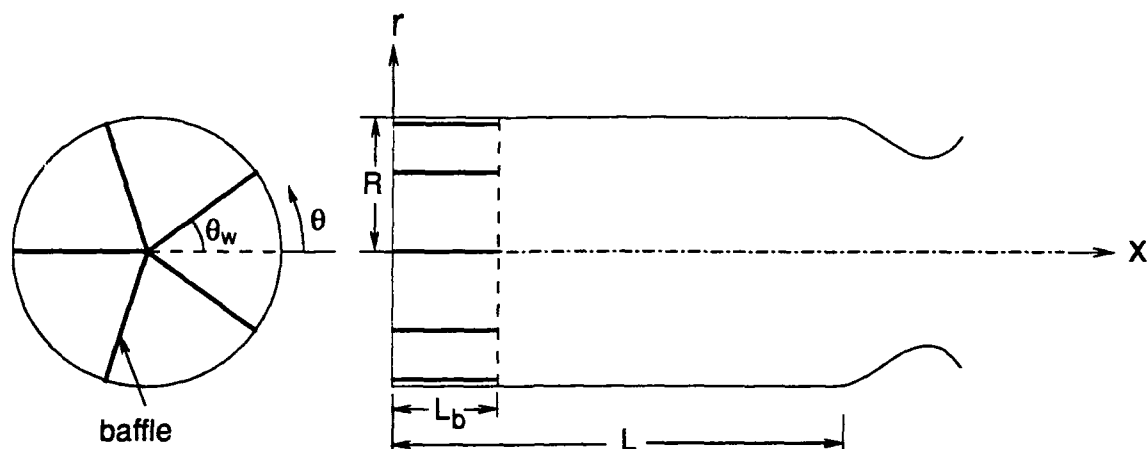


Figure 3.1 Schematic of a Three-Dimensional Baffled Combustion Chamber

the wave equation, since the standard separation of variables method cannot be used due to the boundary shape of the domain.

The fluctuating pressure in each region is synthesized as a Fourier-type expansion in terms of eigenfunctions for the cross section, but allows for temporal and axial variations through the series coefficients.

$$p'(\mathbf{r}, t) = \bar{p} \sum_{n=0}^{\infty} \zeta_n(x, t) \psi_n(r, \theta) \quad (3.1)$$

where the eigenfunction  $\psi_n$  satisfies the Helmholtz equation in the transverse plane:

$$\nabla_r^2 \psi_n + k_n^2 \psi_n = 0 \quad (3.2)$$

subject to the boundary condition

$$\mathbf{n} \cdot \nabla \psi_n = 0 \quad (3.3)$$

The transverse Laplacian operators  $\nabla_r^2$  in the Cartesian and cylindrical coordinates are respectively defined as

$$\nabla_r^2 = \frac{\partial^2}{\partial y^2} + \frac{\partial^2}{\partial z^2} \quad (3.4a)$$

and

$$\nabla_r^2 = \frac{1}{r} \frac{\partial}{\partial r} \left( r \frac{\partial}{\partial r} \right) + \frac{1}{r^2} \frac{\partial^2}{\partial \theta^2} \quad (3.4b)$$

Then, the complete Laplacian operator  $\nabla^2$  becomes

$$\nabla^2 = \nabla_r^2 + \frac{\partial^2}{\partial x^2} \quad (3.5)$$

The subscript  $n$  stands for the doublet of indices  $(m, s)$  defined below. Due to the azimuthal degeneracy in the cylindrical chamber,  $\psi_n$  has two possible forms:

$$\psi_n \sim J_m(\kappa_{ms}r) \begin{cases} \cos m\theta \\ \sin m\theta \end{cases} \quad (3.6)$$

The transverse eigenvalues, represented by the wave number  $\kappa_{ms}$ , are determined by the roots of the derivative of the  $m$ th Bessel function at the chamber wall. That is,

$$\left[ \frac{dJ_m(\kappa_{ms}r)}{dr} \right]_{r=R} = 0 \quad (3.7)$$

Now multiply the wave equation (2.29) by  $\psi_n$  and Eq. (3.2) by  $p'$ , subtract the results, and integrate over the cross section to find

$$\iint \left[ \psi_n \frac{\partial^2 p'}{\partial x^2} - \frac{\psi_n}{a^2} \frac{\partial^2 p'}{\partial t^2} - k_n^2 p \psi_n \right] dS = \iint \psi_n h dS + \oint \psi_n \mathbf{f}_T \cdot \mathbf{n} dl \quad (3.8)$$

where the line integration on the right hand side is conducted along the baffle blades and/or the circumference of the chamber wall at each cross section, and the function  $\mathbf{f}_T$  is defined in the transverse plane as

$$\mathbf{f}_T \cdot \mathbf{n} = \nabla_T p' \cdot \mathbf{n} \quad (3.9)$$

Substitute Eq. (3.1) into Eq. (3.8) and rearrange the result to get the following differential equation for  $\zeta_n(x, t)$ .

$$\frac{\partial^2 \zeta_n}{\partial t^2} - \bar{a}^2 \frac{\partial^2 \zeta_n}{\partial x^2} + \omega_n^2 \zeta_n = -\frac{\bar{a}^2}{\bar{p}E_n^2} \left[ \iint \psi_n h dS + \oint \psi_n \mathbf{f}_T \cdot \mathbf{n} dl \right] \quad (3.10)$$

where  $\omega_n$  is the frequency of the normal transverse mode  $\psi_n$ , defined as

$$\omega_n = \bar{a}k_n \quad (3.11)$$

The Euclidean norm of the mode function,  $E_n$  is defined as

$$E_n^2 = \iint \psi_n^2 dS \quad (3.12)$$

For linear acoustic problems, all the property functions and variables are assumed to vary in a time-harmonic fashion,

$$\begin{aligned} p'(\mathbf{r}, t) &= \hat{p}(\mathbf{r})e^{i\Omega t} \\ \mathbf{u}'_g(\mathbf{r}, t) &= \hat{\mathbf{u}}_g(\mathbf{r})e^{i\Omega t} \\ \zeta_n(x, t) &= \hat{\zeta}_n(x)e^{i\Omega t} \\ h(\mathbf{r}, t) &= \hat{h}(\mathbf{r})e^{i\Omega t} \\ \mathbf{f}_T(r, \theta, t) &= \hat{\mathbf{f}}_T(r, \theta)e^{i\Omega t} \end{aligned} \quad (3.13)$$

where  $\Omega$  is the complex frequency of oscillation and is defined as

$$\Omega = \omega - i\alpha \quad (3.14)$$

The primary purpose of linear stability analysis, then, is to determine the radian frequency  $\omega$  and the growth constant  $\alpha$ .

The ordinary differential equation for the axial distribution function  $\hat{\zeta}_n$  is obtained from the substitution of Eq. (3.13) into Eq. (3.10).

$$\frac{d^2 \hat{\zeta}_n}{dx^2} + \theta_n^2 \hat{\zeta}_n = \frac{1}{\bar{p}E_n^2} \left[ \iint \psi_n \hat{h} dS + \oint \psi_n \hat{\mathbf{f}}_r \cdot \mathbf{n} dl \right] \quad (3.15)$$

where the modified wave number  $\theta_n$  is defined as

$$\theta_n^2 = \frac{\Omega^2 - \omega_n^2}{\bar{a}^2} \quad (3.16)$$

Combustion is often assumed to be concentrated at the injector face, an assumption that is based on the experimental observation that the majority of the combustion processes are completed near the injector of the chamber.<sup>51</sup> Given this condition, the mean flow Mach number is considered as constant. That is,

$$\bar{\mathbf{u}}_g = M\bar{a}\mathbf{e}_x \quad (3.17)$$

where  $M$  is the constant Mach number and  $\mathbf{e}_x$  is the unit vector in the axial direction. However, this assumption consequently limits the range of mean flow Mach number. For example, if the Mach number of the average flow is larger than roughly 0.4, the approximation of classical acoustics deteriorates since the Doppler effect and refraction may cause substantial distortions of the acoustic field. But the

mean flow Mach number is generally small enough over most physical combustion chambers. With this assumption the linear mean flow effect  $h_1$  in the wave equation can be expressed as

$$h_1 = -\bar{\rho} \nabla \cdot \left[ \bar{u}_g \frac{\partial \mathbf{u}'_g}{\partial x} \right] + \frac{1}{\bar{a}^2} \bar{u}_g \cdot \nabla \frac{\partial p'}{\partial t} \quad (3.18)$$

Within first order accuracy, the acoustic velocity  $\mathbf{u}'_g$  in Eq. (3.18) can be expressed in terms of the acoustic pressure  $p'$  using the classical acoustic momentum equation.

$$\frac{\partial \mathbf{u}'_g}{\partial t} = -\frac{1}{\bar{\rho}} \nabla p' \quad (3.19)$$

Substitution of Eq. (3.19) into Eq. (3.18) yields the final expression for the linear effects of the wave equation.

$$\hat{h}_{lin} = -\frac{i \bar{u}_g}{\Omega} \frac{\partial}{\partial x} (\nabla^2 \hat{p}) + \frac{i \Omega}{\bar{a}^2} \bar{u}_g \cdot \nabla \hat{p} \quad (3.20)$$

Substitution of expression (3.20) into Eq. (3.15) leads to a second-order ordinary differential equation for the axial distribution function  $\hat{\zeta}_n$ .

$$\frac{d^2 \hat{\zeta}_n}{dx^2} - \frac{2M\Omega i}{\bar{a}} \frac{d\hat{\zeta}_n}{dx} + \theta_n^2 \hat{\zeta}_n = 0 \quad (3.21)$$

The major task at this point is to determine the complex frequency characterizing linear pressure oscillations. Two cases are treated separately: two- and three-dimensional baffled chambers. For both cases, the acoustic wave characteristics are investigated systematically to give a basic understanding of the wave structures in the chambers.

## 3.2 Two-Dimensional Baffled Chamber

Although the configurations of most practical baffled combustion chambers are three-dimensional, it is beneficial to first achieve the basic understanding of the oscillatory fields in a two-dimensional chamber. This model simplifies the geometric complexity of the problem, and clearly presents some important mechanisms of baffles for modifying the characteristics of unsteady motions. Fig. 3.2 shows the schematic of a two-dimensional baffled combustion chamber. The acoustic fields in the baffle compartments and the main chamber are linked together by requiring continuity of acoustic pressure and axial velocity at the interface. This procedure eventually leads to a transcendental equation for the complex wave number. Results provide explicit information about the acoustic wave structure and complex frequency.

### 3.2.1 Acoustic Field in Baffle Compartments

Because Eq. (3.21) is a second-order ordinary differential equation with constant coefficients, the solution in a two-dimensional model takes the form

$$\hat{\zeta}_{mb}(x) = A_{mb}e^{iq_{mb,1}x} + B_{mb}e^{iq_{mb,2}x} \quad (3.22)$$

where

$$q_{mb,1} = \frac{M\Omega}{\bar{a}} + \sqrt{\left[\frac{M\Omega}{\bar{a}}\right]^2 + \theta_{mb}^2} \quad (3.23a)$$

$$q_{mb,2} = \frac{M\Omega}{\bar{a}} - \sqrt{\left[\frac{M\Omega}{\bar{a}}\right]^2 + \theta_{mb}^2} \quad (3.23b)$$

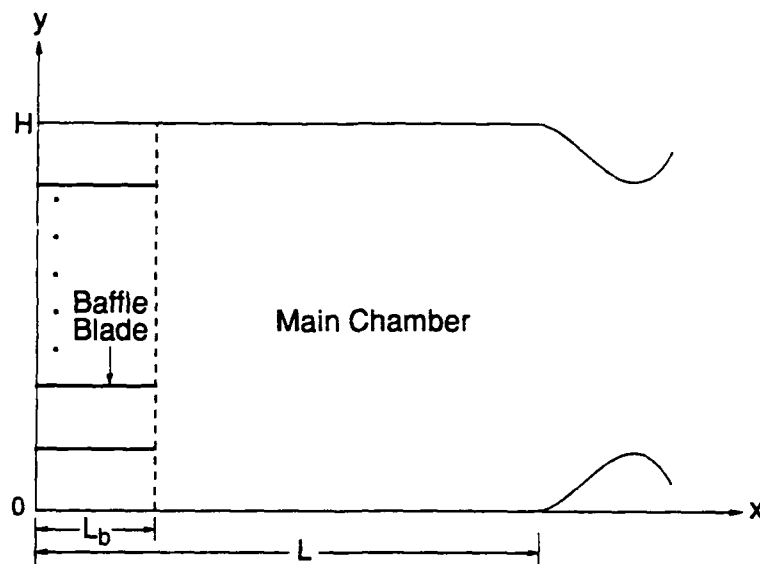


Figure 3.2 Schematic of a Two-Dimensional Baffled Combustion Chamber

The subscript  $b$  stands for baffle compartments. The acoustic boundary condition at the injector face is characterized by an acoustic admittance defined as

$$A_I = \frac{\hat{u}'/\bar{a}}{\hat{p}'/\bar{\gamma}\bar{p}} \Big|_{x=0} \quad (3.24)$$

This leads to a relationship between the coefficients  $A_{mb}$  and  $B_{mb}$ .

$$C_{mb} = \frac{B_{mb}}{A_{mb}} = -\frac{q_{mb,1}}{q_{mb,2}} = -\frac{\frac{M\Omega}{\bar{a}} + \sqrt{\left[\frac{M\Omega}{\bar{a}}\right]^2 + \theta_{mb}^2} + \frac{\Omega}{\bar{a}} A_I}{\frac{M\Omega}{\bar{a}} - \sqrt{\left[\frac{M\Omega}{\bar{a}}\right]^2 + \theta_{mb}^2} + \frac{\Omega}{\bar{a}} A_I} \quad (3.25)$$

For two-dimensional transverse oscillations, the normal mode shape  $\psi_m$  is a function of  $y$  only. Thus Eq. (3.2) reduces to

$$\frac{d^2\psi_m}{dy^2} + k_m^2\psi_m = 0 \quad (3.26)$$

The solution for the  $\mu^{\text{th}}$  baffle compartment becomes

$$\psi_m^\mu = A \cos k_m^\mu y + B \sin k_m^\mu y \quad (3.27)$$

The assumption of rigid surfaces gives the following conditions for baffle blades and chamber wall.

$$\frac{d\psi_m}{dy} = 0 \quad \text{at} \quad \begin{cases} y = \frac{\mu H}{N} \\ y = \frac{(\mu-1)H}{N} \end{cases} \quad \mu = 1, 2, \dots, N \quad (3.28)$$

where  $N$  denotes the number of baffle blades. Thus, the normal transverse mode shape,  $\psi_m$ , for the  $\mu^{\text{th}}$  baffle compartment is determined with the boundary conditions set by Eq. (3.28), such that

$$\psi_m^\mu(y) = A \cos\left(\frac{m\pi N}{H}y\right) \quad (3.29)$$

If the baffle blades are assumed to be equally spaced in the chamber and have rigid surfaces, then the mode shape of the acoustic pressure in the  $\mu^{\text{th}}$  baffle compartment is shown to be

$$\hat{p}^\mu = \bar{p} \sum_{m=0}^{\infty} A_m^\mu \cos\left(\frac{m\pi N}{H}y\right) \left[ \frac{e^{iq_{mb,1}x} + C_{mb}e^{iq_{mb,2}x}}{e^{iq_{mb,1}L_b} + C_{mb}e^{iq_{mb,2}L_b}} \right] \quad (3.30)$$

The constant denominator within the square bracket is added in this expression to facilitate the matching at the interface. This constant denominator does not affect the solution, since the amplitude of linear oscillations is arbitrary anyway. An extension of the above expression to cases involving a non-uniform distribution of baffle blades is straightforward, only at the expense of more mathematical manipulations.

### 3.2.2 Acoustic Field in Main Combustion Chamber

The solution to Eq. (3.21) for the axial part of the acoustic field in the main chamber takes the form

$$\hat{\zeta}_{nc}(x) = A_{nc}e^{iq_{nc,1}(x-L)} + B_{nc}e^{iq_{nc,2}(x-L)} \quad (3.31)$$

where

$$q_{nc,1} = \frac{M\Omega}{\bar{a}} + \sqrt{\left[\frac{M\Omega}{\bar{a}}\right]^2 + \theta_{nc}^2} \quad (3.32a)$$

$$q_{nc,2} = \frac{M\Omega}{\bar{a}} - \sqrt{\left[\frac{M\Omega}{\bar{a}}\right]^2 + \theta_{nc}^2} \quad (3.32b)$$

Here, the subscript  $c$  denotes quantities associated with the main chamber. The acoustic boundary condition provided by the exhaust nozzle may be represented by a nozzle admittance defined below. Although this is a simplistic representation of the effect of the nozzle, the ease of application allows for a focus of attention on the effect of baffles. Furthermore, for short nozzles, this representation can be quite accurate.<sup>52</sup>

$$A_N = \frac{\hat{u}'/\bar{a}}{\hat{p}'/\bar{\gamma}\bar{p}} \Big|_{x=L} \quad (3.33)$$

This nozzle admittance function leads to the following relationship for the coefficients  $A_{nc}$  and  $B_{nc}$ .

$$C_{nc} = \frac{B_{nc}}{A_{nc}} = -\frac{q_{nc,1} + \Omega\bar{\rho}A_d}{q_{nc,2} + \Omega\bar{\rho}A_d} = -\frac{\frac{M\Omega}{\bar{a}} + \sqrt{\left[\frac{M\Omega}{\bar{a}}\right]^2 + \theta_{nc}^2} + \frac{\Omega}{\bar{a}}A_N}{\frac{M\Omega}{\bar{a}} - \sqrt{\left[\frac{M\Omega}{\bar{a}}\right]^2 + \theta_{nc}^2} + \frac{\Omega}{\bar{a}}A_N} \quad (3.34)$$

The transverse mode function  $\psi_n$  for the main chamber, based on the assumption of a rigid chamber wall, can be expressed as

$$\psi_n(y) = A \cos\left(\frac{n\pi}{H}y\right) \quad (3.35)$$

Substitution of Eqs. (3.31) and (3.35) into Eq. (3.1) yields the expression for the mode shape of the acoustic pressure in the main chamber.

$$\hat{p}^c = \bar{p} \sum_{n=0}^{\infty} B_n^c \cos\left(\frac{n\pi}{H}y\right) \left[ \frac{e^{iq_{nc,1}(x-L)} + C_{nc}e^{iq_{nc,2}(x-L)}}{e^{iq_{nc,1}(L_b-L)} + C_{nc}e^{iq_{nc,2}(L_b-L)}} \right] \quad (3.36)$$

Again the denominator in the big bracket is added for the convenience of matching at the interface in the following section.

### 3.2.3 Matching of Acoustic Fields in Baffle Compartments and Main Chamber

Together, Eqs. (3.30) and (3.36) represent the acoustic pressure fields in the whole chamber in terms of the transverse eigenfunctions. Once the coefficients  $A_m^\mu$  and  $B_n^c$  and frequency  $\Omega$  are known, the pressure distribution in the entire chamber can be easily determined. The next step, therefore, is to get these coefficients, using the matching of the acoustic fields in the baffle compartments with that of the main chamber at the interface. This matching requires continuity of acoustic pressure and axial velocity.

$$\hat{p}^\mu|_{x=L_b} = \hat{p}^c|_{x=L_b} \quad (3.37)$$

$$\hat{u}'^\mu|_{x=L_b} = \hat{u}'^c|_{x=L_b} \quad (3.38)$$

From Eqs. (3.30) and (3.36), the pressure distributions of the baffle compartments and the main chamber at the interface (i.e.  $x = L_b$ ) are, respectively

$$\hat{p}^\mu = \sum_{m=0}^{\infty} A_m^\mu \cos\left(\frac{m\pi N}{H}y\right), \quad \frac{(\mu-1)H}{N} \leq y \leq \frac{\mu H}{N} \quad (3.39)$$

$$\hat{p}^c = \sum_{n=0}^{\infty} B_n^c \cos\left(\frac{n\pi}{H}y\right) \quad (3.40)$$

Note that indices  $m$  and  $n$  are used for the acoustic fields in the baffle compartments and the main chamber, respectively, to avoid confusion. Substitution of the above two expressions into the pressure matching condition (3.37), gives an expression for the baffle compartment coefficients,  $A_m^\mu$ , in terms of the main chamber coefficients,  $B_n^c$ .

$$A_m^\mu = \sum_{n=0}^{\infty} \left[ B_n^c \frac{\int_{\frac{(\mu-1)H}{N}}^{\frac{\mu H}{N}} \cos\left(\frac{m\pi N}{H}y\right) \cos\left(\frac{n\pi}{H}y\right) dy}{\int_{\frac{(\mu-1)H}{N}}^{\frac{\mu H}{N}} \cos^2\left(\frac{m\pi N}{H}y\right) dy} \right] \quad (3.41)$$

With the aid of the acoustic momentum equation, the second matching condition (3.38) can be simplified to the continuity of the gradient of acoustic pressures.

$$\left. \frac{\partial \hat{p}^\mu}{\partial x} \right|_{x=L_b} = \left. \frac{\partial \hat{p}^c}{\partial x} \right|_{x=L_b} \quad (3.42)$$

Now taking the spatial derivatives of (3.30) and (3.36) with respect to  $x$ , and evaluating the results at  $x = L_b$  yields

$$\left. \frac{\partial \hat{p}^\mu}{\partial x} \right|_{x=L_b} = \sum_{m=0}^{\infty} \left[ A_m^\mu \cos\left(\frac{m\pi N}{H}y\right) \times \frac{i q_{mb,1} e^{i q_{mb,1} L_b} + i q_{mb,2} C_{mb} e^{i q_{mb,2} L_b}}{e^{i q_{mb,1} L_b} + C_{mb} e^{i q_{mb,2} L_b}} \right] \quad (3.43)$$

$$\left. \frac{\partial \hat{p}^c}{\partial x} \right|_{x=L_b} = \sum_{n=0}^{\infty} \left[ B_n^c \cos\left(\frac{n\pi}{H}y\right) \times \frac{i q_{nc,1} e^{i q_{nc,1} (L_b-L)} + i q_{nc,2} C_{nc} e^{i q_{nc,2} (L_b-L)}}{e^{i q_{nc,1} (L_b-L)} + C_{nc} e^{i q_{nc,2} (L_b-L)}} \right] \quad (3.44)$$

Substitution of Eqs. (3.43) and (3.44) into Eq. (3.42) yields an explicit expression for the coefficients  $B_n^c$  in terms of  $A_m^\mu$ , independent of Eq. (3.41).

$$B_n^c = \sum_{m=0}^{\infty} \sum_{\mu=1}^N \left[ A_m^\mu \frac{\int_{\frac{(\mu-1)H}{N}}^{\frac{\mu H}{N}} \cos\left(\frac{m\pi N}{H}y\right) \cos\left(\frac{n\pi}{H}y\right) dy}{\int_0^H \cos^2\left(\frac{n\pi N}{H}y\right) dy} \times \frac{G_m(\Omega)}{H_n(\Omega)} \right] \quad (3.45)$$

where

$$G_m(\Omega) = \frac{iq_{mb,1}e^{iq_{mb,1}L_b} + iq_{mb,2}C_{mb}e^{iq_{mb,2}L_b}}{e^{iq_{mb,1}L_b} + C_{mb}e^{iq_{mb,2}L_b}} \quad (3.46a)$$

$$H_n(\Omega) = \frac{iq_{nc,1}e^{iq_{nc,1}(L_b-L)} + iq_{nc,2}C_{nc}e^{iq_{nc,2}(L_b-L)}}{e^{iq_{nc,1}(L_b-L)} + C_{nc}e^{iq_{nc,2}(L_b-L)}} \quad (3.46b)$$

Since the amplitude is arbitrary for linear analyses, a normalization of the acoustic pressure to a particular mode within the main chamber helps to determine the complex frequency of acoustic oscillations. This condition can be formally expressed, from Eq. (3.45), as

$$H_{\tilde{n}}(\Omega) = \sum_{m=0}^{\infty} \sum_{\mu=1}^N \left[ A_m^{\mu} \frac{\int_{\frac{(\mu-1)H}{N}}^{\frac{\mu H}{N}} \cos\left(\frac{m\pi N}{H}y\right) \cos\left(\frac{\tilde{n}\pi}{H}y\right) dy}{\int_0^H \cos^2\left(\frac{\tilde{n}\pi N}{H}y\right) dy} \times G_m(\Omega) \right] \quad (3.47)$$

where  $\tilde{n}$  is the specific mode of concern in the main chamber. For example, if a first transverse mode is of interest,  $\tilde{n}$  would equal one. Note that this normalization is not a necessary step in solving the problem, but it is only a convenience used to aid in the numerical computation of the complex frequency and mode shapes. If this normalization is not specified, inversion of a rather large matrix would be required. This matrix contains the coefficients of Eqs. (3.41) and (3.45), with eigenvalues corresponding to the complex frequency, as shown in the Appendix. Arbitrarily setting the dominant mode amplitude equal to one allows a simpler iterative solution to the system of equations, and will not change the value of frequency or mode shapes, since the arbitrary amplitude cancels out, anyway.

Because of the transcendental nature of Eq. (3.47), an iteration scheme is used to determine the complex frequency. The overall numerical procedure is

conducted as follows. First, Eq. (3.41) is substituted into Eqs. (3.45) and (3.47) for simplification,

$$B_n^c = \sum_{m=0}^{\infty} \sum_{\mu=1}^N \sum_{m'=0}^{\infty} \left[ B_{m'}^c \frac{\int_{(\mu-1)H}^{\frac{\mu H}{N}} \cos\left(\frac{m\pi N}{H}y\right) \cos\left(\frac{m'\pi}{H}y\right) dy}{\int_{(\mu-1)H}^{\frac{\mu H}{N}} \cos^2\left(\frac{m'\pi N}{H}y\right) dy} \right. \\ \left. \times \frac{\int_{(\mu-1)H}^{\frac{\mu H}{N}} \cos\left(\frac{m\pi N}{H}y\right) \cos\left(\frac{n\pi}{H}y\right) dy}{\int_0^H \cos^2\left(\frac{n\pi N}{H}y\right) dy} \times \frac{G_m(\Omega)}{H_n(\Omega)} \right] \quad (3.48)$$

and

$$H_{\bar{n}}(\Omega) = \sum_{m=0}^{\infty} \sum_{\mu=1}^N \sum_{m'=0}^{\infty} \left[ B_{m'}^c \frac{\int_{(\mu-1)H}^{\frac{\mu H}{N}} \cos\left(\frac{m\pi N}{H}y\right) \cos\left(\frac{m'\pi}{H}y\right) dy}{\int_{(\mu-1)H}^{\frac{\mu H}{N}} \cos^2\left(\frac{m'\pi N}{H}y\right) dy} \right. \\ \left. \times \frac{\int_{(\mu-1)H}^{\frac{\mu H}{N}} \cos\left(\frac{m\pi N}{H}y\right) \cos\left(\frac{\bar{n}\pi}{H}y\right) dy}{\int_0^H \cos^2\left(\frac{\bar{n}\pi N}{H}y\right) dy} \times G_m(\Omega) \right] \quad (3.49)$$

The second step involves the application of the Newton-Raphson technique to determine the complex frequency from Eq. (3.49). As a first approximation,  $B_{m'}^c = \delta_{m'\bar{n}}$  and  $\Omega = \omega_n$  are used to initiate the iteration procedure. The calculated  $\Omega$  is used to update  $B_n^c$  from Eq. (3.48), which is then substituted back into Eq. (3.49) to calculate the complex frequency. This procedure repeats itself until the converged solutions for  $\Omega$  and  $B_n^c$  are obtained. Finally, the coefficient  $A_m^\mu$  is determined from Eq. (3.41). The iteration scheme functions quite effectively and provides reasonable results within only a few iterations.

### 3.3 Three-Dimensional Baffled Chamber

In this section, a three-dimensional cylindrical baffled chamber, which is more representative of actual rocket systems, is investigated. Usually two types of baffle configurations are used to suppress the transverse modes of oscillation in such chambers: radial baffle blades and hub-type blades. The radial baffle blade is utilized to control tangential modes of oscillation, while the hub-type affects the radial modes. But in order to concentrate attention on the effect of baffles on the tangential mode of oscillation, only problems involving simple configurations of radial baffles are considered here. The acoustic field can be treated following the general approach described in the preceding section.

#### 3.3.1 Acoustic Field in Baffle Compartments

The solution of Eq. (3.21) for the three-dimensional chambers takes the form

$$\hat{\zeta}_{mb}(x) = A_{mb}e^{iq_{mb,1}x} + B_{mb}e^{iq_{mb,2}x} \quad (3.50)$$

where  $q_{mb,1}$  and  $q_{mb,2}$  are defined in the same way as in Eqs. (3.23a) and (3.23b). However, the transverse mode shape  $\psi_n$  for a cylindrical chamber with radial baffle blades is a function of  $r$  and  $\theta$  only, taking the form

$$\psi_n = (A \cos m\theta + B \sin m\theta)J_m(\kappa_{ms}r) \quad (3.51)$$

Baffle blades are assumed to be rigid surfaces, which gives the following conditions in the  $\mu$ th baffle compartment.

$$\frac{\partial \psi_n^\mu}{\partial \theta} = 0 \quad \text{at} \quad \begin{cases} \theta = \frac{2\pi(\mu-1)}{N} \\ \theta = \frac{2\pi\mu}{N} \end{cases} \quad \mu = 1, 2, \dots, N \quad (3.52)$$

where  $N$  is the number of radial baffle blades. These boundary conditions are applied to Eq. (3.51) to yield

$$\begin{aligned} B &= 0 \\ m &= \frac{nN}{2} \quad (n = 0, 1, 2, \dots) \end{aligned} \quad (3.53)$$

In most actual cases, a baffle configuration has an odd number of radial baffle blades with the exception of a one-blade case, which is practically never observed. It would offer protection from modes that are of an order less than the number of blades and, to some degree, protection from modes of an order higher than the number of blades if the order of the mode divided by the number of blades is not equal to an integer. With the odd number  $N$ , then,

$$m = 0, \frac{N}{2}, N, \frac{3N}{2}, 2N, \dots$$

Since half-mode waves do not exist physically, the only values of  $m$  considered in this analysis are those for which

$$m = Nl \quad (l = 0, 1, 2, \dots) \quad (3.54)$$

Thus, the transverse normal mode shape for the  $\mu$ th baffle compartment becomes

$$\psi_{Nl_s}^\mu = A \cos(Nl\theta) J_{Nl}(\kappa_{Nl_s} r) \quad \begin{cases} l = 0, 1, 2, \dots \\ s = 1, 2, 3, \dots \end{cases} \quad (3.55)$$

Here,  $\psi_n$  is replaced by  $\psi_{Nl_s}$  in Eq. (3.55) to distinguish between the main chamber and the baffle compartment indices.

Substitution of Eqs. (3.51) and (3.55) into Eq. (3.1) yields the mode shape of the acoustic pressure for the  $\mu$ th baffle compartment.

$$\hat{p}^\mu = \bar{p} \sum_{l=0}^{\infty} \sum_{s=1}^{\infty} A_{Nl_s}^\mu \psi_{Nl_s}^\mu \left[ \frac{e^{iq_{mb,1}x} + C_{mb} e^{iq_{mb,2}x}}{e^{iq_{mb,1}L_b} + C_{mb} e^{iq_{mb,2}L_b}} \right] \quad (3.56)$$

The coefficient  $C_{mb}$  represents the boundary condition at the injector face and is defined in the same way as in Eq. (3.25). The denominator in the bracket is again added for convenience of matching in the following section.

### 3.3.2 Acoustic Field in Main Combustion Chamber

The solution to Eq. (3.21) for the acoustic field within the main chamber takes the form

$$\hat{\zeta}_{nc}(x) = A_{nc}e^{iq_{nc,1}(x-L)} + B_{nc}e^{iq_{nc,2}(x-L)} \quad (3.57)$$

where  $q_{nc,1}$  and  $q_{nc,2}$  are defined in the same way as in Eqs. (3.32a) and (3.32b). The normal mode shape,  $\psi_n$ , for standing transverse motion in the main chamber takes the form

$$\psi_{nt}^c = A \cos n\theta J_n(\kappa_{nt}r) \quad (3.58)$$

To avoid confusion of the main chamber solution with the solution in the baffle compartments, the index  $nt$  is used for the acoustic field in the main chamber. Now, combine Eqs. (3.57) and (3.58) to obtain the mode shape of the acoustic pressure in the main chamber.

$$\hat{p}^c = \bar{p} \sum_{n=0}^{\infty} \sum_{t=1}^{\infty} B_{nt}^c \psi_{nt}^c \left[ \frac{e^{iq_{nc,1}(x-L)} + C_{nc}e^{iq_{nc,2}(x-L)}}{e^{iq_{nc,1}(L_b-L)} + C_{nc}e^{iq_{nc,2}(L_b-L)}} \right] \quad (3.59)$$

The coefficient  $C_{nc}$  incorporates the effect of the nozzle admittance boundary condition and is determined in the same way as in Eq. (3.34). Again the denominator in the bracket is added to this expression to facilitate the matching in the following section.

### 3.3.3 Matching of Acoustic Fields in Baffle Compartments and Main Chamber

Together, Eqs. (3.56) and (3.59) express the acoustic pressure distributions in the whole chamber in terms of eigenfunctions. Once the coefficients  $A_{Nl_s}^\mu$  and  $B_{nt}^c$  and the frequency are found, the acoustic fields in the entire chamber can be easily computed. The matching of the acoustic fields in the baffle compartments and the main chamber at the interface gives sufficient equations for determining the coefficients and, thus, the wave characteristics of the baffled chambers. The matching requires continuity of acoustic pressure and axial velocity.

$$\hat{p}^\mu|_{x=L_b} = \hat{p}^c|_{x=L_b} \quad (3.60)$$

$$\hat{u}'^\mu|_{x=L_b} = \hat{u}'^c|_{x=L_b} \quad (3.61)$$

From Eqs. (3.56) and (3.59), the pressure distributions of the baffle compartments and the main chamber at the interface (i.e.  $x = L_b$ ) are, respectively

$$\hat{p}^\mu = \sum_{l=0}^{\infty} \sum_{s=1}^{\infty} A_{Nl_s}^\mu \psi_{Nl_s}^\mu, \quad \frac{2\pi(\mu-1)}{N} \leq \theta \leq \frac{2\pi\mu}{N} \quad (3.62)$$

$$\hat{p}^c = \sum_{n=0}^{\infty} \sum_{t=1}^{\infty} B_{nt}^c \psi_{nt}^c \quad (3.63)$$

Substitution of Eqs. (3.62) and (3.63) into the pressure matching condition (3.60), yields an explicit expression for the baffle compartment coefficients,  $A_{Nl_s}^\mu$ , in terms of the main chamber coefficients,  $B_{nt}^c$ .

$$A_{Nl_s}^\mu = \sum_{n=0}^{\infty} \sum_{t=1}^{\infty} \left[ B_{nt}^c \frac{\int_{\frac{2\pi(\mu-1)}{N}}^{\frac{2\pi\mu}{N}} \int_0^R \psi_{Nl_s}^\mu \psi_{nt}^c r dr d\theta}{\int_{\frac{2\pi(\mu-1)}{N}}^{\frac{2\pi\mu}{N}} \int_0^R (\psi_{Nl_s}^\mu)^2 r dr d\theta} \right] \quad (3.64)$$

With the aid of the acoustic momentum equation, the second matching condition, Eq. (3.61), can be interpreted as the continuity of the axial gradient of acoustic pressure.

$$\left. \frac{\partial \hat{p}^\mu}{\partial x} \right|_{x=L_b} = \left. \frac{\partial \hat{p}^c}{\partial x} \right|_{x=L_b} \quad (3.65)$$

Differentiation of Eqs. (3.56) and (3.59) with respect to  $x$  and subsequent evaluation at  $x = L_b$  give

$$\left. \frac{\partial \hat{p}^\mu}{\partial x} \right|_{x=L_b} = \sum_{l=0}^{\infty} \sum_{s=1}^{\infty} A_{Nls}^\mu \psi_{Nls}^\mu \left[ \frac{iq_{mb,1} e^{iq_{mb,1} L_b} + iq_{mb,2} C_{mb} e^{iq_{mb,2} L_b}}{e^{iq_{mb,1} L_b} + C_{mb} e^{iq_{mb,2} L_b}} \right] \quad (3.66)$$

$$\left. \frac{\partial \hat{p}^c}{\partial x} \right|_{x=L_b} = \sum_{n=0}^{\infty} \sum_{t=1}^{\infty} B_{nt}^c \psi_{nt}^c \left[ \frac{iq_{nc,1} e^{iq_{nc,1} (L_b-L)} + iq_{nc,2} C_{nc} e^{iq_{nc,2} (L_b-L)}}{e^{iq_{nc,1} (L_b-L)} + C_{nc} e^{iq_{nc,2} (L_b-L)}} \right] \quad (3.67)$$

Substitution of Eqs. (3.66) and (3.67) into Eq. (3.65) gives an expression for the Fourier coefficients of the main chamber,  $B_{nt}^c$ , in terms of those coefficients for the baffle compartments,  $A_{Nls}^\mu$ .

$$B_{nt}^c = \sum_{l=0}^{\infty} \sum_{s=1}^{\infty} \sum_{\mu=1}^N \left[ A_{Nls}^\mu \frac{\int_{\frac{2\pi(\mu-1)}{N}}^{\frac{2\pi\mu}{N}} \int_0^R \psi_{Nls}^\mu \psi_{nt}^c r dr d\theta}{\int_0^{2\pi} \int_0^R (\psi_{nt}^c)^2 r dr d\theta} \times \frac{G_{Nls}(\Omega)}{H_{nt}(\Omega)} \right] \quad (3.68)$$

where

$$G_{Nls}(\Omega) = \frac{iq_{mb,1} e^{iq_{mb,1} L_b} + iq_{mb,2} C_{mb} e^{iq_{mb,2} L_b}}{e^{iq_{mb,1} L_b} + C_{mb} e^{iq_{mb,2} L_b}} \quad (3.69a)$$

$$H_{nt}(\Omega) = \frac{iq_{nc,1} e^{iq_{nc,1} (L_b-L)} + iq_{nc,2} C_{nc} e^{iq_{nc,2} (L_b-L)}}{e^{iq_{nc,1} (L_b-L)} + C_{nc} e^{iq_{nc,2} (L_b-L)}} \quad (3.69b)$$

As was done for the two-dimensional case, a normalization of the acoustic pressure to a particular mode within the main chamber is made in determining the complex

frequency of the acoustic oscillations. This normalization can be expressed, from Eq. (3.68), as

$$H_{\tilde{n}\tilde{t}}(\Omega) = \sum_{l=0}^{\infty} \sum_{s=1}^{\infty} \sum_{\mu=1}^N \left[ A_{Nl_s}^{\mu} \frac{\int_0^{\frac{2\pi\mu}{N}} \int_0^R \psi_{Nl_s}^{\mu} \psi_{\tilde{n}\tilde{t}}^c r dr d\theta}{\int_0^{2\pi} \int_0^R (\psi_{\tilde{n}\tilde{t}}^c)^2 r dr d\theta} \times G_{Nl_s}(\Omega) \right] \quad (3.70)$$

where  $\tilde{n}$  and  $\tilde{t}$  are specific tangential and radial modes of concern, respectively, in the main chamber. For example, if a first tangential mode is under consideration, both  $\tilde{n}$  and  $\tilde{t}$  would equal one.

An iteration scheme is again used to determine the complex frequency, and the numerical iteration proceeds as follows. First, substitution of Eq. (3.64) into Eqs. (3.68) and (3.70) gives

$$B_{nt}^c = \sum_{l=0}^{\infty} \sum_{s=1}^{\infty} \sum_{\mu=1}^N \sum_{l'=0}^{\infty} \sum_{s'=1}^{\infty} \left[ B_{l's'}^c \frac{\int_0^{\frac{2\pi\mu}{N}} \int_0^R \psi_{Nl_s}^{\mu} \psi_{l's'}^c r dr d\theta}{\int_0^{\frac{2\pi\mu}{N}} \int_0^R (\psi_{Nl_s}^{\mu})^2 r dr d\theta} \times \frac{\int_0^{\frac{2\pi\mu}{N}} \int_0^R \psi_{Nl_s}^{\mu} \psi_{nt}^c r dr d\theta}{\int_0^{2\pi} \int_0^R (\psi_{nt}^c)^2 r dr d\theta} \times \frac{G_{Nl_s}(\Omega)}{H_{nt}(\Omega)} \right] \quad (3.71)$$

and

$$H_{\tilde{n}\tilde{t}}(\Omega) = \sum_{l=0}^{\infty} \sum_{s=1}^{\infty} \sum_{\mu=1}^N \sum_{l'=0}^{\infty} \sum_{s'=1}^{\infty} \left[ B_{l's'}^c \frac{\int_0^{\frac{2\pi\mu}{N}} \int_0^R \psi_{Nl_s}^{\mu} \psi_{l's'}^c r dr d\theta}{\int_0^{\frac{2\pi\mu}{N}} \int_0^R (\psi_{Nl_s}^{\mu})^2 r dr d\theta} \times \frac{\int_0^{\frac{2\pi\mu}{N}} \int_0^R \psi_{Nl_s}^{\mu} \psi_{\tilde{n}\tilde{t}}^c r dr d\theta}{\int_0^{2\pi} \int_0^R (\psi_{\tilde{n}\tilde{t}}^c)^2 r dr d\theta} \times G_{Nl_s}(\Omega) \right] \quad (3.72)$$

Second, a Newton-Raphson iteration scheme is applied to determine the complex frequency  $\Omega$  from Eq. (3.72). As a first approximation,  $B_{l's'}^c = \delta_{l'\tilde{n}} \delta_{s'\tilde{t}}$  and  $\Omega = \omega_n$

are used to initiate the iteration procedure. The calculated  $\Omega$  is used to update  $B_{nt}^c$  from Eq. (3.71), which is then substituted back into Eq. (3.72) to compute the complex frequency. This procedure is repeated until converged solutions for  $\Omega$  and  $B_{nt}^c$  are obtained. Finally, the coefficients,  $A_{Nt}^\mu$ , are determined from Eq. (3.64). Like the two-dimensional solution, this method gives reasonable values for complex frequency  $\Omega$  in a few iterations.

### 3.4 Results and Discussion of Linear Acoustic Analysis

The analysis described in the previous sections has been applied to the study of acoustic wave characteristics in baffled combustion chambers, and the results have provided useful information about the effect of baffles on the detailed flow structure. The consequences for the two cases are presented separately: two- and three-dimensional baffled chambers.

#### 3.4.1 Acoustic Field in Two-Dimensional Baffled Chamber

To gain confidence in the accuracy of this analysis, calculated acoustic fields of normal modes are first validated with numerical solutions obtained from a well-established finite element code, ANSYS.<sup>53</sup> The ANSYS code uses a 3-D isoparametric acoustic fluid element and has been successfully used to study sound propagation and submerged structure dynamics.

Figure 3.3 shows the acoustic pressure fields of the first transverse mode in chambers containing one and two baffle blades. The aspect ratio ( $L/H$ ) of the chamber is 1.25, similar to that of the two-dimensional 'equivalent' combustion

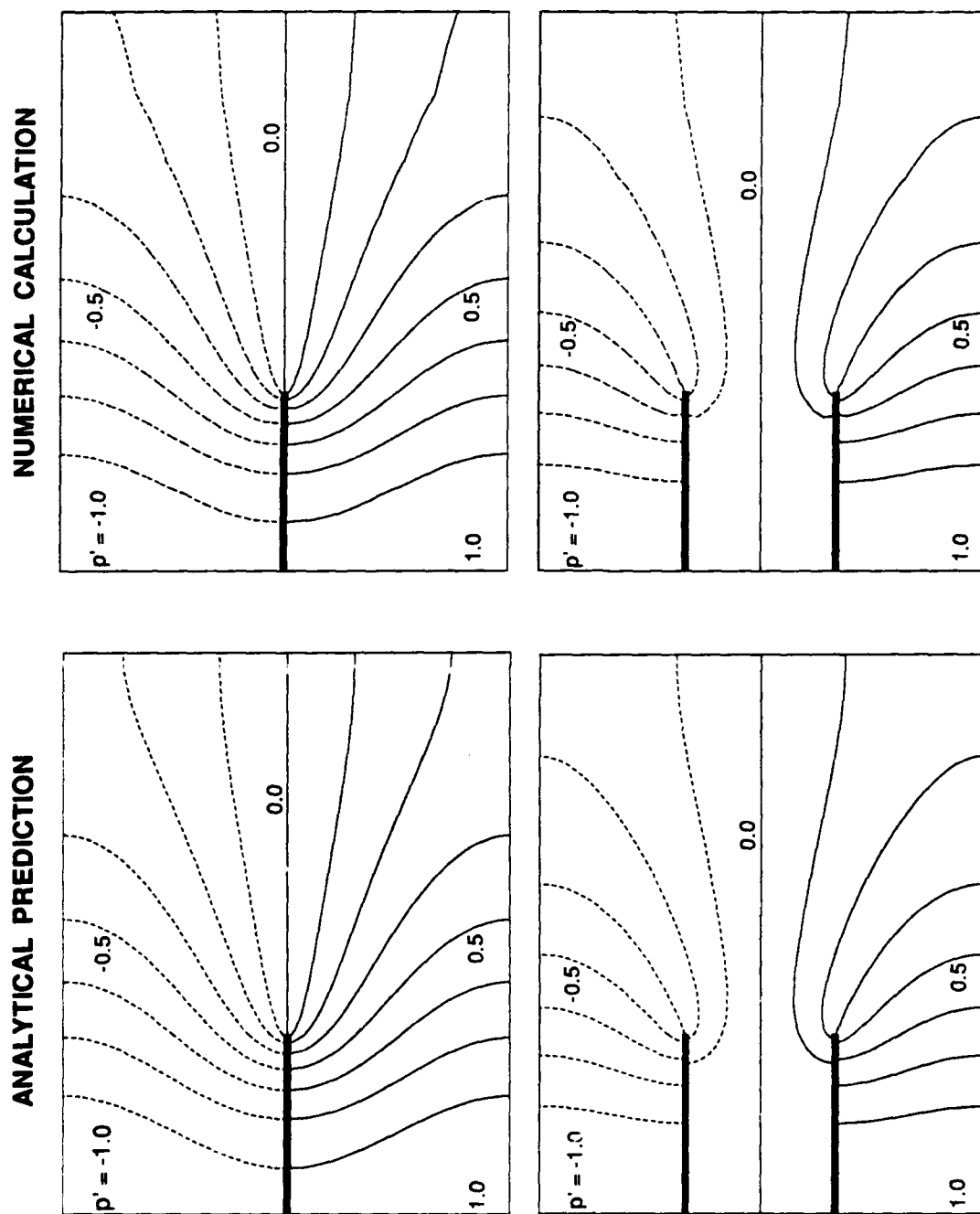


Figure 3.3 Comparison between Analytical and Numerical Results for Acoustic Pressure Contours in Baffled Chambers;  $L_b = 0.4 H$

chamber of the F-1 engine. Zero acoustic admittance is specified at the injector and nozzle entrance to ensure normal mode solutions. Because of the limitation of the wave-front number in the ANSYS code, small kinks can be observed in the numerically calculated pressure contours. The analytical solutions are in excellent agreement with these finite element calculations, so this analytical approach can be applied to acoustic problems in the baffled combustion chamber with confidence.

Figure 3.4 presents the effect of baffle length on the oscillatory pressure fields of the first transverse mode in a one-baffle chamber, and shows that the baffle exerts significant influence on the acoustic field. For long baffles (e.g.,  $L_b = 0.4H$ ), the acoustic motion inside the baffle compartments very much resembles a longitudinal wave and transits to a transverse oscillation downstream of the baffle. This is seen clearly by noticing that the pressure nodal line for the first transverse mode in the unbaffled chamber lies at the center of the chamber parallel to the chamber wall. But once the baffle is added to the chamber, it must move to satisfy the acoustic velocity boundary conditions set by the baffle blades, such that the pressure contour lines are normal to the baffle surface. By shifting the mode of oscillation from transverse to longitudinal inside the baffle compartments, baffles can decrease the prevalence of the transverse modes, which have historically been most troublesome in liquid rocket combustion instability problems, whereas longitudinal modes have not. As a result, however, regions of high amplitude pressure fluctuations are concentrated near the injector face. If pressure sensitive combustion processes are responsible for the instability, the addition of a baffle might, therefore, worsen the problem, since the region sensitive to the variation of acoustic motion is usually close to the injector.

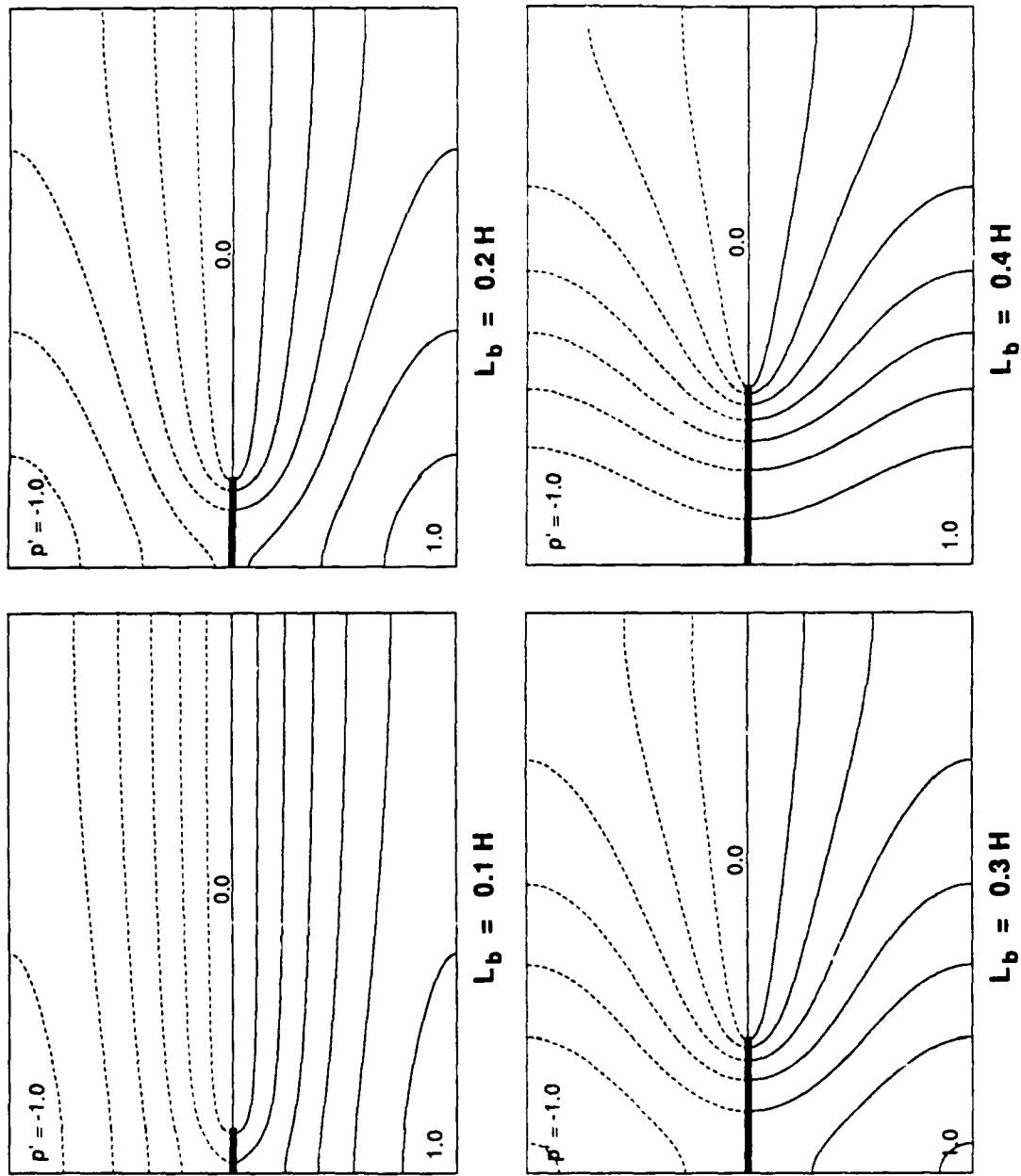


Figure 3.4 Effect of Baffle Length on the Acoustic Pressure Field in a One-Baffle Chamber; the First Transverse Mode

The concentration of large amplitude pressure fluctuations in this region thus has the potential to release large amounts of energy. However, in an unbaffled chamber, the pressure variation associated with a transverse mode can change the orientation of the propellant jets issuing from the injector. This can have a significant influence on the atomization and spray characteristics near the injector face that may be coupled with the chamber acoustics to generate instability. With the addition of a baffle, however, the longitudinal nature of pressure oscillations near the injector face might have no effect, or at least a substantially different effect on this type of combustion process near the injector face.

Figure 3.5 shows the acoustic pressure contours of the first transverse mode in a two-baffled chamber. For a short baffle length (e.g.,  $L_b = 0.1H$ ), transverse oscillations exist in almost the entire chamber except for regions near the baffle tips, but the degree of wave distortion increases with increased baffle length. As with the one-baffle case, longitudinal oscillations become conspicuous in the upper and lower baffle compartments for  $L_b > 0.2H$ , which might mean enhanced stability, as argued previously. Note that the acoustic pressure is almost uniformly distributed in the center baffle compartment, with its magnitude at a minimal level. This suggests that the center compartment may be the most effective in separating the acoustic waves from sensitive combustion processes, and thus might be able to overcome any possible destabilizing influences from the adjacent compartments.

However, the situation for the second transverse mode is quite different. Figure 3.6 shows the oscillatory pressure fields, which indicates that the wave motion exhibits longitudinal motion in the top and bottom baffle compartments, similar

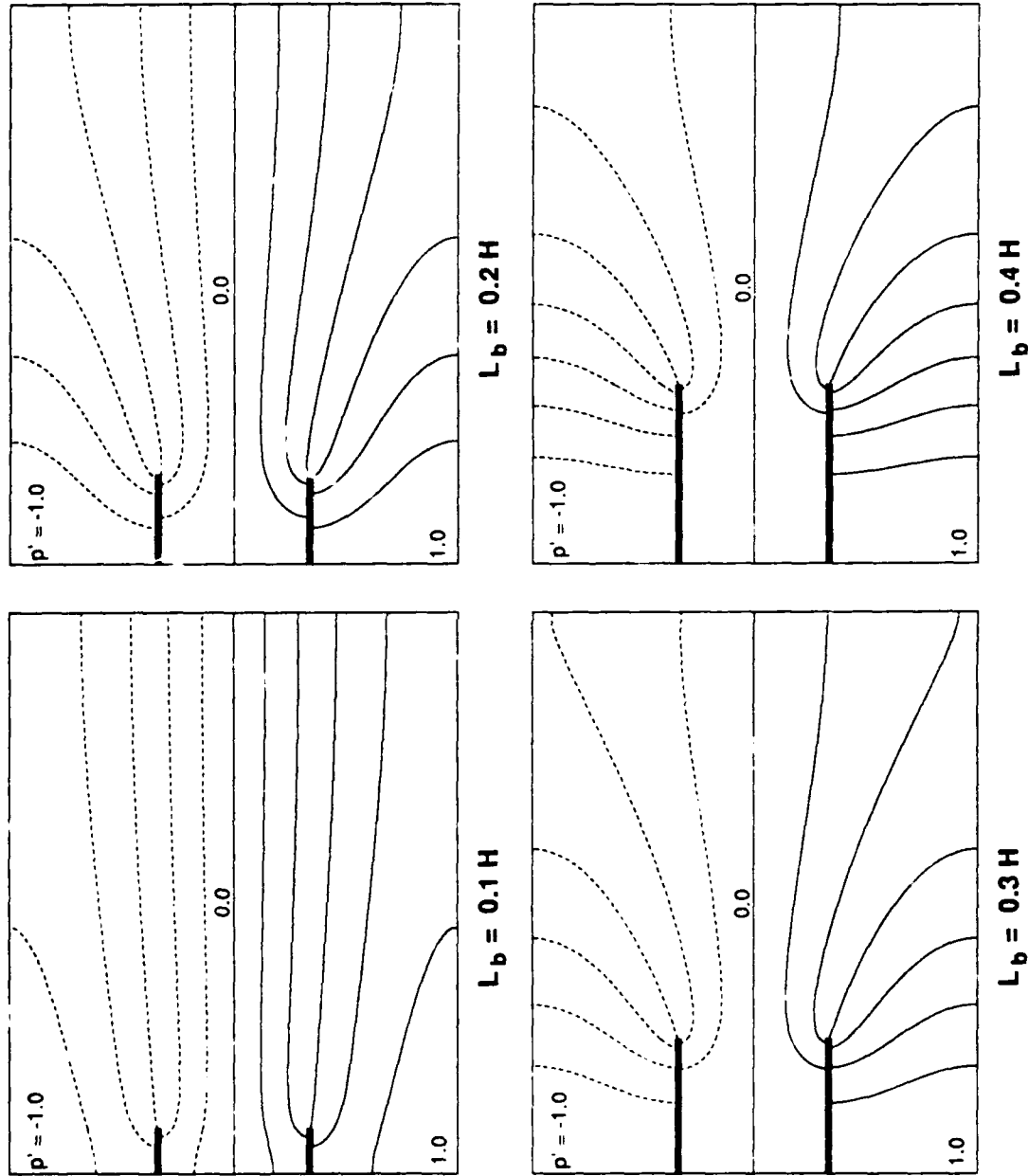


Figure 3.5 Effect of Baffle Length on the Acoustic Pressure Field in a Two-Baffle Chamber; the First Transverse Mode

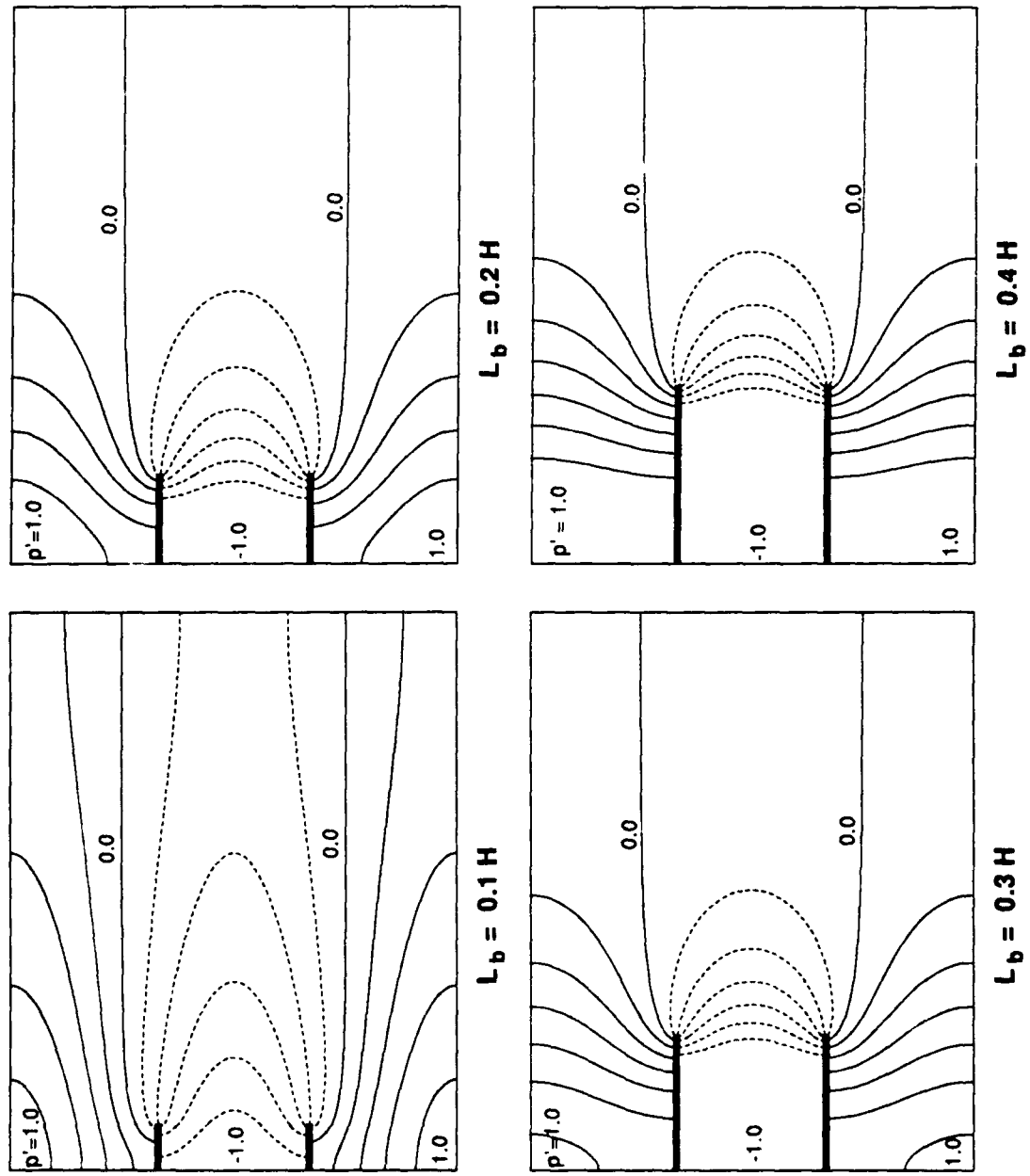


Figure 3.6 Effect of Baffle Length on the Acoustic Pressure Field in a Two-Baffle Chamber; the Second Transverse Mode

to the first mode case. However, large-amplitude bulk oscillations now exist in the center region. If pressure sensitive processes are responsible for the instability, this concentrated pressure fluctuation could promote instability. The effect of acoustic velocity on unsteady combustion, however, is quite limited in the baffle compartments, especially in the center one. According to the experiments of Levine and Bambanek<sup>38</sup> and Reardon,<sup>35</sup> transverse components of the acoustic velocity have a strong effect on the combustion process. For instance, atomization, local mixture ratio, and adjacent injector element interactions can all be affected by acoustic velocity fluctuations in the transverse direction. Near the injector face, where large temperature and concentration gradients are found, this effect can be especially pronounced. From Fig. 3.7, however, it is clear that the transverse components are very small near the injector face inside the baffle compartments. Figure 3.7 shows the acoustic pressure and velocity vector together for the first transverse mode in a two-baffle chamber.

So for an unbaffled chamber in which a transverse mode of instability arises from velocity sensitive processes, addition of baffles will likely have a stabilizing effect. Thus, the longitudinalization of transverse oscillations brought about by the baffle can be supposed to have stabilizing or destabilizing effects, depending primarily on the relative importance of pressure sensitive and velocity sensitive combustion processes.

The second transverse mode for the one-baffle chamber and the third transverse mode for the two-baffle chamber are also examined, as shown in Fig. 3.8. The acoustic fields are almost identical to those in an unbaffled chamber, showing

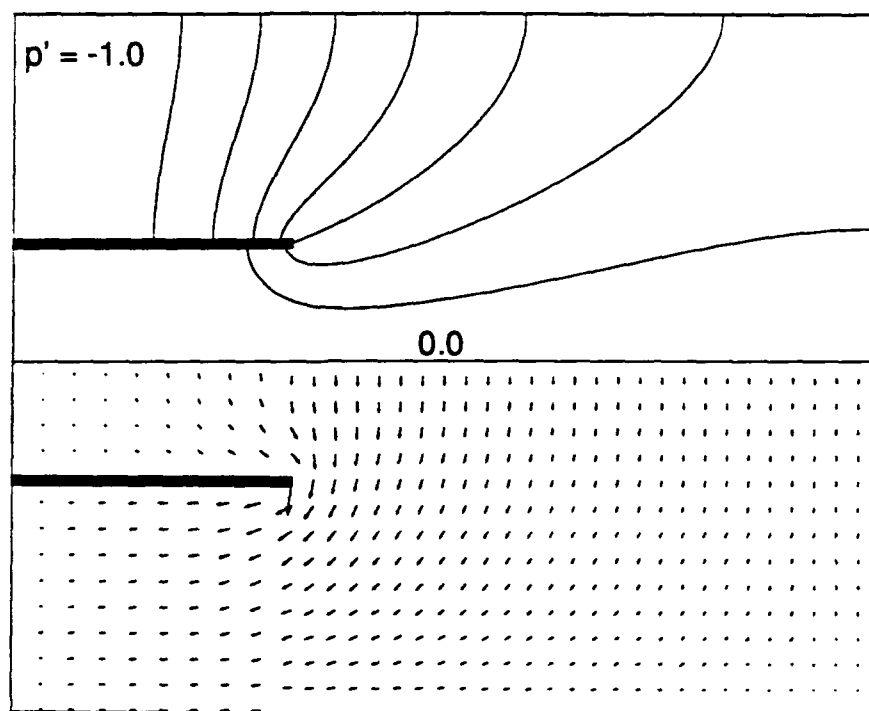
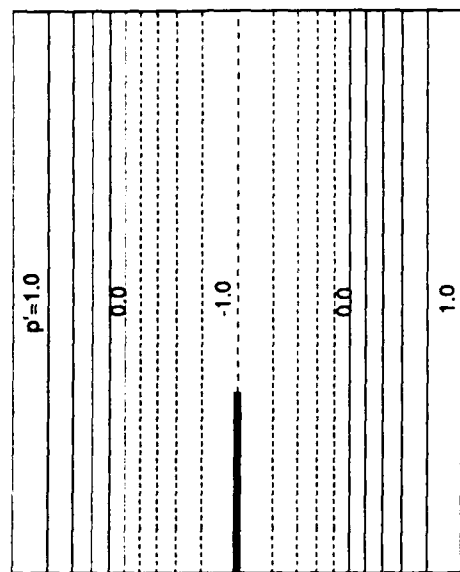
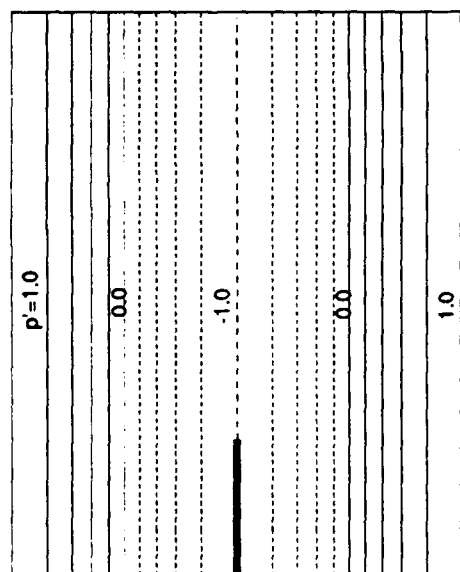


Figure 3.7 Acoustic Pressure and Velocity for the First Transverse Mode in a Two-Baffle Chamber

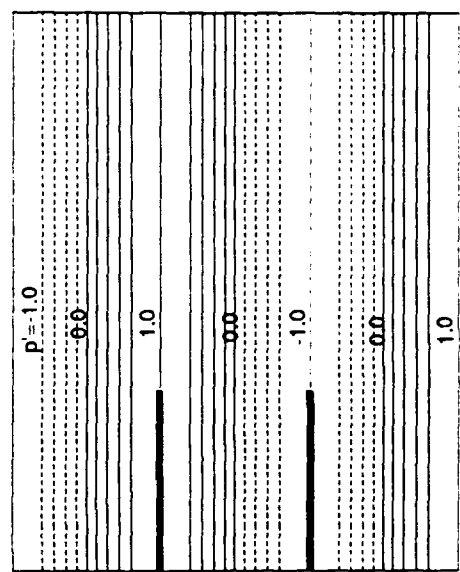


$L_b = 0.4 H$

(a) One-Baffle Chamber; the Second Transverse Mode

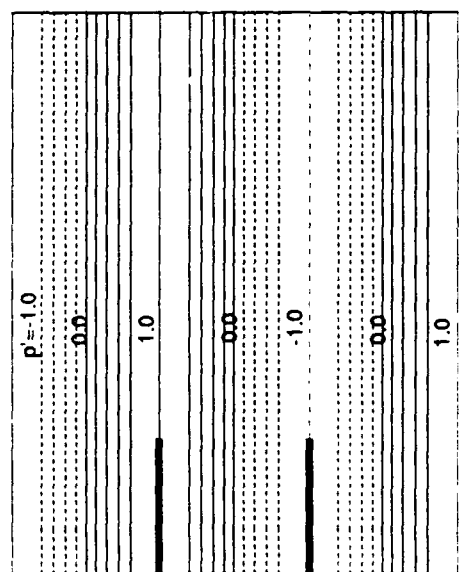


$L_b = 0.3 H$



$L_b = 0.4 H$

(b) Two-Baffle Chamber; the Third Transverse Mode



$L_b = 0.3 H$

Figure 3.8 Effect of Baffle Length on the Acoustic Pressure Field

that the baffles have little effect on these transverse modes because the boundary conditions imposed by the baffle blades are automatically satisfied if they are located at the acoustic pressure anti-nodal (or the velocity nodal) lines.

The effect of baffle length on the oscillation frequency is also studied. Comparison with the numerical (ANSYS) results is made again, since no appropriate experimental data was found. Figure 3.9 presents the results for the first transverse mode in a one-baffle chamber, where the frequency is normalized with respect to the natural frequency of an un baffled chamber. Excellent agreement is observed between the analytical predictions and the finite-element calculations, with relative errors of less than one percent. The frequency decreases persistently with increased baffle length, perhaps due to an increase in the effective path length of the gas particles, as caused by the baffle blade. This same trend can also be observed in actual three-dimensional engine tests. For a baffle length of  $0.4H$ , the reduction of frequency from that of the un baffled chamber is greater than 25%. The ensuing influence on the liquid-propellant combustion response can be significant and must be taken into account in a realistic treatment of combustion instabilities in baffled combustors. Since combustion instability depends on a specific relationship between the acoustic frequency and the characteristic response time of combustion processes, sufficient modification of the oscillation frequency will probably lessen the amount of acoustic/combustion coupling, and might terminate the instability altogether. Thus decreasing oscillation frequency is another potential stabilizing effect of the baffles on the chamber.

It should be noted that numerical calculations using ANSYS takes several hours

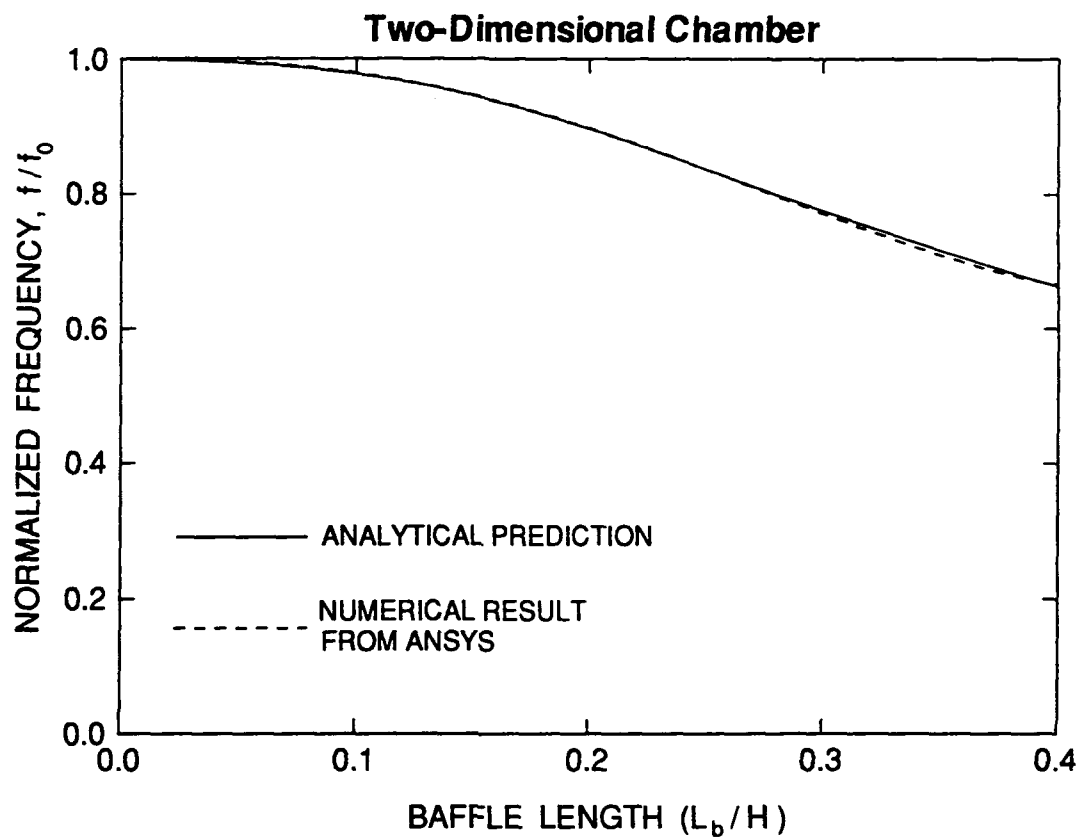
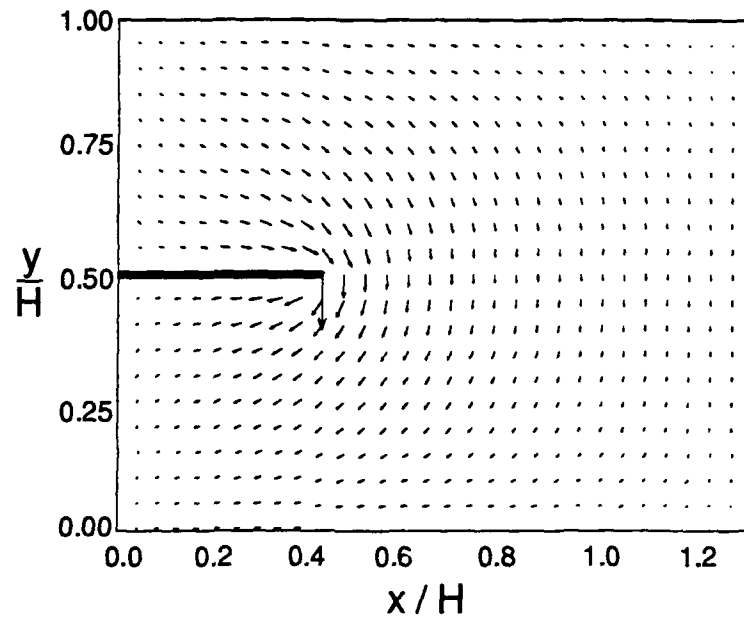


Figure 3.9 Effect of Baffle Length on the Frequency of the First Transverse Mode; Two-Dimensional Chamber

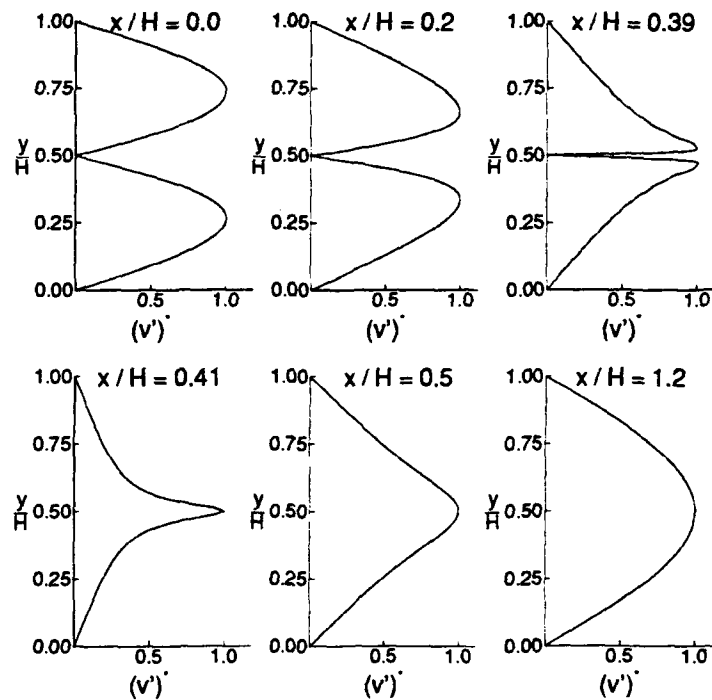
on the VAX-8700 system, but only a few minutes is required to get analytical results with 40 terms in the eigenfunction expansion. This suggests that this analysis has many strong features.

As mentioned before, a critical issue in the study of liquid rocket combustion instability is the effect of acoustic velocity on propellant combustion. In consideration of this point, the acoustic velocity field is calculated in detail, giving the result shown in Fig. 3.10. The acoustic velocity reaches its maximum amplitude due to the large pressure gradient near the baffle tip, then decreases in the far field. The transverse components of the acoustic velocity are generally much larger than the axial components just downstream of the baffle tip, since the acoustic wave front must turn 180 degrees around the baffle. Figure 3.10(b) shows the distributions of transverse acoustic velocity at various axial locations, where  $(v')^*$  stands for the velocity normalized with respect to its maximum value in the transverse plane at the given axial location. In the baffle compartment ( $x < 0.4H$ ), the requirement for transverse acoustic velocity to vanish at the baffle blade causes two peaks in the velocity profile. The profile then becomes a simpler distribution downstream of the baffle, with a single peak at the centerline. Note that the magnitude of the transverse velocity components near the injector face is negligibly small due to the longitudinalization of the wave there.

Near the baffle tip, however, large magnitudes and a rapid variation in the velocity profile are observed. Furthermore, the large gradients of acoustic pressure observed near the baffle tip provide sizable centripetal forces as the wave turns 180 degrees around the baffle tip in satisfaction of the geometric condition set by



(a) Acoustic Vector Plot



(b) Distribution of Transverse Acoustic Velocity at Various Axial Locations

Figure 3.10 Acoustic Velocity Field of the First Transverse Mode in a One-Baffle Chamber

the baffle. Baer and Mitchell<sup>31</sup> claimed that viscous dissipation of acoustic energy due to these rapid variations of acoustic velocity is crucial in stabilizing the baffled rocket engine. It is worth noting here that the drastic change of acoustic velocity near the baffle tip should lead to the formation of vortices, which are convected downstream in the presence of mean flow. In the case of oscillatory flow past a baffle compartment, it might be expected that vortices are also created in the compartments, with the direction of rotation alternating in response to the flow past the baffle.<sup>25</sup> Such creation and destruction of vortices may provide for energy dissipation that is significant in certain cases. However, the longitudinalization of flow in the compartments suggests that downstream shedding of vortices is more important, especially in the case of the longer baffles. The subsequent influence of these vortices on the mean flowfield may also significantly alter the combustion distribution and instability characteristics, and is addressed by Wicker<sup>32</sup> in a systematic fashion.

### 3.4.2 Acoustic Field in Three-Dimensional Baffled Chamber

Calculations are also carried out for acoustic fields in three-dimensional cylindrical chambers with radial baffles, thereby simulating more realistic rocket engine configurations.

Figure 3.11 presents the normalized frequency of the first tangential mode as a function of the baffle length and the number of blades. Good agreement with experimental data<sup>20,22,54,55</sup> was obtained. As with the two-dimensional case, the oscillation frequency decreases with baffle length due to the increased acoustic

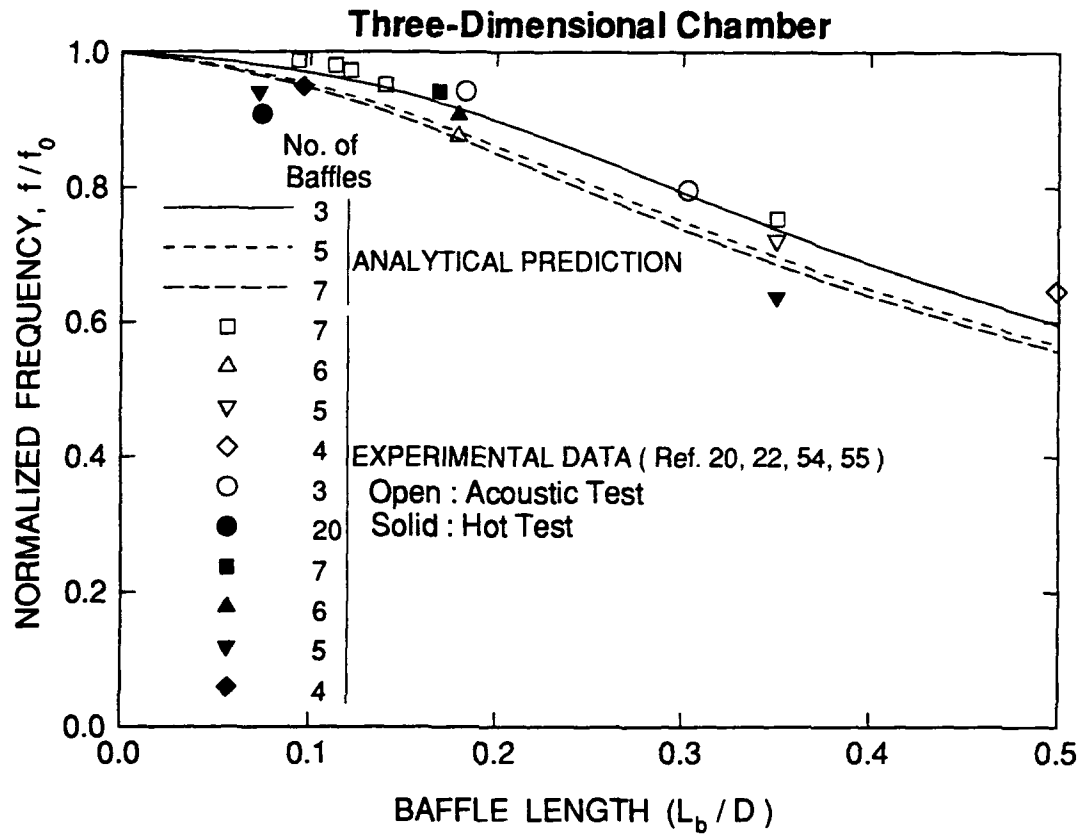


Figure 3.11 Effect of Baffle Length on the Frequency of the First Tangential Mode; Three-Dimensional Chamber

path length around the baffle blades. This depression of the oscillation frequencies can eliminate acoustic/combustion coupling in the chamber, or perhaps alter the chamber mode so that the instability may be avoided. This phenomenon might serve as one of the stabilizing effects of the baffles. It is also interesting to mention that the number of baffle blades plays a minor role in determining the frequency. Increasing the number of blades from three to seven only slightly decreases the frequency, a phenomenon also supported by experimental data. This aspect is understandable considering that when more than three baffle blades are used, the first tangential mode is always affected, regardless of the number of blades.

Figure 3.12 shows the acoustic pressure contours at various cross sections in a chamber with three radial baffle blades. This baffle configuration is the simplest one that can get rid of first tangential mode instability, which is the most often seen and the most troublesome in the actual rocket systems. The wave resembles a classical tangential mode in the downstream end of the chamber (i.e.  $x/L = 1.0$ ), but the pressure contours become distorted near the baffle tips, and finally reach a symmetric pattern dictated by the geometric constraints of the baffle blades. As seen for the two-dimensional case, unsteady motions in the injector end of the baffle compartments have a more longitudinal or even bulk type oscillation, with a quite uniform transverse spatial distribution.

Also important is that the pressure amplitude is higher than that in the main chamber. This peculiar phenomenon suggests that the baffle tends to redistribute the acoustic energy in the chamber from the downstream to the upstream region. Usually most of the energy release from liquid propellant occurs in the upstream

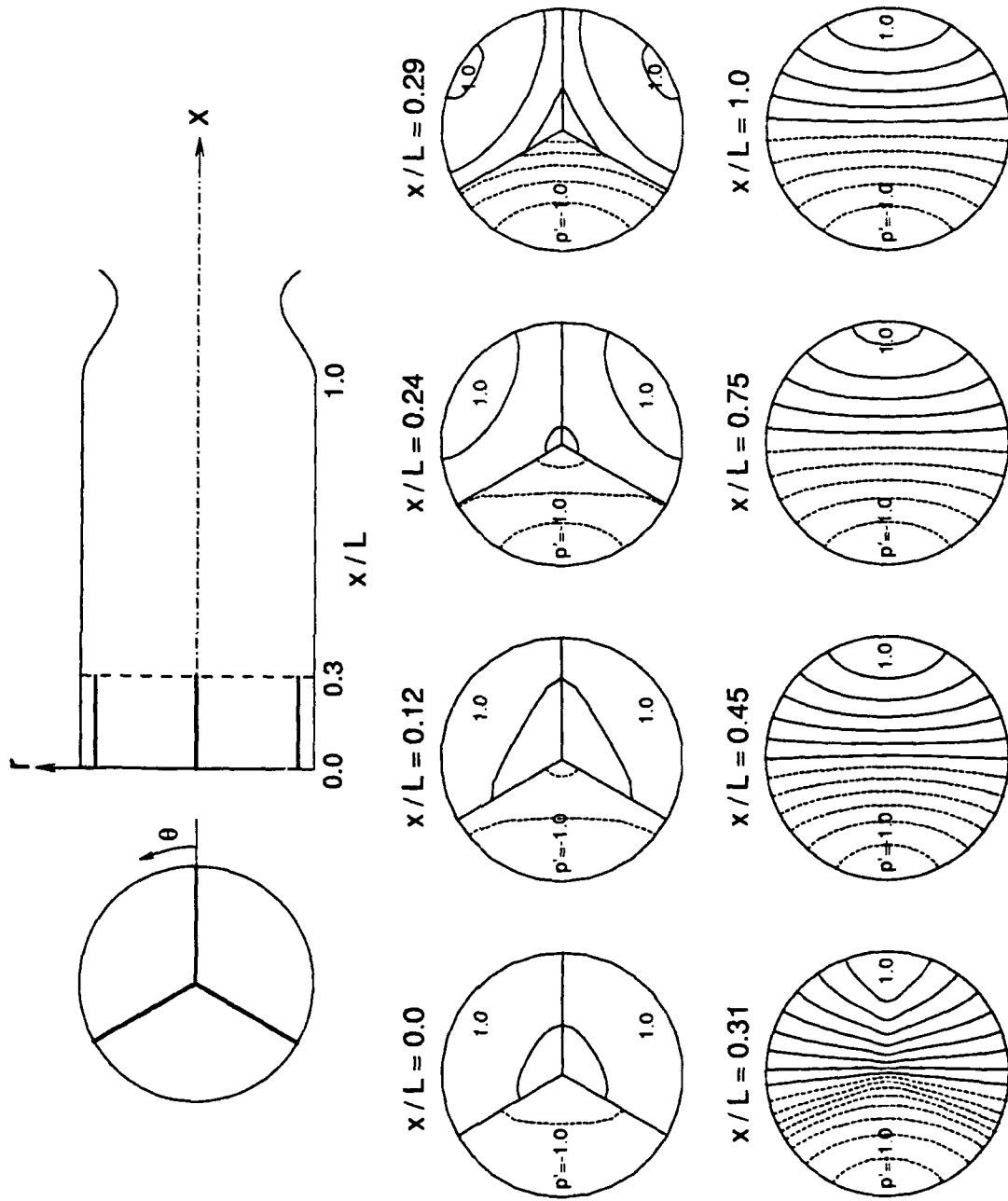


Figure 3.12 Acoustic Pressure Contours of the First Tangential Mode at Various Cross Sections of a Three-Dimensional Baffled Chamber

region. The high-amplitude acoustic pressure in that region has the potential to release larger amounts of energy, and could have a net destabilizing effect on the engine. This mechanism is formalized in terms of Rayleigh's criterion,<sup>29</sup> which states that if a pulse of heat is added at a time and location where the acoustic pressure is increasing, the pressure rise is encouraged and hence the heat addition has a destabilizing effect. However, as was already noted in two-dimensional results, the characteristics of the wave motions in the baffle compartments are significantly changed. Under further considerations, this pressure concentration may not destabilize the engines.

Figure 3.13 presents the transverse acoustic velocity vectors at various cross sections. The acoustic velocities in the baffle compartments have very small amplitudes, especially near the injector face, where large temperature and concentration gradients exist. Since the transverse components of acoustic velocity would be expected to have little effect on the combustion processes in that region, addition of baffle blades in the chamber could yield a stabilizing effect, especially if velocity sensitive combustion processes are of primary concern. Large-amplitude velocity oscillations exist immediately downstream of the baffles, which is similar to the two-dimensional case. The large acoustic velocity gradients in this region lead to the formation of vortices, which are convected downstream by the mean flow. Viscous dissipation within each vortex and convection of energy associated with the vortical structure out of the chamber may be a significant mechanism of energy dissipation.<sup>32</sup> Also, the influences of these vortices on the mean flowfield might change the combustion distribution and instability characteristics.

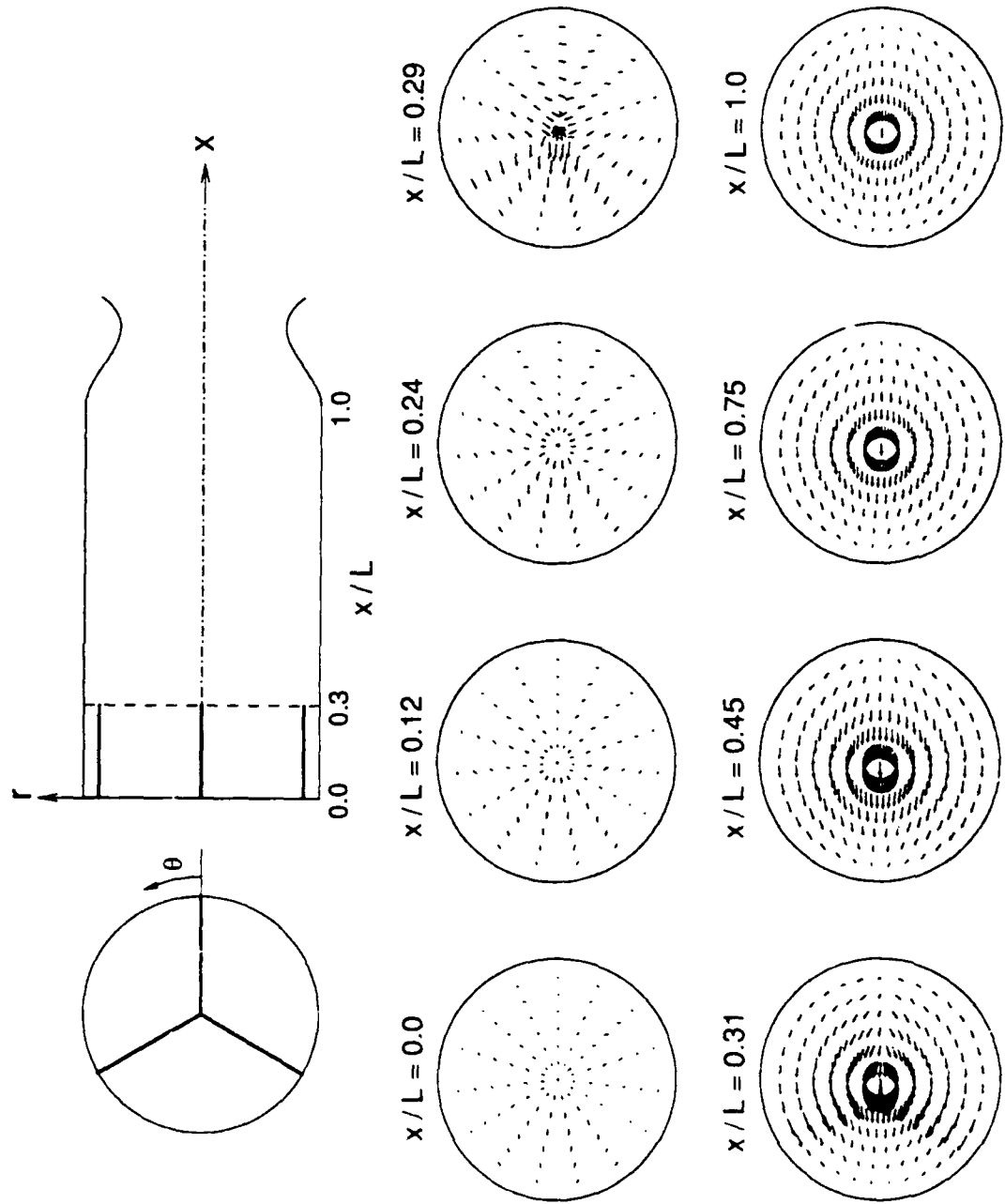


Figure 3.13 Acoustic Velocity Vectors of the First Tangential Mode

## CHAPTER 4

## NONLINEAR SPINNING TRANSVERSE OSCILLATIONS

Before dealing with the nonlinear acoustic analysis in the baffled combustion chamber, this chapter addresses the characteristics of spinning wave motions in a cylindrical unbaffled chamber. Spinning transverse oscillations are quite often observed in many types of combustion chambers and are known to be detrimental due to the increasing combustion efficiency through the acceleration of mixing processes. The purpose of this chapter is to examine how the spinning wave motions are related to the velocity coupling, and the conditions for which stable limit cycles exist for the special cases of combinations of spinning modes.

## 4.1 Problem Formulation

The solution of the wave equation (2.29) in a cylindrical unbaffled chamber is approximated by a synthesis of the normal modes of the chamber, with unknown time-varying amplitudes  $\eta_n(t)$ ,

$$p' = \bar{p} \sum_{n=1}^{\infty} \eta_n(t) \psi_n(\mathbf{r}) \quad (4.1a)$$

The corresponding velocity field is

$$\mathbf{u}'_g = \sum_{n=1}^{\infty} \frac{\dot{\eta}_n(t)}{\bar{\gamma} k_n^2} \nabla \psi_n(\mathbf{r}) \quad (4.1b)$$

where  $\psi_n(\mathbf{r})$  is a normal mode function satisfying

$$\nabla^2 \psi_n + k_n^2 \psi_n = 0 \quad (4.2a)$$

$$\mathbf{n} \cdot \nabla \psi_n = 0 \quad (4.2b)$$

A set of second-order ordinary differential equations for the time-varying amplitude of each mode can be obtained by averaging the conservation equations over the volume of the chamber using Galerkin's method. Now multiply Eq. (2.29) by  $\psi_n$  and Eq. (4.2a) by  $p'$ , subtract the results, integrate over the volume, and apply Green's theorem to find

$$\iiint \left( \frac{\psi_n}{\bar{a}^2} \frac{\partial^2 p'}{\partial t^2} + k_n^2 \psi_n p' \right) dV = - \iiint \psi_n h dV - \oiint \psi_n \mathbf{f} \cdot \mathbf{n} dS \quad (4.3)$$

Substitution of Eq. (4.1) into Eq. (4.3) and some rearrangements of the results lead to a system of second-order ordinary differential equations for the time-dependent amplitudes.

$$\ddot{\eta}_n + \omega_n^2 \eta_n = F_n \quad (4.4)$$

where the forcing function  $F_n$  can be expressed

$$F_n = \frac{-\bar{a}^2}{\bar{p}E_n^2} \left[ \iiint \psi_n h dV + \oiint \psi_n \mathbf{f} \cdot \mathbf{n} dS \right] \quad (4.5a)$$

and

$$E_n^2 = \iiint \psi_n^2 dV \quad (4.5b)$$

The next step is to represent the forcing function  $F_n$  in terms of time-varying amplitudes  $\eta_n(t)$ . In this chapter, the main focus is on the influence of the linear interactions between modes on the spinning wave motions within the chamber, so that only the linear part of the forcing function is taken into consideration. The linear approximation of  $h_3$  in Eq. (2.30c) is

$$h_{3,lin} = -\frac{\bar{R}}{\bar{a}^2} \frac{\Delta H_v}{C_v} \frac{\partial}{\partial t} \dot{\omega}'_i \quad (4.6)$$

where  $\Delta H_v$  is the heat of combustion of the liquid propellant per unit mass. This expression is not complete until the burning rate is represented in terms of flow variables. Such closure of the solution is conveniently accomplished through the use of the combustion response function concept. The original definition of the combustion response function uses only pressure for representing the burning rate, but according to Reardon,<sup>35</sup> the transverse velocity components play an important role on the burning rate fluctuation for the spinning mode of oscillations. In this analysis, the velocity coupling effect, as well as the pressure coupling, is incorporated with the combustion response function to express the burning rate. The unsteady combustion is modeled as

$$\frac{\dot{\omega}'_l}{\dot{\omega}_l} = \mathcal{R}_p \frac{p'}{\bar{p}} + \mathcal{R}_v \frac{v'}{\bar{a}} + \mathcal{R}_w \frac{w'}{\bar{a}} \quad (4.7)$$

where  $v'$  and  $w'$  are acoustic velocity perturbations in the radial and tangential directions, respectively; the pressure-coupled, radial and tangential velocity-coupled response functions are symbolized by  $\mathcal{R}_p$ ,  $\mathcal{R}_v$  and  $\mathcal{R}_w$ , respectively. For the linear acoustic problems, all variables are assumed to vary in a time-harmonic fashion, e.g.,

$$p'(\mathbf{r}, t) = \hat{p}(\mathbf{r})e^{i\Omega t} \quad (4.8)$$

$$\vdots$$

Since the combustion response function should account for both the amplitude and the phase relationship between flow variables and burning rate perturbation, the complex expressions for  $\mathcal{R}_p$ ,  $\mathcal{R}_v$  and  $\mathcal{R}_w$  are required, thus, Eq. (4.7) is rewritten

as the sum of its real and imaginary parts.

$$\begin{aligned} \frac{\dot{\omega}'_l}{\bar{\omega}_l} = & \mathcal{R}e(\mathcal{R}_p) \frac{p'}{\bar{p}} + \frac{1}{\bar{p}\Omega} \mathcal{I}m(\mathcal{R}_p) \frac{\partial p'}{\partial t} \\ & + \mathcal{R}e(\mathcal{R}_v) \frac{v'}{\bar{a}} + \frac{1}{\bar{a}\Omega} \mathcal{I}m(\mathcal{R}_v) \frac{\partial v'}{\partial t} \\ & + \mathcal{R}e(\mathcal{R}_w) \frac{w'}{\bar{a}} + \frac{1}{\bar{a}\Omega} \mathcal{I}m(\mathcal{R}_w) \frac{\partial w'}{\partial t} \end{aligned} \quad (4.9)$$

Then, the linear approximation of the combustion response related source term  $(h_{3lin})_{CR}$  takes the form,

$$\begin{aligned} (h_{3lin})_{CR} = & -\frac{1}{a^2} \left[ G_{1n} \frac{\partial p'}{\partial t} + G_{2n} \frac{\partial^2 p'}{\partial t^2} \right. \\ & + H_{1n} \frac{\partial v'}{\partial t} + H_{2n} \frac{\partial^2 v'}{\partial t^2} \\ & \left. + I_{1n} \frac{\partial w'}{\partial t} + I_{2n} \frac{\partial^2 w'}{\partial t^2} \right] \end{aligned} \quad (4.10a)$$

where,

$$\begin{aligned} G_{1n} &= \frac{\bar{R}}{\bar{C}_v} \frac{\bar{\omega}_l \mathcal{R}e(\mathcal{R}_p) \Delta H_v}{\bar{p}} \\ G_{2n} &= \frac{\bar{R}}{\bar{C}_v} \frac{\bar{\omega}_l \mathcal{I}m(\mathcal{R}_p) \Delta H_v}{\Omega \bar{p}} \\ H_{1n} &= \frac{\bar{R}}{\bar{C}_v} \frac{\bar{\omega}_l \mathcal{R}e(\mathcal{R}_v) \Delta H_v}{\bar{a}} \\ H_{2n} &= \frac{\bar{R}}{\bar{C}_v} \frac{\bar{\omega}_l \mathcal{I}m(\mathcal{R}_v) \Delta H_v}{\Omega \bar{a}} \\ I_{1n} &= \frac{\bar{R}}{\bar{C}_v} \frac{\bar{\omega}_l \mathcal{R}e(\mathcal{R}_w) \Delta H_v}{\bar{a}} \\ I_{2n} &= \frac{\bar{R}}{\bar{C}_v} \frac{\bar{\omega}_l \mathcal{I}m(\mathcal{R}_w) \Delta H_v}{\Omega \bar{a}} \end{aligned} \quad (4.10b)$$

Because the combustion response function is a function of frequency, all coefficients in Eq. (4.10b) are also functions of the frequency and have different values for each mode of oscillations.

If the series expansions for  $\mathbf{u}'_g$  and  $p'$  in Eq. (4.1) and the linear approximation of combustion response related source term  $(h_{3lin})_{CR}$  in Eq. (4.10a) are substituted into Eq. (4.5), the linear part of the forcing function then becomes

$$(F_n)_{linear} = - \sum_{i=1}^{\infty} (D_{ni}\dot{\eta}_i + E_{ni}\eta_i) \quad (4.11)$$

where the linear coefficients  $D_{ni}$  and  $E_{ni}$  are given by,

$$\begin{aligned} D_{ni} = & \frac{1}{E_n^2} \iiint \left[ \left[ 1 + \frac{k_n^2}{k_i^2} \right] \psi_n \bar{\mathbf{u}}_g \cdot \nabla \psi_i \right. \\ & - \frac{1}{k_i^2} [\nabla \psi_i \times (\nabla \times \bar{\mathbf{u}}_g)] \cdot \nabla \psi_n + \bar{\gamma} \psi_i \psi_n \nabla \cdot \bar{\mathbf{u}}_g \\ & \left. - G_{1n} \psi_i \psi_n + \frac{H_{2n}}{\bar{\rho}} \frac{\partial \psi_i}{\partial r} \psi_n + \frac{I_{2n}}{\bar{\rho}} \frac{1}{r} \frac{\partial \psi_i}{\partial \theta} \psi_n \right] dV \quad (4.12a) \end{aligned}$$

$$E_{ni} = \frac{1}{E_n^2} \iiint \left[ G_{2n} k_i^2 \psi_i \psi_n \bar{a}^2 + \frac{H_{1n}}{\bar{\rho}} \frac{\partial \psi_i}{\partial r} \psi_n + \frac{I_{1n}}{\bar{\rho}} \frac{1}{r} \frac{\partial \psi_i}{\partial \theta} \psi_n \right] dV \quad (4.12b)$$

Here, the linear interaction effects between modes represented by the coefficients in Eq. (4.10b) are incorporated with the linear parameters in Eq. (4.12).

For the standing mode of oscillations, each tangential motion has only one mode shape in the azimuthal direction. Therefore, the linear coupling between modes cannot exist, even though the linear contribution of the combustion response is considered. For the spinning mode of oscillations, however, two periodic motions in a tangential direction are possible. That is, the combination of  $\psi_n = \cos m\theta J_m(\kappa_{ms}r)$  and  $\psi_i = \sin m\theta J_m(\kappa_{ms}r)$  is possible for the spinning transverse oscillations. For the first three modes, the wave numbers and mode shapes are given by,

First Tangential Mode (1T)

$$\kappa_{11}R = 1.8412; \quad \psi_1 = \cos \theta J_1(\kappa_{11}r), \quad \psi_4 = \sin \theta J_1(\kappa_{11}r) \quad (4.13a)$$

First Radial Mode (1R)

$$\kappa_{01}R = 3.8317; \quad \psi_2 = J_0(\kappa_{01}r) \quad (4.13b)$$

Second Tangential Mode (2T)

$$\kappa_{21}R = 3.0542; \quad \psi_3 = \cos 2\theta J_2(\kappa_{21}r), \quad \psi_5 = \sin 2\theta J_2(\kappa_{21}r) \quad (4.13c)$$

The linear coefficients  $D_{ni}$  and  $E_{ni}$  can be computed from Eq. (4.12) for the first three modes. Unlike Yang and Culick's standing mode analysis,<sup>47</sup> the linear coupling coefficients,  $D_{14}$ ,  $E_{14}$ ,  $D_{41}$ , and  $E_{41}$  appear for the first tangential mode and  $D_{35}$ ,  $E_{35}$ ,  $D_{53}$  and  $E_{53}$  for the second tangential mode, with the following values.

$$\begin{aligned} D_{11} &= D_{44} = -G_{11} + \frac{H_{21}}{\bar{\rho}} A_1 \\ D_{22} &= -G_{12} + \frac{H_{22}}{\bar{\rho}} A_2 \\ D_{33} &= D_{55} = -G_{13} + \frac{H_{23}}{\bar{\rho}} A_3 \\ D_{14} &= -D_{41} = \frac{I_{21}}{\bar{\rho}} A_4 \\ D_{35} &= -D_{53} = \frac{I_{23}}{\bar{\rho}} A_5 \end{aligned} \quad (4.14a)$$

And

$$\begin{aligned} E_{11} &= E_{44} = G_{21}\omega_1^2 + \frac{H_{11}}{\bar{\rho}} A_1 \\ E_{22} &= G_{22}\omega_2^2 + \frac{H_{12}}{\bar{\rho}} A_2 \end{aligned}$$

$$\begin{aligned}
E_{33} &= E_{55} = G_{23}\omega_3^2 + \frac{H_{13}}{\bar{\rho}}A_3 \\
E_{14} &= -E_{41} = \frac{I_{11}}{\bar{\rho}}A_4 \\
E_{35} &= -E_{53} = \frac{I_{13}}{\bar{\rho}}A_5
\end{aligned} \tag{4.14b}$$

where

$$A_1 = \frac{\kappa_{1s}}{(1 - \frac{1}{\kappa_{1s}^2 R^2}) [J_1(\kappa_{1s} R)]^2} \int_0^R r J_1(\kappa_{1s} r) [J_0(\kappa_{1s} r) - J_2(\kappa_{1s} r)] dr \tag{4.15a}$$

$$A_2 = -\frac{2\kappa_{0s}}{R^2 [J_0(\kappa_{0s} R)]^2} \int_0^R r J_0(\kappa_{0s} r) J_1(\kappa_{0s} r) dr \tag{4.15b}$$

$$A_3 = \frac{\kappa_{2s}}{(1 - \frac{1}{\kappa_{2s}^2 R^2}) [J_2(\kappa_{2s} R)]^2} \int_0^R r J_2(\kappa_{2s} r) [J_1(\kappa_{2s} r) - J_3(\kappa_{2s} r)] dr \tag{4.15c}$$

$$A_4 = \frac{2}{R^2 (1 - \frac{1}{\kappa_{1s}^2 R^2}) [J_1(\kappa_{1s} R)]^2} \int_0^R [J_1(\kappa_{1s} r)]^2 dr \tag{4.15d}$$

$$A_5 = \frac{4}{R^2 (1 - \frac{1}{\kappa_{2s}^2 R^2}) [J_2(\kappa_{2s} R)]^2} \int_0^R [J_2(\kappa_{2s} r)]^2 dr \tag{4.15e}$$

An approximate solution technique using the method of time-averaging gives the temporal behavior of the amplitude. First of all, time-varying amplitudes  $\eta_n(t)$  are assumed to have the form,

$$\eta_n(t) = r_n(t) \sin[\omega_n t + \phi_n(t)] \tag{4.16}$$

where  $r_n(t)$  and  $\phi_n(t)$  are the amplitude and phase of the limit cycle, respectively. Using the linear coupling coefficients in Eq. (4.14) and applying the time-averaging method, the equations for time-varying amplitudes due to the combustion response are given by,

First Tangential Mode (1T)

$$\left(\frac{dr_1}{dt}\right)_{CR} = \alpha_{14}r_4 \cos(\phi_1 - \phi_4) - \theta_{14}r_4 \sin(\phi_1 - \phi_4) \quad (4.17a)$$

$$\left(\frac{dr_4}{dt}\right)_{CR} = \alpha_{41}r_1 \cos(\phi_1 - \phi_4) + \theta_{41}r_1 \sin(\phi_1 - \phi_4) \quad (4.17b)$$

$$\left(r_1 \frac{d\phi_1}{dt}\right)_{CR} = -\alpha_{14}r_4 \sin(\phi_1 - \phi_4) - \theta_{14}r_4 \cos(\phi_1 - \phi_4) \quad (4.17c)$$

$$\left(r_4 \frac{d\phi_4}{dt}\right)_{CR} = \alpha_{41}r_1 \sin(\phi_1 - \phi_4) - \theta_{41}r_1 \cos(\phi_1 - \phi_4) \quad (4.17d)$$

Second Tangential Mode (2T)

$$\left(\frac{dr_3}{dt}\right)_{CR} = \alpha_{35}r_5 \cos(\phi_3 - \phi_5) - \theta_{35}r_5 \sin(\phi_3 - \phi_5) \quad (4.18a)$$

$$\left(\frac{dr_5}{dt}\right)_{CR} = \alpha_{53}r_3 \cos(\phi_3 - \phi_5) + \theta_{53}r_3 \sin(\phi_3 - \phi_5) \quad (4.18b)$$

$$\left(r_3 \frac{d\phi_3}{dt}\right)_{CR} = -\alpha_{35}r_5 \sin(\phi_3 - \phi_5) - \theta_{35}r_5 \cos(\phi_3 - \phi_5) \quad (4.18c)$$

$$\left(r_5 \frac{d\phi_5}{dt}\right)_{CR} = \alpha_{53}r_3 \sin(\phi_3 - \phi_5) - \theta_{53}r_3 \cos(\phi_3 - \phi_5) \quad (4.18d)$$

where,

$$\alpha_{ni} = -D_{ni}/2 \quad \theta_{ni} = -E_{ni}/2\omega_n \quad (4.19)$$

**4.2 Nonlinear Spinning Oscillations**

Equations for time-varying amplitudes due to the combustion response in Section 4.1 are combined with those in Ref. 47 to investigate the nonlinear spinning transverse oscillations. For simplicity, only the first three modes (1T, 1R and 2T)—the most commonly observed in practical systems—are considered here.

Four simple combinations of modes are examined for the spinning wave motions: the first tangential mode, the first tangential/first radial modes, and the first tangential/second tangential modes. After this, the combination of three modes is discussed. The conditions for which the limit cycles exist are studied for each case, and the influence of linear coupling parameters on the spinning wave motions is also investigated.

#### 4.2.1 First Tangential Mode

The first tangential mode alone can exhibit the spinning wave motion if the linear coupling terms are taken into account. Equations of time-varying amplitudes and phases due to the combustion response (Section 4.1) are added to those of transverse oscillations in Ref. 47.

$$\frac{dr_1}{dt} = \alpha_1 r_1 + \alpha_{14} r_4 \cos X - \theta_{14} r_4 \sin X \quad (4.20)$$

$$\frac{dr_4}{dt} = \alpha_4 r_4 + \alpha_{41} r_1 \cos X + \theta_{41} r_1 \sin X \quad (4.21)$$

$$\begin{aligned} \frac{dX}{dt} = & -(\theta_1 - \theta_4) \\ & - \left[ \frac{\theta_{14} r_4}{r_1} - \frac{\theta_{41} r_1}{r_4} \right] \cos X - \left[ \frac{\alpha_{14} r_4}{r_1} + \frac{\alpha_{41} r_1}{r_4} \right] \sin X \end{aligned} \quad (4.22)$$

where,

$$X = \phi_1 - \phi_4 \quad (4.23)$$

The relations between linear parameters are easily found as follows,

$$\begin{aligned} \alpha_1 &= \alpha_4, \quad \theta_1 = \theta_4 \\ \alpha_{14} &= -\alpha_{41}, \quad \theta_{14} = -\theta_{41} \end{aligned} \quad (4.24)$$

Similar to the standing mode analysis,<sup>47</sup> the limiting values of amplitude  $r_n$  and phase  $\phi_n$  are given in the following form,

$$r_{n0} = \text{constant} \quad (4.25a)$$

$$\phi_{n0} = \nu_n t + \xi_n \quad (4.25b)$$

The subscript 0 denotes the value in the limit cycle. Combining Eqs. (4.23) and (4.25) gives

$$\nu_1 = \nu_4 \quad (4.26a)$$

$$X_0 = \xi_1 - \xi_4 \quad (4.26b)$$

At the limit cycle, then, Eqs. (4.20)-(4.22) become

$$0 = \alpha_1 r_{10} + \alpha_{14} r_{40} \cos X_0 - \theta_{14} r_{40} \sin X_0 \quad (4.27)$$

$$0 = \alpha_4 r_{40} + \alpha_{41} r_{10} \cos X_0 + \theta_{41} r_{10} \sin X_0 \quad (4.28)$$

$$0 = -(\theta_1 - \theta_4) - \left[ \frac{\theta_{14} r_{40}}{r_{10}} - \frac{\theta_{41} r_{10}}{r_{40}} \right] \cos X_0 - \left[ \frac{\alpha_{14} r_{40}}{r_{10}} + \frac{\alpha_{41} r_{10}}{r_{40}} \right] \sin X_0 \quad (4.29)$$

The practical assumption in a reasonable sense is taken for the limiting amplitudes.

$$r_{10} = r_{40} \quad (4.30)$$

After some manipulations of Eqs. (4.27)-(4.29), the relation between frequency modulations is obtained as,

$$\xi_1 = \xi_4 + \frac{(2n+1)\pi}{2} \quad (n = 1, 2, 3 \dots) \quad (4.31)$$

This means that mode 1 and mode 4 have a phase difference of either  $\frac{\pi}{2}$  or  $\frac{3\pi}{2}$  at the limit cycle. On the other hand, acoustic pressure for the first tangential mode is

$$\begin{aligned} p'(\mathbf{r}, t)/\bar{p} = & r_{10} \sin(\omega_1 t + \phi_{10}) \cos \theta J_1(\kappa_1 r) \\ & + r_{40} \sin(\omega_4 t + \phi_{40}) \sin \theta J_1(\kappa_1 r) \end{aligned} \quad (4.32)$$

Equation (4.32) can be further simplified using Eqs. (4.30) and (4.31),

$$p'(\mathbf{r}, t)/\bar{p} = r_{10} \sin[(\omega_1 + \nu_1)t + \xi_1 \pm \theta] J_1(\kappa_1 r) \quad (4.33)$$

Equation (4.33) shows that the spatial- and time-dependent parts of the first tangential mode are combined together, representing the spinning wave motion. Therefore, the first tangential mode alone may exhibit a spinning mode of oscillations if the linear coupling due to the combustion response is considered.

Next, check the condition for which the limit cycles exist. From Eqs. (4.27) and (4.28)

$$\alpha_1 = (-1)^n \theta_{14} \quad (n = 1, 2, 3 \dots) \quad (4.34)$$

This is the necessary and sufficient condition for the existence of limit cycles. The remaining task is to determine the conditions for which the limit cycle is stable. The procedure consists of examining small perturbations in the vicinity of the limit cycle. Substituting the relation  $r_n = r_{n0} + r'_n$ ,  $X = X_0 + X'$ , into the Eqs. (4.20)-(4.22) and neglecting the higher order terms yield a system of linearized equations. The solutions are assumed to vary exponentially in time and may be written in the form,  $r'_1 = \tilde{r}_1 \exp(\lambda t)$ , etc. This leads to a system of linear algebraic equations for

$\tilde{r}_n$ , and  $\tilde{X}$  in matrix form.

$$\begin{pmatrix} \alpha_1 - \lambda & (-1)^{n+1}\theta_{14} & (-1)^{n+1}\alpha_{14}r_{10} \\ (-1)^{n+1}\theta_{14} & \alpha_1 - \lambda & (-1)^n\alpha_{14}r_{10} \\ (-1)^n\frac{2\alpha_{14}}{r_{10}} & (-1)^{n+1}\frac{2\alpha_{14}}{r_{10}} & (-1)^n2\theta_{14} - \lambda \end{pmatrix} \begin{pmatrix} \tilde{r}_1 \\ \tilde{r}_4 \\ \tilde{X} \end{pmatrix} = 0 \quad (4.35)$$

For the non-trivial solutions, the determinant of the  $3 \times 3$  square matrix in Eq. (4.35) is equal to zero, giving the characteristic equation for  $\lambda$ .

$$P(\lambda) = \lambda^3 - 4\alpha_1\lambda^2 + [5\theta_{14}^2 + (-1)^{n+1}\theta_{14}^2 + \alpha_{14}^2] \lambda = 0 \quad (4.36)$$

Application of Routh-Hurwitz criteria gives the necessary and sufficient condition for the stable limit cycle.

$$\alpha_1 < 0 \quad (4.37)$$

Figure 4.1 shows the limit cycle of the first tangential mode with the condition (4.37) satisfied.

Let's examine this case from the acoustic energy conservation point of view at the limit cycle. Acoustic energy density is defined as

$$\langle \mathcal{E} \rangle = \frac{1}{2} \frac{p'^2}{\bar{\rho}\bar{a}^2} + \frac{1}{2} \bar{\rho} u'^2 \quad (4.38)$$

The total time-averaged energy of the combustion chamber is obtained using Eqs. (4.1) and (4.13).

$$\mathcal{E}_n = \text{constant} \cdot r_n^2 \quad (4.39)$$

Then, the rate of energy change of the system is

$$\frac{d\mathcal{E}_n}{dt} = \text{constant} \cdot r_n \frac{dr_n}{dt} \quad (4.40)$$

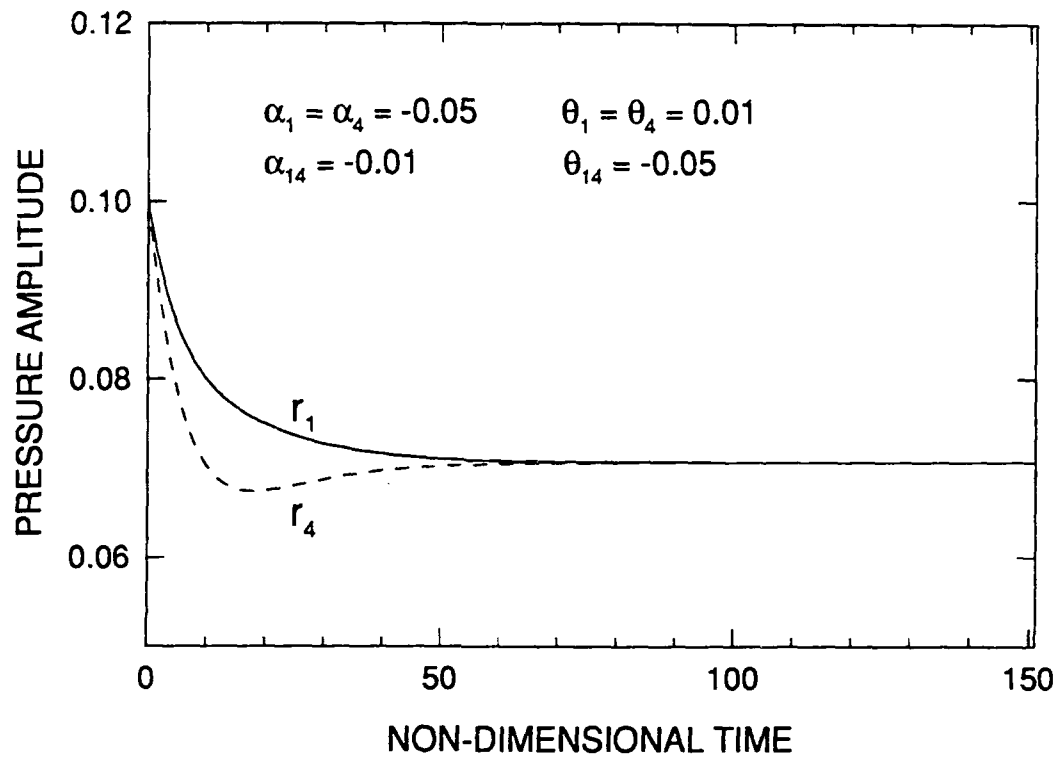


Figure 4.1 An Example Showing the Existence of Stable  
Limit Cycle, 1T Mode

Substituting Eqs. (4.20) and (4.21) into Eq. (4.40) and adding two equations using the relation (4.24) yield

$$\frac{d}{dt} [\mathcal{E}_1 + \mathcal{E}_4] = \alpha_1(r_1^2 + r_4^2) - 2\theta_{14}r_1r_4 \sin X \quad (4.41)$$

In the limit cycle,  $X$  approaches  $X_0$ , therefore, the right hand side of Eq. (4.41) vanishes due to the condition (4.34), which means that the acoustic energy is conserved. Since  $\alpha_1$  is negative, the first term of Eq. (4.41) represents the energy dissipated. And then, energy is supplied by the second term, which represents the linear coupling mechanism. Careful examination of linear coupling coefficient  $\theta_{14}$  reveals that the second term in Eq. (4.41) is closely related to the tangential velocity effect by the Eqs. (4.10b), (4.14) and (4.19). This means that the velocity-coupled response function (especially in the tangential direction) plays an essential role for the spinning mode of oscillations. This observation is consistent with Reardon's experiment<sup>35</sup> whereby the velocity effect has the strong destabilizing effects on the spinning mode of transverse oscillations.

#### 4.2.2 First Tangential/First Radial Modes

Next, the combination of the first tangential and first radial modes is studied. The mode shapes  $\psi_1$ ,  $\psi_4$  and  $\psi_2$  are taken into account. The equations governing the wave amplitudes and phases of each mode can be given by,

##### First Tangential Mode

$$\frac{dr_1}{dt} = \alpha_1 r_1 + a_1 r_1 r_2 \cos X$$

$$+\alpha_{14}r_4 \cos(\phi_1 - \phi_4) - \theta_{14}r_4 \sin(\phi_1 - \phi_4) \quad (4.42)$$

$$\begin{aligned} \frac{dr_4}{dt} = & \alpha_4 r_4 + a_1 r_2 r_4 \cos Y \\ & + \alpha_{41} r_1 \cos(\phi_1 - \phi_4) + \theta_{41} r_1 \sin(\phi_1 - \phi_4) \end{aligned} \quad (4.43)$$

First Radial Mode

$$\frac{dr_2}{dt} = \alpha_2 r_2 + b_1 [r_1^2 \cos X + r_4^2 \cos Y] \quad (4.44)$$

and

$$\begin{aligned} \frac{dX}{dt} = & -2\theta_1 - \theta_2 + \Omega_{12} - 2a_1 r_2 \sin X - \frac{b_1}{r_2} [r_1^2 \sin X + r_4^2 \sin Y] \\ & - \frac{2r_4}{r_1} [\theta_{14} \cos(\phi_1 - \phi_4) + \alpha_{14} \sin(\phi_1 - \phi_4)] \end{aligned} \quad (4.45)$$

$$\begin{aligned} \frac{dY}{dt} = & -2\theta_4 - \theta_2 + \Omega_{12} - 2a_1 r_2 \sin Y - \frac{b_1}{r_2} [r_1^2 \sin X + r_4^2 \sin Y] \\ & - \frac{2r_1}{r_4} [\theta_{41} \cos(\phi_1 - \phi_4) - \alpha_{41} \sin(\phi_1 - \phi_4)] \end{aligned} \quad (4.46)$$

where,

$$\begin{aligned} X(t) &= 2\phi_1 - \phi_2 + \Omega_{12}t \\ Y(t) &= 2\phi_4 - \phi_2 + \Omega_{12}t \end{aligned} \quad (4.47a)$$

$$\Omega_{12} = 2\omega_1 - \omega_2$$

$$\phi_1 - \phi_4 = (X - Y)/2$$

And the same values of  $a_1$ ,  $a_2$ ,  $b_1$  and  $b_2$  as those of Ref. 47 are used in this chapter

as,

$$\begin{aligned} a_1 &= 0.1570 \left( \frac{\bar{a}}{R} \right), & a_2 &= -0.0521 \left( \frac{\bar{a}}{R} \right) \\ b_1 &= -0.1054 \left( \frac{\bar{a}}{R} \right), & b_2 &= 0.1873 \left( \frac{\bar{a}}{R} \right) \end{aligned} \quad (4.47b)$$

The following relations are valid for the limit cycle.

$$\begin{aligned}\nu_1 &= \nu_4 \\ X_0 &= 2\xi_1 - \xi_2 \\ Y_0 &= 2\xi_4 - \xi_2\end{aligned}\quad (4.48)$$

The reasonable assumption (4.30) is used again; hence, at the limit cycle, Eqs. (4.42)-(4.46) become

$$0 = \alpha_1 + a_1 r_{20} \cos X_0 + \alpha_{14} \cos \frac{(X_0 - Y_0)}{2} - \theta_{14} \sin \frac{(X_0 - Y_0)}{2} \quad (4.49)$$

$$0 = \alpha_4 + a_1 r_{20} \cos Y_0 + \alpha_{41} \cos \frac{(X_0 - Y_0)}{2} + \theta_{41} \sin \frac{(X_0 - Y_0)}{2} \quad (4.50)$$

$$0 = \alpha_2 r_{20} + b_1 r_{10}^2 [\cos X_0 + \cos Y_0] \quad (4.51)$$

$$\begin{aligned}0 &= -2\theta_1 - \theta_2 + \Omega_{12} - 2a_1 r_{20} \sin X_0 - \frac{b_1}{r_{20}} r_{10}^2 [\sin X_0 + \sin Y_0] \\ &\quad - \frac{2r_{40}}{r_{10}} \left[ \theta_{14} \cos \frac{(X_0 - Y_0)}{2} + \alpha_{14} \sin \frac{(X_0 - Y_0)}{2} \right]\end{aligned}\quad (4.52)$$

$$\begin{aligned}0 &= -2\theta_4 - \theta_2 + \Omega_{12} - 2a_1 r_{20} \sin Y_0 - \frac{b_1}{r_2} r_{10}^2 [\sin X_0 + \sin Y_0] \\ &\quad - \frac{2r_{10}}{r_{40}} \left[ \theta_{41} \cos \frac{(X_0 - Y_0)}{2} - \alpha_{41} \sin \frac{(X_0 - Y_0)}{2} \right]\end{aligned}\quad (4.53)$$

Spinning wave motion exists only when the phase difference should be  $\frac{(2n+1)\pi}{2}$ .

From Eqs. (4.49)-(4.53), only the condition  $r_{20} \rightarrow 0$  makes the system a spinning mode. When  $r_{20}$  approaches 0,

$$\xi_1 = \xi_4 + \frac{(2n+1)\pi}{2} \quad (n = 1, 2, 3 \dots) \quad (4.54)$$

Now check the condition for which the limit cycles exist. From Eqs. (4.49) and (4.50), the same condition as (4.34) in Section 4.2.1 is obtained.

$$\alpha_1 = (-1)^n \theta_{14} \quad (n = 1, 2, 3 \dots) \quad (4.55)$$

This is the necessary and sufficient condition for the existence of limit cycles. The remaining task is to determine the conditions for which the limit cycle is stable. However, the peculiar structure of the  $r_{20}$  equation does not make it possible to get the conditions for which the limit cycle is stable. Figure 4.2 shows the limit cycle of the 1T/1R modes, in which the pattern  $r_{20} \rightarrow 0$  can obviously be seen at the limit cycle.

Next, check this case from the energy conservation point of view. From Eqs. (4.42)-(4.44), the rate of energy change for the 1T/1R modes becomes

$$\begin{aligned} \frac{d}{dt} [\mathcal{E}_1 + \mathcal{E}_4 + \mathcal{E}_2] = & \alpha_1 (r_1^2 + r_4^2) - 2\theta_{14} r_1 r_4 \sin(\phi_1 - \phi_4) \\ & + \alpha_2 r_2^2 + b_1 r_2 (r_1^2 \cos X + r_4^2 \cos Y) \end{aligned} \quad (4.56)$$

It can easily be shown that the right hand side of Eq. (4.56) vanishes at the limit cycle by substituting condition (4.55). Therefore, the conclusion is reached that there is no contribution of the first radial mode to the spinning mode of oscillations after the limit cycle is attained for the combination of 1T/1R modes. That is, the contribution of the first radial mode is limited in the initial stages, but its effect disappears once the limit cycle is obtained, as can be clearly seen in Fig. 4.2.

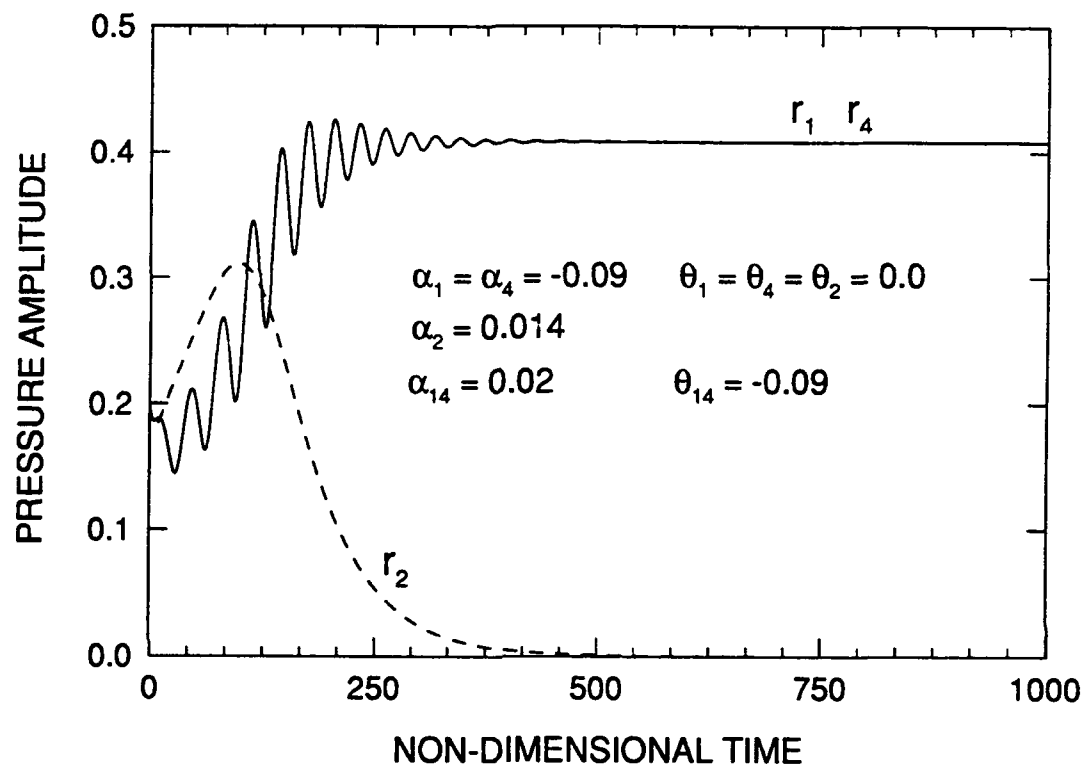


Figure 4.2 An Example Showing the Existence of Stable Limit Cycle, 1T/1R Modes

### 4.2.3 First Tangential/Second Tangential Modes

Mode shapes  $\psi_1$ ,  $\psi_4$ ,  $\psi_3$  and  $\psi_5$  are considered for the combination of the first and second tangential modes. The analysis of 1T/2T modes follows the same approach as that of the 1T/1R modes for the spinning mode of oscillations. The following relations for the linear parameters and linear coupling parameters are already found in Section 4.1.

$$\begin{aligned}\alpha_1 &= \alpha_4, \theta_1 = \theta_4 \\ \alpha_3 &= \alpha_5, \theta_3 = \theta_5\end{aligned}\tag{4.57a}$$

$$\begin{aligned}\alpha_{14} &= -\alpha_{41}, \theta_{14} = -\theta_{41} \\ \alpha_{35} &= -\alpha_{53}, \theta_{35} = -\theta_{53}\end{aligned}\tag{4.57b}$$

The approximate equations governing the amplitudes and phases of each mode are given by,

#### First Tangential Mode

$$\begin{aligned}\frac{dr_1}{dt} &= \alpha_1 r_1 + a_2 r_1 r_3 \cos X + a_2 r_4 r_5 \cos Z \\ &\quad + \alpha_{14} r_4 \cos(\phi_1 - \phi_4) - \theta_{14} r_4 \sin(\phi_1 - \phi_4)\end{aligned}\tag{4.58}$$

$$\begin{aligned}\frac{dr_4}{dt} &= \alpha_4 r_4 - a_2 r_3 r_4 \cos Y + a_2 r_1 r_5 \cos Z \\ &\quad + \alpha_{41} r_1 \cos(\phi_1 - \phi_4) + \theta_{41} r_1 \sin(\phi_1 - \phi_4)\end{aligned}\tag{4.59}$$

#### Second Tangential Mode

$$\frac{dr_3}{dt} = \alpha_3 r_3 + b_2 [r_1^2 \cos X - r_4^2 \cos Y]$$

$$+ \alpha_{35}r_5 \cos(\phi_3 - \phi_5) - \theta_{35}r_5 \sin(\phi_3 - \phi_5) \quad (4.60)$$

$$\begin{aligned} \frac{dr_5}{dt} &= \alpha_5r_5 + 2b_2r_1r_4 \cos Z \\ &+ \alpha_{53}r_3 \cos(\phi_3 - \phi_5) + \theta_{53}r_3 \sin(\phi_3 - \phi_5) \end{aligned} \quad (4.61)$$

and

$$\begin{aligned} \frac{dX}{dt} &= -2\theta_1 + \theta_3 + \Omega_{13} - \frac{1}{r_3} [2a_2r_3^2 + b_2r_1^2] \sin X + \frac{b_2r_4^2}{r_3} \sin Y \\ &- \frac{2a_2r_4r_5}{r_1} \sin Z - \frac{2r_4}{r_1} [\alpha_{14} \sin(\phi_1 - \phi_4) + \theta_{14} \cos(\phi_1 - \phi_4)] \\ &+ \frac{r_5}{r_3} [\alpha_{35} \sin(\phi_3 - \phi_5) + \theta_{35} \cos(\phi_3 - \phi_5)] \end{aligned} \quad (4.62)$$

$$\begin{aligned} \frac{dY}{dt} &= -2\theta_4 + \theta_3 + \Omega_{13} + \frac{1}{r_3} [2a_2r_3^2 + b_2r_4^2] \sin Y - \frac{b_2r_1^2}{r_3} \sin X \\ &- \frac{2a_2r_1r_5}{r_4} \sin Z + \frac{2r_1}{r_4} [\alpha_{41} \sin(\phi_1 - \phi_4) - \theta_{41} \cos(\phi_1 - \phi_4)] \\ &+ \frac{r_5}{r_3} [\alpha_{53} \sin(\phi_3 - \phi_5) + \theta_{53} \cos(\phi_3 - \phi_5)] \end{aligned} \quad (4.63)$$

$$\begin{aligned} \frac{dZ}{dt} &= -\theta_1 - \theta_4 + \theta_5 + \Omega_{13} - a_2r_3 [\sin X - \sin Y] \\ &- \left[ a_2 \left( \frac{r_4r_5}{r_1} + \frac{r_1r_5}{r_4} \right) + \frac{2b_2r_1r_4}{r_5} \right] \sin Z \\ &- \frac{r_4}{r_1} [\alpha_{14} \sin(\phi_1 - \phi_4) + \theta_{14} \cos(\phi_1 - \phi_4)] \\ &+ \frac{r_1}{r_4} [\alpha_{41} \sin(\phi_1 - \phi_4) - \theta_{41} \cos(\phi_1 - \phi_4)] \\ &- \frac{r_3}{r_5} [\alpha_{53} \sin(\phi_3 - \phi_5) - \theta_{53} \cos(\phi_3 - \phi_5)] \end{aligned} \quad (4.64)$$

where,

$$\begin{aligned}
 X &= 2\phi_1 - \phi_3 + \Omega_{13}t \\
 Y &= 2\phi_4 - \phi_3 + \Omega_{13}t \\
 Z &= \phi_1 + \phi_4 - \phi_5 + \Omega_{13}t \\
 \Omega_{13} &= 2\omega_1 - \omega_3 \\
 \phi_1 - \phi_4 &= (X - Y)/2 \\
 \phi_3 - \phi_5 &= Z - (X + Y)/2
 \end{aligned} \tag{4.65}$$

At the limit cycle, the same procedure as that in Section 4.2.2 is followed to find

$$\begin{aligned}
 \nu_1 &= \nu_4, \quad \nu_3 = \nu_5 \\
 X_0 &= 2\xi_1 - \xi_3 \\
 Y_0 &= 2\xi_4 - \xi_3 \\
 Z_0 &= \xi_1 + \xi_4 - \xi_5
 \end{aligned} \tag{4.66}$$

The Following assumption for the limit cycle is used, which is practical in a reasonable sense.

$$r_{10} = r_{40}, \quad r_{30} = r_{50} \tag{4.67}$$

Considerable manipulations of Eqs. (4.58)-(4.64) yield the following relationship.

$$X_0 = Y_0 + (2n + 1)\pi \quad (n = 1, 2, 3 \dots) \tag{4.68a}$$

$$Z_0 = \frac{(X_0 + Y_0)}{2} + \frac{(2k + 1)\pi}{2} \quad (k = 1, 2, 3 \dots) \tag{4.68b}$$

Then, the relations between frequency modulations are

$$\xi_1 = \xi_4 + \frac{(2n + 1)\pi}{2} \quad (n = 1, 2, 3 \dots) \tag{4.69a}$$

$$\xi_3 = \xi_5 + \frac{(2k + 1)\pi}{2} \quad (k = 1, 2, 3 \dots) \tag{4.69b}$$

This means that the phase differences between mode 1 and mode 4, and between mode 3 and mode 5 are  $\frac{\pi}{2}$  or  $\frac{3\pi}{2}$  at the limit cycle. On the other hand, acoustic pressure for the combination of the first and second tangential modes is

$$\begin{aligned}
 p'(\mathbf{r}, t)/\bar{p} &= r_{10} \sin(\omega_1 t + \phi_{10}) \cos \theta J_1(\kappa_1 r) \\
 &+ r_{40} \sin(\omega_1 t + \phi_{40}) \sin \theta J_1(\kappa_1 r) \\
 &+ r_{30} \sin(\omega_3 t + \phi_{30}) \cos 2\theta J_2(\kappa_3 r) \\
 &+ r_{50} \sin(\omega_3 t + \phi_{50}) \sin 2\theta J_2(\kappa_3 r)
 \end{aligned} \tag{4.70}$$

Eq. (4.70) can be further simplified using Eqs. (4.67) and (4.69) to give

$$\begin{aligned}
 p'(\mathbf{r}, t)/\bar{p} &= r_{10} \sin[(\omega_1 + \nu_1)t + \xi_1 + \theta] J_1(\kappa_1 r) \\
 &+ r_{30} \sin[(\omega_3 + \nu_3)t + \xi_3 + 2\theta] J_2(\kappa_3 r)
 \end{aligned} \tag{4.71}$$

Equation (4.71) shows that the spatial- and time-dependent parts of the first and second tangential modes are combined together, resulting in the spinning wave motion. Therefore, the combination of 1T/2T modes exhibits the spinning mode of oscillations within the chamber if the linear coupling, due to the combustion response, is taken into account. Some manipulations of the Eqs. (4.58)-(4.61) give the solution for the amplitude of each mode at the limit cycle.

$$r_{10}^2 = \frac{[\alpha_1 - (-1)^n \theta_{14}] [\alpha_3 - (-1)^k \theta_{35}]}{4a_2 b_2 \cos^2 X_0} \tag{4.72}$$

$$r_{30} = -\frac{\alpha_1 - (-1)^n \theta_{14}}{2a_2 \cos X_0} \tag{4.73}$$

According to the definitions of  $a_2$  and  $b_2$  in Eq. (4.47),  $a_2 b_2$  is negative; hence, for the real value of  $r_{10}$ , the following relation should be satisfied.

$$[\alpha_1 - (-1)^n \theta_{14}] [\alpha_3 - (-1)^k \theta_{35}] < 0 \quad (n, k = 1, 2, 3 \dots) \tag{4.74}$$

This is the necessary and sufficient condition for the existence of the limit cycle.

The next step is to determine the conditions for which the limit cycle is stable. Substituting the relations  $r_n = r_{n0} + r'_n$ ,  $X = X_0 + X'$ , etc. into the Eqs. (4.58)-(4.64) and neglecting higher-order terms, the system of the linearized equations is given by.

$$\begin{aligned} \frac{dr'_1}{dt} = & r'_1 \left[ \frac{\alpha_1 + (-1)^n \theta_{14}}{2} \right] + r'_4 \left[ \frac{-\alpha_1 + (-1)^n \theta_{14}}{2} \right] \\ & + r'_3 (a_2 r_{10} \cos X_0) + r'_5 (a_2 r_{10} \cos X_0) \\ & + X' \left[ -a_2 r_{10} r_{30} \sin X_0 + (-1)^{n+1} \frac{\alpha_{14} r_{10}}{2} \right] \\ & + Y' \left[ (-1)^n \frac{\alpha_{14} r_{10}}{2} \right] + Z' (-a_2 r_{10} r_{30} \sin X_0) \end{aligned} \quad (4.75)$$

$$\begin{aligned} \frac{dr'_4}{dt} = & r'_1 \left[ \frac{-\alpha_1 + (-1)^n \theta_{14}}{2} \right] + r'_4 \left[ \frac{\alpha_1 + (-1)^n \theta_{14}}{2} \right] \\ & + r'_3 (a_2 r_{10} \cos X_0) + r'_5 (a_2 r_{10} \cos X_0) \\ & + X' \left[ (-1)^n \frac{\alpha_{14} r_{10}}{2} \right] + Z' (-a_2 r_{10} r_{30} \sin X_0) \\ & + Y' \left[ -a_2 r_{10} r_{30} \sin X_0 + (-1)^{n+1} \frac{\alpha_{14} r_{10}}{2} \right] \end{aligned} \quad (4.76)$$

$$\begin{aligned} \frac{dr'_3}{dt} = & r'_1 (2b_2 r_{10} \cos X_0) + r'_4 (2b_2 r_{10} \cos X_0) + r'_3 (\alpha_3) r'_5 ((-1)^{k+1} \theta_{35}) \\ & + X' \left[ -b_2 r_{10}^2 \sin X_0 + (-1)^k \frac{\alpha_{35} r_{30}}{2} \right] \\ & + Y' \left[ -b_2 r_{10}^2 \sin X_0 + (-1)^k \frac{\alpha_{35} r_{30}}{2} \right] + Z' [(-1)^{n+1} \alpha_3 5 r_{30}] \end{aligned} \quad (4.77)$$

$$\frac{dr'_5}{dt} = r'_1 (2b_2 r_{10} \cos X_0) + r'_4 (2b_2 r_{10} \cos X_0) + r'_3 ((-1)^{k+1} \theta_{35}) + r'_5 (\alpha_3)$$

$$\begin{aligned}
& +X' \left[ (-1)^{k+1} \frac{\alpha_{35} r_{30}}{2} \right] + Y' \left[ +(-1)^{k+1} \frac{\alpha_{35} r_{30}}{2} \right] \\
& +Z' \left[ -2b_2 r_{10}^2 \sin X_0 + (-1)^k \alpha_3 5r_{30} \right]
\end{aligned} \tag{4.78}$$

and

$$\begin{aligned}
\frac{dX'}{dt} = & r'_1 \left[ \frac{2a_2 r_{30}}{r_{10}} \sin X_0 - \frac{2b_2 r_{10}}{r_{30}} \sin X_0 + (-1)^n \frac{2\alpha_{14}}{r_{10}} \right] \\
& +r'_4 \left[ \frac{-2a_2 r_{30}}{r_{10}} \sin X_0 - \frac{2b_2 r_{10}}{r_{30}} \sin X_0 - (-1)^n \frac{2\alpha_{14}}{r_{10}} \right] \\
& +r'_3 \left[ -2a_2 \sin X_0 + \frac{2b_2 r_{10}^2}{r_{30}^2} \sin X_0 - (-1)^k \frac{\alpha_{35}}{r_{30}} \right] \\
& +r'_5 \left[ -2a_2 \sin X_0 + +(-1)^k \frac{\alpha_{35}}{30} \right] \\
& +X' \left[ -2a_2 r_{30} \cos X_0 - \frac{b_2 r_{10}^2}{r_{30}} \cos X_0 + (-1)^n \theta_{14} + (-1)^k \frac{\theta_{35}}{2} \right] \\
& +Y' \left[ \frac{-b_2 r_{10}^2}{r_{30}} \cos X_0 - (-1)^n \theta_{14} + (-1)^k \frac{\theta_{35}}{2} \right] \\
& +Z' \left[ -2a_2 r_{30} \cos X_0 - (-1)^k \theta_{35} \right]
\end{aligned} \tag{4.79}$$

$$\begin{aligned}
\frac{dY'}{dt} = & r'_1 \left[ \frac{-2a_2 r_{30}}{r_{10}} \sin X_0 - \frac{2b_2 r_{10}}{r_{30}} \sin X_0 + (-1)^n \frac{2\alpha_{14}}{r_{10}} \right] \\
& +r'_4 \left[ \frac{2a_2 r_{30}}{r_{10}} \sin X_0 - \frac{2b_2 r_{10}}{r_{30}} \sin X_0 + (-1)^n \frac{2\alpha_{14}}{r_{10}} \right] \\
& +r'_3 \left[ -2a_2 \sin X_0 + \frac{2b_2 r_{10}^2}{r_{30}^2} \sin X_0 - (-1)^k \frac{\alpha_{35}}{r_{30}} \right] \\
& +r'_5 \left[ -2a_2 \sin X_0 + +(-1)^k \frac{\alpha_{35}}{30} \right] \\
& +X' \left[ \frac{-b_2 r_{10}^2}{r_{30}} \cos X_0 - (-1)^n \theta_{14} + (-1)^k \frac{\theta_{35}}{2} \right]
\end{aligned}$$

$$\begin{aligned}
& +Y' \left[ -2a_2 r_{30} \cos X_0 - \frac{b_2 r_{10}^2}{r_{30}} \cos X_0 + (-1)^n \theta_{14} + (-1)^k \frac{\theta_{35}}{2} \right] \\
& +Z' \left[ -2a_2 r_{30} \cos X_0 - (-1)^k \theta_{35} \right]
\end{aligned} \tag{4.80}$$

$$\begin{aligned}
\frac{dZ'}{dt} = & r'_1 \left[ -\frac{2b_2 r_{10}}{r_{30}} \sin X_0 \right] + r'_4 \left[ -\frac{2b_2 r_{10}}{r_{30}} \sin X_0 \right] \\
& + r'_3 \left[ -2a_2 \sin X_0 + (-1)^k \frac{\alpha_{35}}{30} \right] \\
& + r'_5 \left[ -2a_2 \sin X_0 + \frac{2b_2 r_{10}^2}{r_{30}^2} \sin X_0 - (-1)^k \frac{\alpha_{35}}{r_{30}} \right] \\
& + X' \left[ -a_2 r_{30} \cos X_0 - (-1)^k \frac{\theta_{35}}{2} \right] \\
& + Y' \left[ -a_2 r_{30} \cos X_0 - (-1)^k \frac{\theta_{35}}{2} \right] \\
& + Z' \left[ -2a_2 r_{30} \cos X_0 - \frac{2b_2 r_{10}^2}{r_{30}} \cos X_0 + (-1)^{k+1} \theta_{35} \right]
\end{aligned} \tag{4.81}$$

If these equations are expressed in matrix form, it gives a  $7 \times 7$  matrix which is impossible to handle analytically. For the analytical tractability, let us take the assumption that  $r'_1 = r'_4$  and  $r'_3 = r'_5$ , and  $X' = Y' = Z'$  which means the initial phase differences between mode 1 and mode 4, and between mode 3 and mode 5 are  $\frac{\pi}{2}$  or  $\frac{3\pi}{2}$ . The system is then reduced to a  $3 \times 3$  matrix that can be handled analytically; then, the characteristic equation for  $\lambda$  is given by,

$$\lambda^3 + P_1 \lambda^2 + P_2 \lambda + P_3 = 0 \tag{4.82}$$

where,

$$\begin{aligned}
P_1 &= -2(\alpha'_1 + \alpha'_3) \\
P_2 &= \alpha'_3 [\alpha'_3 - (4\alpha'_1 - \alpha'_3) \tan^2 X_0] \\
P_3 &= 2\alpha'_1 \alpha'_3 [(2\alpha'_1 + \alpha'_3)(1 + \tan^2 X_0)]
\end{aligned} \tag{4.83}$$

Application of Routh-Hurwitz stability analysis yields the following conditions for the stable limit cycles.

$$\begin{aligned} \alpha'_1 + \alpha'_3 &< 0 \\ 2\alpha'_1 + \alpha'_3 &< 0 \\ \alpha'_1 &> \frac{-|k|}{2 + \chi} \sqrt{\frac{-\chi^2 + 2\chi + 2}{\chi^2 + 2\chi + 2}} \quad \text{if } \alpha'_1 < 0 \end{aligned} \quad (4.84)$$

where,

$$\begin{aligned} \alpha'_1 &= \alpha_1 - (-1)^n \theta_{14} \\ \alpha'_3 &= \alpha_3 - (-1)^k \theta_{35} \\ \chi &= \frac{\alpha'_3}{\alpha'_1} \\ k &= 2(\theta_1 + (-1)^n \alpha_{14}) - (\theta_3 + (-1)^k \alpha_{35}) - (2\omega_1 - \omega_3) \end{aligned} \quad (4.85)$$

The linear coupling parameters are incorporated with the linear parameters. Figure 4.3 shows the overall result of Eq. (4.84) for the special case of  $k=0.025$ , where the shaded regions represent the conditions for the stable limit cycles.

Figure 4.4 shows the time history of the limiting amplitudes of 1T/2T modes with parameters which satisfy the conditions in Fig. 4.3. The stable limit cycles can be clearly seen.

#### 4.2.4 First Tangential/First Radial/Second Tangential Modes

Spinning oscillations of the combination of the first three modes are also investigated using the same analysis as that of the two-mode combination cases. The approximate equations governing the amplitudes and phases of each mode are as follows,

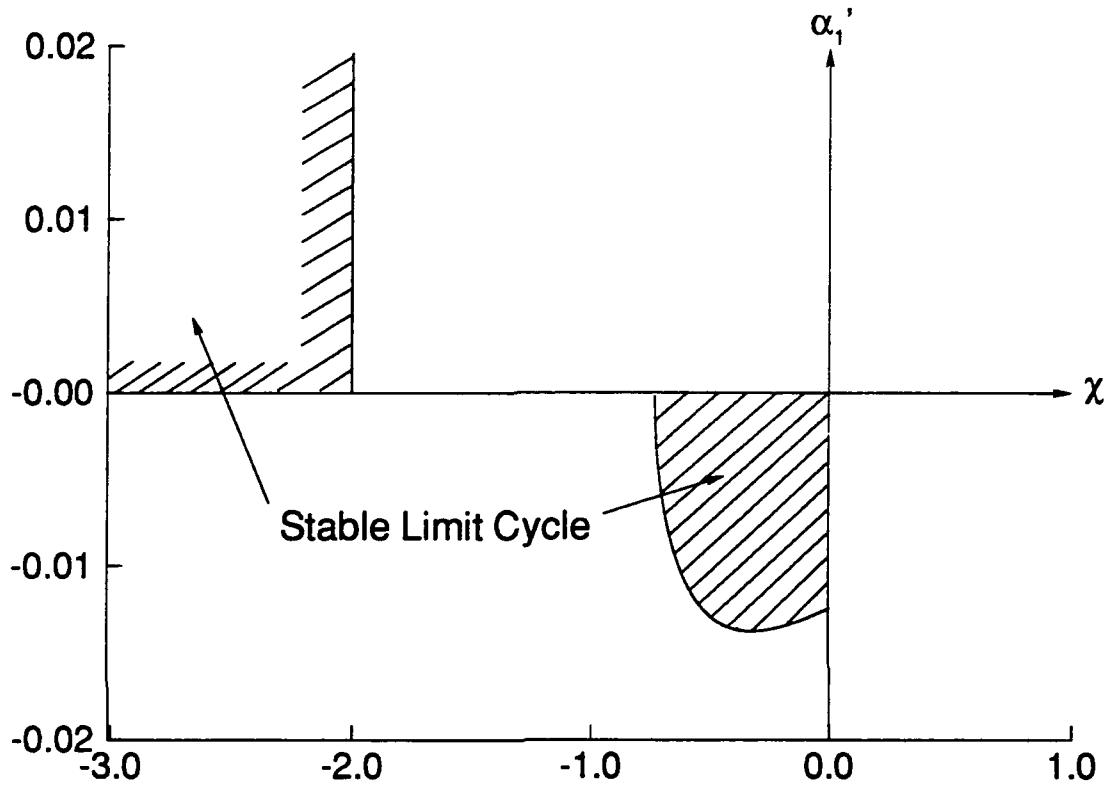


Figure 4.3 Illustration of the Necessary and Sufficient  
Conditions for the Stable Limit Cycle, 1T/2T Modes

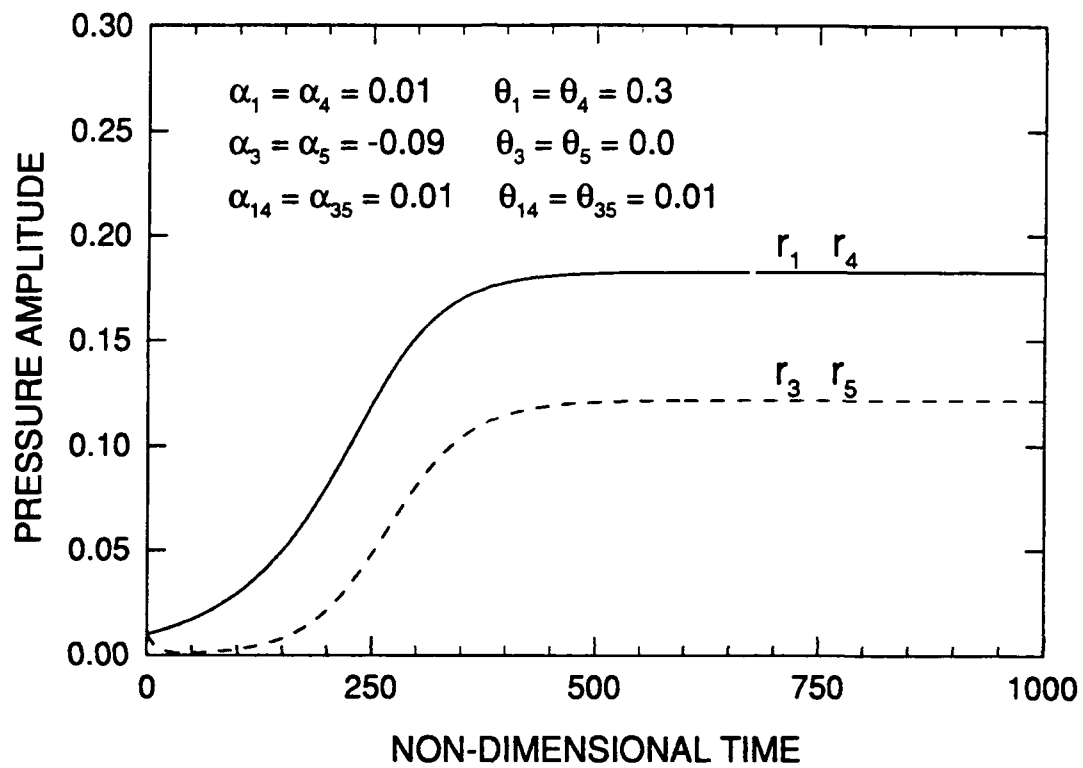


Figure 4.4 An Example Showing the Existence of Stable  
Limit Cycle, 1T/2T Modes

First Tangential Mode

$$\begin{aligned} \frac{dr_1}{dt} = & \alpha_1 r_1 + a_1 r_1 r_2 \cos X + a_2 r_1 r_3 \cos Y + a_2 r_4 r_5 \cos Z \\ & + \alpha_{14} r_4 \cos(\phi_1 - \phi_4) - \theta_{14} r_4 \sin(\phi_1 - \phi_4) \end{aligned} \quad (4.86)$$

$$\begin{aligned} \frac{dr_4}{dt} = & \alpha_4 r_4 + a_1 r_2 r_4 \cos X_1 - a_2 r_3 r_4 \cos Y_1 + a_2 r_1 r_5 \cos Z \\ & + \alpha_{41} r_1 \cos(\phi_1 - \phi_4) + \theta_{41} r_1 \sin(\phi_1 - \phi_4) \end{aligned} \quad (4.87)$$

$$\begin{aligned} r_1 \frac{d\phi_1}{dt} = & -\theta_1 r_1 - a_1 r_1 r_2 \sin X - a_2 r_1 r_3 \sin Y - a_2 r_4 r_5 \sin Z \\ & - \alpha_{14} r_4 \sin(\phi_1 - \phi_4) - \theta_{14} r_4 \cos(\phi_1 - \phi_4) \end{aligned} \quad (4.88)$$

$$\begin{aligned} r_4 \frac{d\phi_4}{dt} = & -\theta_4 r_4 - a_1 r_2 r_4 \sin X_1 + a_2 r_3 r_4 \sin Y_1 - a_2 r_1 r_5 \sin Z \\ & + \alpha_{41} r_1 \sin(\phi_1 - \phi_4) - \theta_{41} r_1 \cos(\phi_1 - \phi_4) \end{aligned} \quad (4.89)$$

First Radial Mode

$$\frac{dr_2}{dt} = \alpha_2 r_2 + b_1 [r_1^2 \cos X + r_4^2 \cos X_1] \quad (4.90)$$

$$r_2 \frac{d\phi_2}{dt} = -\theta_2 r_2 + b_1 [r_1^2 \sin X + r_4^2 \sin X_1] \quad (4.91)$$

Second Tangential Mode

$$\begin{aligned} \frac{dr_3}{dt} = & \alpha_3 r_3 + b_2 [r_1^2 \cos Y - r_4^2 \cos Y_1] \\ & + \alpha_{35} r_5 \cos(\phi_3 - \phi_5) - \theta_{35} r_5 \sin(\phi_3 - \phi_5) \end{aligned} \quad (4.92)$$

$$\begin{aligned} \frac{dr_5}{dt} = & \alpha_5 r_5 + 2b_2 r_1 r_4 \cos Z \\ & + \alpha_{53} r_3 \cos(\phi_3 - \phi_5) + \theta_{53} r_3 \sin(\phi_3 - \phi_5) \end{aligned} \quad (4.93)$$

$$\begin{aligned}
r_3 \frac{d\phi_3}{dt} = & -\theta_3 r_3 + b_2 [r_1^2 \sin Y - r_4^2 \sin Y_1] \\
& - \alpha_{35} r_5 \sin(\phi_3 - \phi_5) - \theta_{35} r_5 \cos(\phi_3 - \phi_5)
\end{aligned} \tag{4.94}$$

$$\begin{aligned}
r_5 \frac{d\phi_5}{dt} = & -\theta_5 r_5 + 2b_2 r_1 r_4 \sin Z \\
& + \alpha_{53} r_3 \cos(\phi_3 - \phi_5) - \theta_{53} r_3 \sin(\phi_3 - \phi_5)
\end{aligned} \tag{4.95}$$

where,

$$\begin{aligned}
X &= 2\phi_1 - \phi_2 + \Omega_{12}t \\
Y &= 2\phi_1 - \phi_3 + \Omega_{13}t \\
X_1 &= 2\phi_4 - \phi_2 + \Omega_{12}t \\
Y_1 &= 2\phi_4 - \phi_3 + \Omega_{13}t \\
Z &= \phi_1 + \phi_4 - \phi_5 + \Omega_{13}t
\end{aligned} \tag{4.96}$$

There are ten independent equations for ten unknowns, but the algebra is much more complicated than that for the two-mode combination cases. Direct numerical integration of Eqs. (4.86)-(4.95) is performed with various combinations of linear and linear coupling parameters. Similar to the result of the 1T/1R modes, the amplitude of the first radial mode  $r_{20}$  goes to zero for the spinning wave motions. Figure 4.5 shows the time history of the amplitudes for the 1T/1R/2T modes case, in which the pattern  $r_{20} \rightarrow 0$  can be clearly seen. Therefore, the first radial mode in the combination of the 1T/1R/2T modes has no contribution after the limit cycle is reached. But in the initial stages, it helps the system reach the limit cycle regardless of the initial phase differences and once the limit cycle is attained, its

effect disappears. The phase difference of the first tangential modes and that of the second tangential modes always become odd number multiples of  $\frac{\pi}{2}$ . That is, the system always degenerates to the spinning wave motion regardless of the initial phase differences.

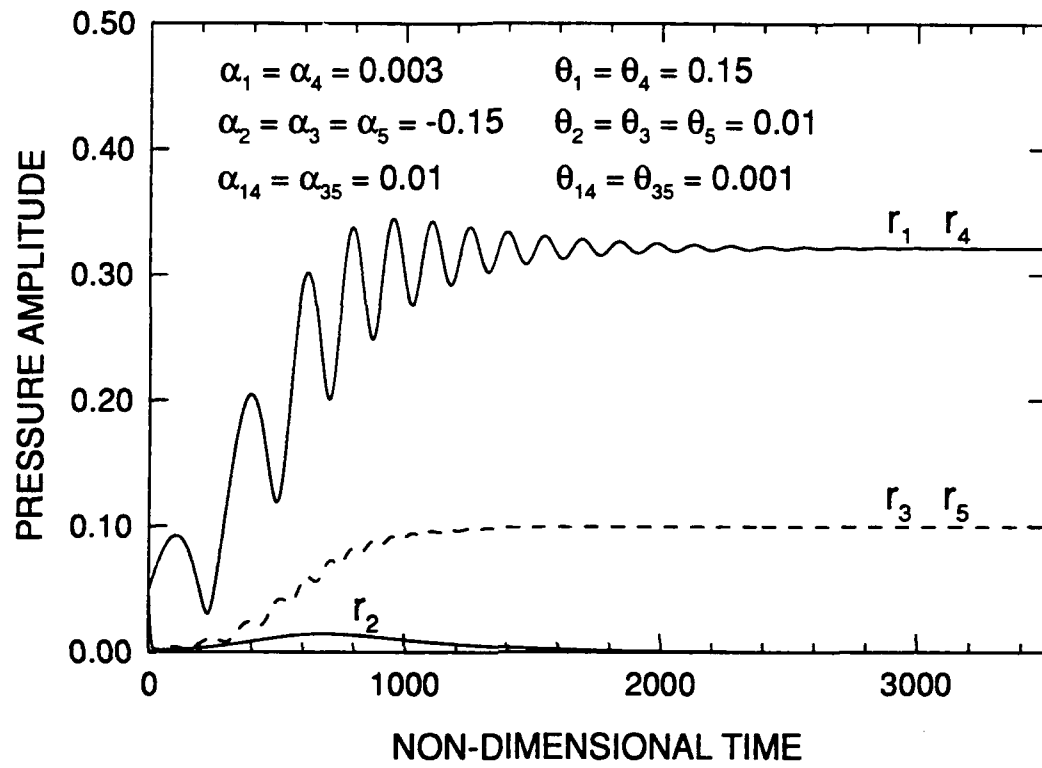


Figure 4.5 An Example Showing the Existence of Stable Limit Cycle, 1T/1R/2T Modes

## CHAPTER 5

### NONLINEAR ACOUSTIC WAVES IN BAFFLED CHAMBERS

This task represents an outgrowth of the linear acoustic analysis described in Chapter 3. A linear acoustic analysis provides a means for assessing whether a particular system is stable or unstable with respect to small perturbations, but gives no information about the ultimate amplitudes that unstable motions reach. In practical systems, constant amplitude oscillations (i.e. limit cycles) have often been observed. Since the occurrence of a limit cycle in a dynamical system requires the influence of nonlinear interactions, modeling of this phenomenon within a chamber requires appropriate consideration of the nonlinear terms in the governing equations. There have been many studies<sup>47,48,56</sup> addressing nonlinear analysis in the perfect (unbaffled) cylindrical chambers but none exists for the baffled combustors. This chapter deals with the nonlinear acoustic analysis in baffled environments.

#### 5.1 Nonlinear Acoustic Oscillations

The wave equation derived in Chapter 2 contains various nonlinear processes of concern. Among all nonlinear processes, the effect of second order nonlinear gas dynamics is examined systematically here.

Unlike the linear acoustic analysis, the simple assumption of time-harmonic behavior of all the acoustic variables is no longer valid. However, for a typical rocket engine, the mean-flow Mach number and the variation of mean pressure are small.

Under such conditions, the frequencies and the spatial variation of the unsteady motions deviate only slightly from the classical acoustic field obtained for the same geometry, but without any source terms ( $h = \mathbf{n} \cdot \mathbf{f} = 0$ ). Thus, the solution to the wave equation can be faithfully approximated by a synthesis of the linear normal acoustic modes  $\hat{p}_n(\mathbf{r})$ , with unknown time-varying amplitudes  $\eta_n(t)$  as coefficients:

$$p' = \bar{p} \sum_n \eta_n(t) \hat{p}_n(\mathbf{r}) \quad (5.1)$$

Correspondingly, the acoustic velocity field is written as

$$\mathbf{u}'_g(\mathbf{r}, t) = \sum_n \frac{\dot{\eta}_n(t)}{\bar{\gamma} k_n^2} \nabla \hat{p}_n(\mathbf{r}) \quad (5.2)$$

where the linear mode shape  $\hat{p}_n(\mathbf{r})$  satisfies the Helmholtz equation throughout the chamber, subject to rigid surface boundary conditions.

$$\nabla^2 \hat{p}_n + k_n^2 \hat{p}_n = 0 \quad (5.3a)$$

$$\mathbf{n} \cdot \nabla \hat{p}_n = 0 \quad (5.3b)$$

The time-varying amplitudes  $\eta_n(t)$  give the temporal nonlinear behavior of the system. Eqs. (5.1) and (5.2) are not exact representations of the true fields, for the boundary conditions are not satisfied; Eq. (5.1) gives  $\mathbf{n} \cdot \nabla p' = 0$  because the  $\hat{p}_n$  satisfies Eq. (5.3b) and according to Eq. (5.2), the velocity fluctuation vanishes on the boundary. This means that Eqs. (5.1) and (5.2) do not accurately reproduce the spatial structure of the unsteady motions near the boundary. Nevertheless, the errors are small when the perturbations contained in  $h$  and  $\mathbf{f}$  of Eqs. (2.30) and (2.32) are small. Furthermore, due to subsequent spatial averaging, the equations found for the amplitudes will provide a satisfactory basis for studying real problems.

Note that, owing to the geometric discontinuity set by the baffles, the linear mode shape  $\hat{p}_n$  is not the same as its counterpart for a perfect cylinder. Rather, it is expressed as a series of transverse normal modes.

$$\hat{p}_n(\mathbf{r}) = \sum_i \hat{\zeta}_{ni}(x) \psi_i(r, \theta) \quad (5.4)$$

Here,  $\psi_i(r, \theta)$  is the transverse normal mode function for a cylinder. The axial distribution function  $\hat{\zeta}_{ni}(x)$  can be determined using the eigenfunction-expansion technique discussed in Chapter 3. Thus, the nonlinear solution found in this chapter is constructed using the linear acoustic solutions found in Chapter 3.

A system of ordinary differential equations in terms of the time-varying amplitudes of Eq. (5.1) can be obtained. This is done by averaging the conservation equations over the volume of the chamber using a version of the method of least residuals, which is equivalent to Galerkin's method with the linear mode shape as a weighting function. Now multiply Eq. (2.29) by  $\hat{p}_n$  and Eq. (5.3a) by  $p'$ , subtract the results, integrate over the entire volume, and apply Green's theorem to get

$$\iiint \left( \frac{\hat{p}_n}{\bar{a}^2} \frac{\partial^2 p'}{\partial t^2} + k_n^2 \hat{p}_n p' \right) dV = - \iiint \hat{p}_n h dV - \oint \hat{p}_n \mathbf{f} \cdot \mathbf{n} dS \quad (5.5)$$

Substitution of Eqs. (5.1) and (5.4) into Eq. (5.5) and some rearrangement of the result leads to a system of second-order ordinary differential equations for the temporal behavior of nonlinear oscillations.

$$\sum_m C_{nm} (\ddot{\eta}_m + \omega_n^2 \eta_m) = F_n \quad (5.6)$$

where the amplitude coefficients,  $C_{nm}$ , and forcing function,  $F_n$ , are defined as,

$$C_{nm} = \sum_i E_i^2 \int \hat{\zeta}_{ni}(x) \hat{\zeta}_{mi}(x) dx \quad (5.7)$$

$$F_n = -\frac{\bar{a}^2}{\bar{p}} \left[ \iiint \hat{p}_n h dV + \oiint \hat{p}_n \mathbf{f} \cdot \mathbf{n} dS \right] \quad (5.8)$$

where

$$E_i^2 = \iint \psi_i^2(r, \theta) r dr d\theta \quad (5.9)$$

Equation (5.6) represents the time-dependent motions of a collection of nonlinear oscillators, one oscillator being associated with each linear mode. The principal difference between the present analysis and the unbaffled cases<sup>47,48</sup> lies in the structure of the ordinary differential equation (5.6), in which strong coupling among modes occurs on both sides of the equation. Now, the problem is reduced to solving this system of second-order ordinary differential equations for the time-varying amplitude, given a specified initial condition.

The forcing function,  $F_n$  represents the deviation from unperturbed acoustic modes and, therefore, provides the mechanism that allows for initial finite oscillations to grow or decay. As a result, the various components of  $F_n$  are essential to the study of combustion instabilities in the baffled combustion chambers. It is convenient to classify these components of  $F_n$  according to the orders of  $p'$  and  $\mathbf{u}'_g$  in each term. Substitution of Eqs. (2.30) and (2.32) into Eq. (5.8) yields the explicit expression of the forcing function  $F_n$ . After some straightforward manipulations,  $F_n$  can be written as

$$F_n = -\frac{\bar{a}^2}{\bar{p}} \left[ \underbrace{\bar{\rho} k_n^2 \iiint \hat{p}_n (\bar{\mathbf{u}}_g \cdot \mathbf{u}'_g) dV}_{[a]} - \underbrace{\bar{\rho} \iiint [\mathbf{u}'_g \times (\nabla \times \bar{\mathbf{u}}_g)] \cdot \nabla \hat{p}_n dV}_{[b]} \right. \\ \left. - \underbrace{\frac{1}{\bar{a}^2} \iiint \frac{\partial p'}{\partial t} \bar{\mathbf{u}}_g \cdot \nabla \hat{p}_n dV}_{[c]} + \underbrace{\frac{\bar{\gamma} - 1}{\bar{a}^2} \iiint \hat{p}_n \frac{\partial p'}{\partial t} \nabla \cdot \bar{\mathbf{u}}_g dV}_{[d]} \right]$$

$$\begin{aligned}
& \underbrace{+\bar{\rho} \iiint (\mathbf{u}_g' \cdot \nabla \mathbf{u}_g') \cdot \nabla \hat{p}_n dV}_{[e]} \quad \underbrace{-\frac{1}{\bar{a}^2} \iiint \frac{\partial p'}{\partial t} \mathbf{u}_g' \cdot \nabla \hat{p}_n dV}_{[f]} \\
& \underbrace{+\frac{\bar{\gamma}-1}{\bar{a}^2} \iiint \hat{p}_n \frac{\partial p'}{\partial t} \nabla \cdot \mathbf{u}_g' dV}_{[g]} \quad \underbrace{+\frac{\bar{\gamma}-1}{\bar{a}^2} \iiint \hat{p}_n p' \nabla \cdot \frac{\partial \mathbf{u}_g'}{\partial t} dV}_{[h]} \quad (5.10) \\
& \underbrace{+\oint \hat{p}_n \frac{\partial}{\partial t} (\bar{\mathbf{u}}_g \rho' + \mathbf{u}_g' \bar{\rho} + \mathbf{u}_g' \rho') \cdot \mathbf{n} dS}_{[i]} \\
& \underbrace{- \iiint (\mathcal{F}' \cdot \nabla \hat{p}_n) + \left( \frac{1}{\bar{a}^2} \hat{p}_n \frac{\partial \mathcal{P}'}{\partial t} \right) dV}_{[j]}
\end{aligned}$$

The first four terms, [a] – [d], are referred to as the linear acoustics, and the next four terms, [e] – [h], the second order nonlinear acoustics. The last two terms, [i] – [j], are related to the combustion response and other sources such as particle damping. If only the nonlinear contribution from the gasdynamics of the unsteady flow is taken into account in this study, the forcing function can be expressed in terms of the wave amplitude  $\eta_n$ , with the form

$$F_n = - \sum_{i=1}^{\infty} [D_{ni} \dot{\eta}_i + E_{ni} \eta_i] - \sum_{i=1}^{\infty} \sum_{j=1}^{\infty} [A_{nij} \dot{\eta}_i \dot{\eta}_j + B_{nij} \eta_i \eta_j] \quad (5.11)$$

Note that the cross coupling term  $\dot{\eta}_i \eta_j$  does not appear in the formulation of Eq. (5.11) since nonlinear combustion responses and the interactions between mean flow and nonlinear acoustics are not included in this analysis. The explicit forms of the above coefficients are given by,

$$D_{ni} = \iiint \left[ \left( 1 + \frac{k_n^2}{k_i^2} \right) \hat{p}_n \bar{\mathbf{u}}_g \cdot \nabla \hat{p}_i - \frac{1}{k_i^2} (\nabla \hat{p}_i \times (\nabla \times \bar{\mathbf{u}}_g)) \cdot \nabla \hat{p}_n \right]$$

$$+ \bar{\gamma} \hat{p}_n \hat{p}_i \nabla \cdot \bar{\mathbf{u}}_g \Big] dV \quad (5.12a)$$

$$E_{ni} = -\bar{a}^2 \oint \hat{p}_n \nabla \hat{p}_i \cdot \mathbf{n} dS \quad (5.12b)$$

and

$$A_{nij} = \frac{I_{nij}}{8\bar{\gamma}k_i^2k_j^2} \left[ (k_i^2 + k_j^2)(2k_i^2 + 2k_j^2 - k_n^2) - k_n^4 - 8\bar{\gamma}k_i^2k_j^2 \right] \quad (5.12c)$$

$$B_{nij} = \frac{\bar{a}^2 I_{nij}}{4\bar{\gamma}} \left[ 2(k_i^2 + k_j^2)(1 - \bar{\gamma}) - k_n^2 \right] \quad (5.12d)$$

$$I_{nij} = \iiint \hat{p}_n \hat{p}_i \hat{p}_j dV. \quad (5.12e)$$

The linear coefficients  $D_{ni}$  and  $E_{ni}$  arise from all linear processes in Eq. (5.10), and the nonlinear coefficients  $A_{nij}$  and  $B_{nij}$  represent the second order nonlinear acoustics part of Eq. (5.10). Note that all coefficients depend on the linear mode shapes and frequencies of the chamber.

After the forcing function  $F_n$ , Eq. (5.11) is substituted in Eq. (5.6), this can be rewritten in a matrix form:

$$[\mathbf{C}] \{ \ddot{\eta} \} = \{ f \} \quad (5.13)$$

where

$$[\mathbf{C}] \{ \ddot{\eta} \} = \sum_{m=1}^{\infty} C_{nm} \ddot{\eta}_m \quad (5.14a)$$

$$\begin{aligned} \{ f \} = & - \sum_{i=1}^{\infty} \left[ D_{ni} \dot{\eta}_i + (E_{ni} + C_{ni} \omega_n^2) \eta_i \right] \\ & - \sum_{i=1}^{\infty} \sum_{j=1}^{\infty} \left[ A_{nij} \dot{\eta}_i \dot{\eta}_j + B_{nij} \eta_i \eta_j \right] \end{aligned} \quad (5.14b)$$

Now the problem is reduced to solving a set of simultaneous differential equations (5.13). But unlike the unbaffled case, the wave motion can no longer be viewed as a weakly coupled system. Consequently, the method of time-averaging used by Culick,<sup>46</sup> which can replace a system of second-order ordinary differential equations by an equivalent system of first-order equations, cannot be practically applied to solving Eq. (5.13) due to this strong coupling among modes. Therefore, numerical integration of Eq. (5.13) is performed using a fourth-order Runge-Kutta scheme to get the time history of the amplitudes  $\eta_n(t)$ . However, a similar format as used in the method of time averaging is employed for the representation of the amplitude of the limit cycle. Namely, the time-varying amplitudes,  $\eta_n(t)$  are transformed to two variables,  $r_n(t)$  and  $\phi_n(t)$  as follows,

$$\eta_n(t) = r_n(t) \sin[\omega_n t + \phi_n(t)] \quad (5.15)$$

where  $r_n(t)$  and  $\phi_n(t)$  are the amplitude and phase of the limit cycle, respectively. Then the amplitude of the limit cycle,  $r_n(t)$ , takes the form,

$$r_n(t) = \sqrt{[\eta_n(t)]^2 + \left[ \frac{\dot{\eta}_n(t)}{\omega_n} \right]^2} \quad (5.16)$$

This expression is used to represent the temporal variation of the amplitude of the limit cycle. The major task at this point is to determine the limiting amplitude  $r_n(t)$  characterizing the nonlinear oscillations.

For the two-dimensional rectangular baffled chamber, the results from the two-dimensional linear acoustic analysis are used to determine the coefficients  $C_{nm}$  characterizing the baffled system. In calculating the coefficients  $C_{nm}$ , the

assumption of no mean flow is made to allow concentration upon the nonlinear behavior itself. The calculation is performed in two regions separately (i.e. baffle compartments and the main chamber) and then combined to give the final expression for the coefficients. That is,

$$\begin{aligned} C_{nm} &= \sum_i \left[ E_i^2 \int \hat{\zeta}_{ni} \hat{\zeta}_{mi} dx \right] \\ &= \sum_i \left[ E_i^2 \int_0^{L_b} \hat{\zeta}_{ni} \hat{\zeta}_{mi} dx \right]_B + \sum_i \left[ E_i^2 \int_{L_b}^L \hat{\zeta}_{ni} \hat{\zeta}_{mi} dx \right]_C \end{aligned} \quad (5.17a)$$

where

$$E_i^2 = \int \psi_i^2(y) dy \quad (5.17b)$$

Here, the  $B$  and  $C$  subscripts denote integration in the baffle compartments and the main chamber regions, respectively.

The calculation of  $I_{nij}$  in Eq. (5.12e) is also treated separately,

$$\begin{aligned} I_{nij} &= \iiint \hat{p}_n \hat{p}_i \hat{p}_j dV \\ &= \sum_a \sum_b \sum_c \left[ \int_0^{L_b} \hat{\zeta}_{na} \hat{\zeta}_{ib} \hat{\zeta}_{jc} dx \cdot \int_B \psi_a \psi_b \psi_c dy \right. \\ &\quad \left. + \int_{L_b}^L \hat{\zeta}_{na} \hat{\zeta}_{ib} \hat{\zeta}_{jc} dx \cdot \int_C \psi_a \psi_b \psi_c dy \right] \end{aligned} \quad (5.18)$$

Equation (5.18) is used to calculate nonlinear parameters  $A_{nij}$  and  $B_{nij}$  from (5.12c) and (5.12d), respectively.

For the three-dimensional cylindrical baffled chamber, the same procedure as the two-dimensional chamber case is followed. Then, the coefficients  $C_{nm}$  are

determined as

$$\begin{aligned} C_{nm} &= \sum_i \left[ E_i^2 \int \hat{\zeta}_{ni} \hat{\zeta}_{mi} dx \right] \\ &= \sum_i \left[ E_i^2 \int_0^{L_b} \hat{\zeta}_{ni} \hat{\zeta}_{mi} dx \right]_B + \sum_i \left[ E_i^2 \int_{L_b}^L \hat{\zeta}_{ni} \hat{\zeta}_{mi} dx \right]_C \end{aligned} \quad (5.19a)$$

where

$$E_i^2 = \iint \psi_i^2(r, \theta) r dr d\theta \quad (5.19b)$$

For the determination of nonlinear parameters  $A_{nij}$  and  $B_{nij}$ , the coefficient  $I_{nij}$  in Eq. (5.12e) is calculated first as

$$\begin{aligned} I_{nij} &= \iiint \hat{p}_n \hat{p}_i \hat{p}_j dV \\ &= \sum_a \sum_b \sum_c \left[ \int_0^{L_b} \hat{\zeta}_{na} \hat{\zeta}_{ib} \hat{\zeta}_{jc} dx \cdot \iint_B \psi_a \psi_b \psi_c r dr d\theta \right. \\ &\quad \left. + \int_{L_b}^L \hat{\zeta}_{na} \hat{\zeta}_{ib} \hat{\zeta}_{jc} dx \cdot \iint_C \psi_a \psi_b \psi_c r dr d\theta \right] \end{aligned} \quad (5.20)$$

## 5.2 Results and Discussion of Nonlinear Acoustic Analysis

From the energy point of view, linear oscillations can be visualized as having completely uncoupled modes of energy storage in the oscillating fields. However, it is highly unlikely that a real system, certainly a system as complicated as a liquid rocket engine, will be completely linear with all modes uncoupled. If the different modes are coupled with each other, it is quite possible that draining energy from one mode will also drain energy from other modes through the nonlinear processes.

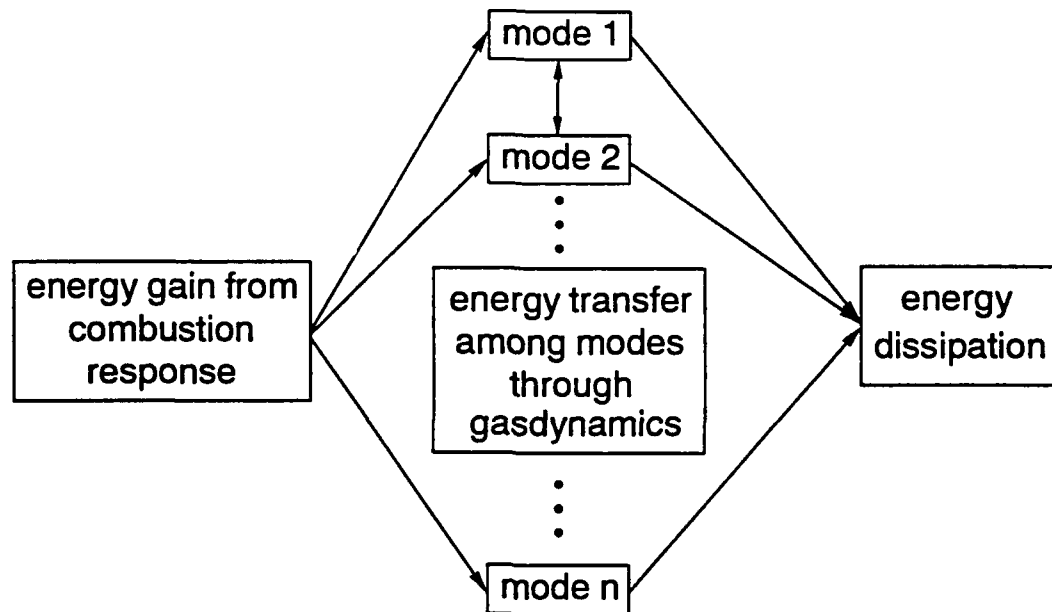


Figure 5.1 Block Diagram Showing the Energy Transfer Relation among Modes

Therefore, given the circumstances that instabilities are likely, it is necessary to pay attention to nonlinear behavior. The overall energy transfer relationship among modes through nonlinear interactions, and how this is related with linear processes, are conveniently outlined in the block diagram in Fig. 5.1.

Useful analytical results from the nonlinear analysis described in the previous section can fully describe the time-varying amplitudes in finite oscillations for a baffled chamber. The complexity of the problem depends on how many nonlinear

modes are to be considered in the analysis. Unfortunately, but as is expected, the analysis becomes more and more complicated as the number of modes considered in the nonlinear synthesis is increased. Because of the complexity of the actual analysis, only the case of the first two modes combination (i.e.  $n = 1$  and  $n = 2$ ) is treated for the two-dimensional analysis. This case represents the simplest possible situation and can serve as a basis for analyzing more complicated problems. Culick and Yang<sup>9</sup> showed that the two mode expansion is valid over a broad range of linear and nonlinear parameters that govern the global quantitative behavior for un baffled chambers. Although higher modes have the capability to modify the stability domain, the amplitudes of higher modes for many practical systems are negligibly small due to the efficient viscous damping at high frequencies. Thus, the description of nonlinear acoustic fields in the baffled chambers by the first two modes may be justified.

The coefficients  $C_{nm}$ , which represent the major distinction between the baffled and the un baffled chamber nonlinear analysis, are functions of both baffle length and chamber oscillation frequency. Although the combinations using only the first two nonlinear modes are under examination ( $n = 1$  and  $n = 2$ ), the number of simultaneous equations to be solved increases by a factor of  $2m$ , where  $m$  is the number of linear modes considered in one nonlinear mode. However,  $m$  should take on as many values as possible. This makes the analysis complicated to a great extent, since even a few modes in the expansion mean a large set of equations to be solved. For this analysis, the chamber with baffle length  $L_b = 0.2H$  is used and the frequencies obtained from the linear acoustic analysis are employed to estimate

these coefficients from Eqs. (5.17) and (5.19) for the two-dimensional and three-dimensional chambers, respectively. Values of  $C_{nm}$  are tabulated for the first three modes in Table 2 and Table 3 for two-dimensional and three-dimensional cases, respectively.

Table 2 Values of  $C_{nm}$  for Two-Dimensional Chamber

$C_{nm}$	$m = 1$	$m = 2$	$m = 3$
$n = 1$	0.386	0.0	0.204
$n = 2$	0.0	0.363	0.0
$n = 3$	0.204	0.0	0.286

Table 3 Values of  $C_{nm}$  for Three-Dimensional Chamber

$C_{nm}$	$m = 1$	$m = 2$	$m = 3$
$n = 1$	0.72	0.78	-0.13
$n = 2$	0.78	1.43	0.0
$n = 3$	-0.13	0.0	0.37

Using these coefficients, the direct numerical integration of Eq. (5.13) for the first two modes is performed for the investigation of limit cycle behavior in a system.

A limit cycle behavior is found to exist even though there is complicated coupling among modes in the baffled system. The result for two-dimensional rectangular chamber is shown in Fig. 5.2, for the first two transverse modes

combination; note that the radian frequency of each mode is normalized with respect to the fundamental mode of an un baffled chamber. For a system with a positive growth constant of the first mode, the stability of the system can be improved if the growth constant of the second mode is negative. Although this condition corresponds to a decrease of the limit cycle amplitude of the second mode, it may result in an amplitude increase of the first mode, since a higher first mode amplitude would be required to balance the stronger damping effect of the second mode and thus produce the stable limit cycle. It is interesting to mention that the amplitude histories of limit cycles observed in this study have different shapes from those for un baffled chambers. The limit cycle amplitudes are fluctuating with respect to constant values, possibly due to the strong coupling between modes.

From energy considerations, a mode with a positive growth constant can be directly interpreted as unstable if there is no nonlinear coupling. Therefore, such a mode can serve as an effective source of energy for the nonlinear acoustic system. In a similar manner, a mode with a negative growth constant can be regarded as a sink of energy. The nonlinear coupling allows for inter-modal energy exchange and can thus channel net energy from the unstable to the stable modes. When the limit cycle is reached, the sink and source effects of the individual mode balance each other and the energy of the system remains constant in time. For the two-mode combination considered here, energy is supplied through the first mode by linear processes because its growth constant is positive. This energy is then transferred to the second mode through the second order nonlinear gasdynamics coupling, where

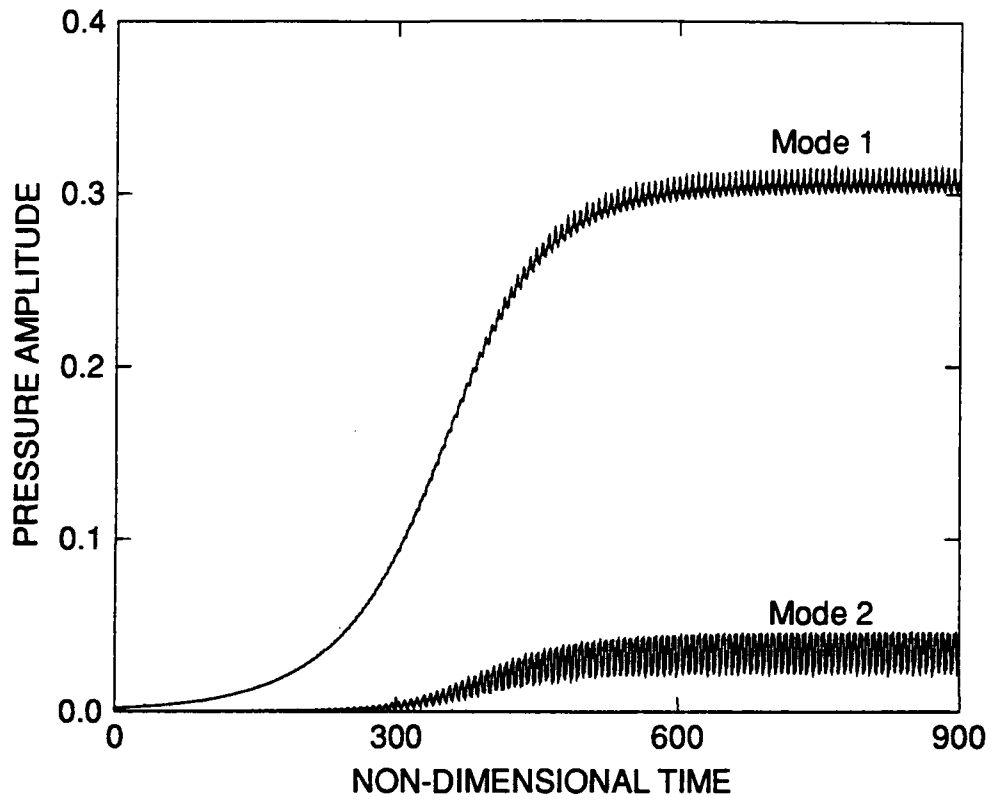


Figure 5.2 An Example Showing the Existence of Limit Cycle  
for Two-Dimensional Chamber;  
the First and Second Transverse Modes

it is dissipated by a linear decay process acting on the second mode with its negative growth constant. In general, nonlinear processes associated with gasdynamics have a natural tendency to cause energy flow from lower to higher modes.

For a three-dimensional cylindrical baffled combustion chamber, only three cases of nonlinear mode combinations are treated here. Investigated are: (1) the first tangential and the first radial modes, (2) the first tangential and the second tangential modes and (3) the first tangential, the first radial and the second tangential modes. These three situations represent the most commonly observed modes in actual rocket engines, without presenting a formidable calculational task.

Limit cycles are reached for all cases and the results are shown in Fig. 5.3-5.5 for 1T/1R mode, 1T/2T mode and 1T/1R/2T mode combinations, respectively. For all three cases, the limiting amplitudes fluctuate in a manner similar to the results for the two-dimensional baffled chamber, due to the complicated coupling among modes. This fluctuation can be equivalently stated as a vertical shift of the envelope of the time-varying amplitude as seen in Fig. 5.6, thus making the limit cycle fluctuate with respect to constant value.

The overall trends are the same as the two-dimensional case, but it is interesting to observe that the intensity of the fluctuation for the three-dimensional case is stronger. The fluctuation is more than 30 percent of the average amplitude for all three-dimensional cases. This means a larger shifting of the envelopes of the time-varying amplitudes. Coupling among modes allows a cascade of energy from lower modes to higher modes, as evidenced by the limit cycle growth for the first tangential mode. Figure 5.5 shows that the amplitude of the first radial mode is

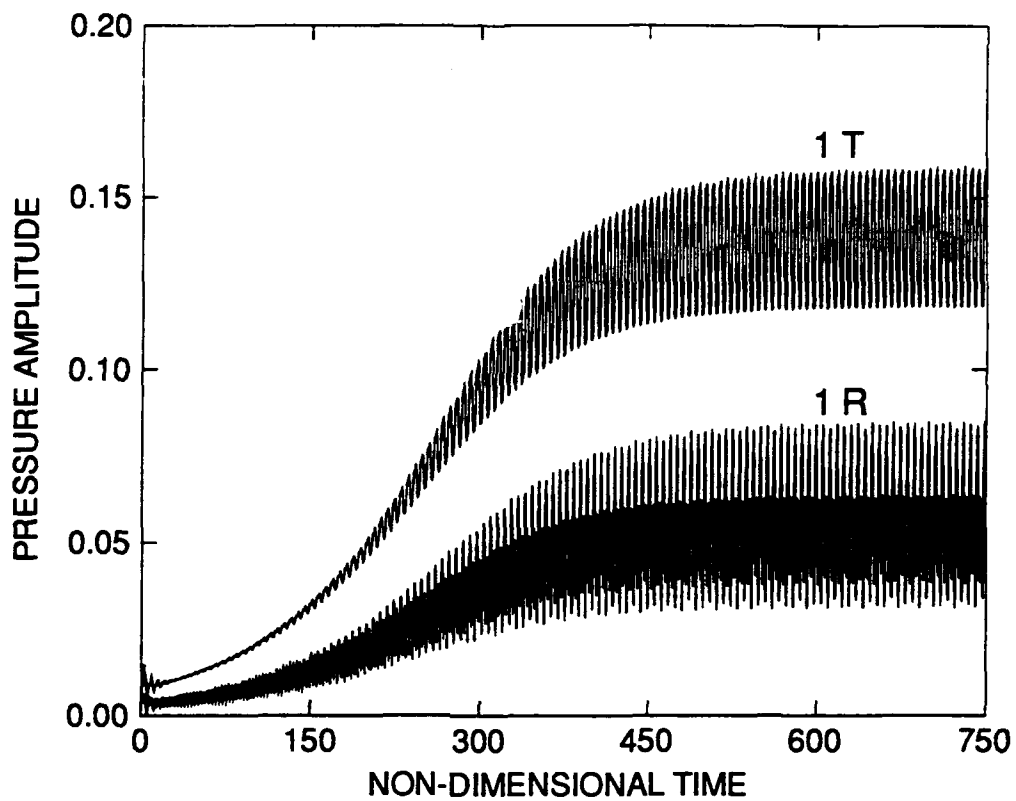


Figure 5.3 An Example Showing the Existence of Limit Cycle  
for Three-Dimensional Chamber;  
the First Tangential/First Radial Modes

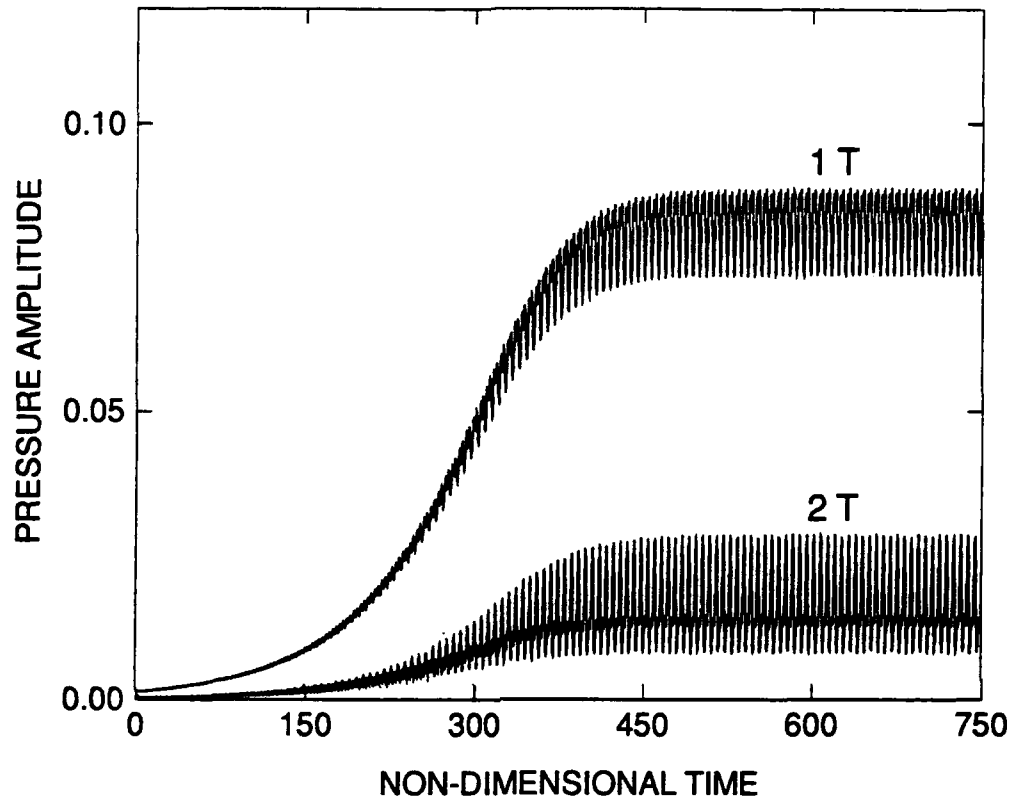


Figure 5.4 An Example Showing the Existence of Limit Cycle  
for Three-Dimensional Chamber;  
the First Tangential/Second Tangential Modes

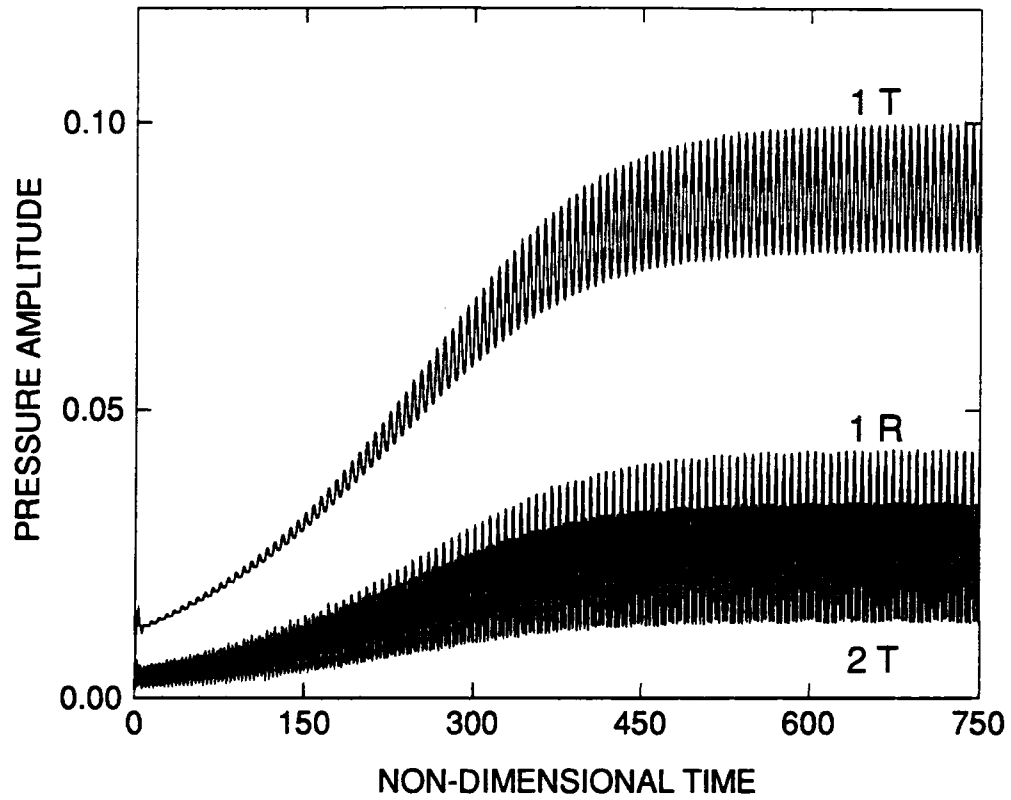


Figure 5.5 An Example Showing the Existence of Limit Cycle for Three-Dimensional Chamber; the First Tangential/Second Tangential/First Radial Modes

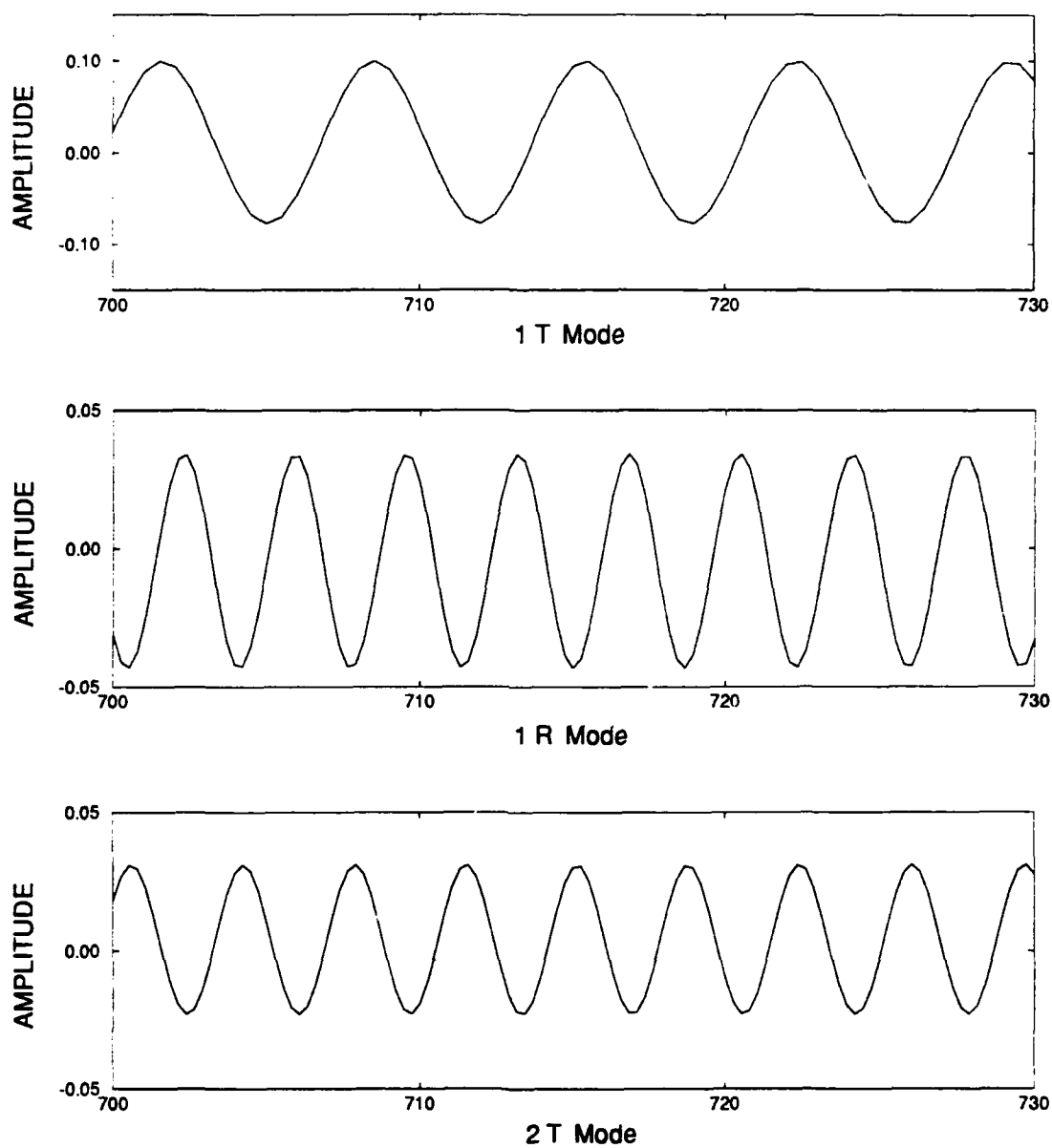


Figure 5.6 Time History of the Pressure Amplitude  
for Three-Dimensional Chamber; the First  
Tangential/Second Tangential/First Radial Modes

similar to that of the second tangential mode. Thus, both the first tangential and the first radial modes are important in dissipating the energy of the first tangential mode for the creation of a stable limit cycle in this scenario.

In summary, the typical nonlinear behaviors—limit cycles are observed in combustion chambers even though there are strong couplings among modes in baffled environments. And energy cascade through the nonlinear gasdynamics processes is also predicted for several mode combinations. But unlike the unbaffled case, the limit cycle amplitudes show the fluctuating characteristics due to the complicated inter-modal coupling in the baffled system.

## CHAPTER 6

## CONCLUSIONS AND FUTURE WORK

Linear and nonlinear acoustic wave analyses have been developed for two- and three-dimensional baffled combustion chambers. A wave equation governing flow oscillations is derived from the conservation equations for a two-phase mixture. To solve this wave equation in baffled environments, the eigenfunction expansion technique is used to express solutions in the baffle compartments and the main chamber, separately. With appropriate matching of the acoustic fields at the interface between the baffle compartments and the main chamber, unsteady flow structures in the entire chamber can be obtained. The major advantage of this approach is that it alleviates the computational burden associated with conventional numerical methods, and provides more sweeping results in a much more efficient manner. Furthermore, it provides an analytical framework for studying mechanisms proposed as the causes of unsteady motions in baffled rocket engines.

From the linear acoustic analysis, the detailed wave structures inside the baffled combustion chambers, including distributions of acoustic pressure and velocity, have been investigated. Three stabilizing effects of the baffle on transverse modes of instability have been observed. First, transverse waves can be longitudinalized inside baffle compartments. This effect is more conspicuous for chambers with longer baffle lengths. Longitudinal waves are rarely a problem in most liquid rocket engines, so the longitudinalization of the waves seems to be a sensible

way for causing stability. Physically, this longitudinalization may act to decouple combustion from oscillatory effects if the processes near the injector face are sensitive to transverse variations in pressure. However, there is also a potentially destabilizing concentration of pressure amplitude near the injector face associated with longitudinalization of the wave. Second, a severe restriction of the transverse component of the acoustic velocity fluctuation is observed. If processes sensitive to acoustic velocity are responsible for instability, this restriction could be the key in stabilizing the system. Third, the normal mode frequency is decreased with the addition of baffles. Acoustic pressure oscillations that might have induced instability without the baffles might fail to interact constructively due to the shift of frequency.

From the nonlinear spinning mode analysis in a cylindrical unbaffled chamber, linear couplings between modes are found to exist and to play an important role on the spinning transverse mode of oscillations. Limit cycle histories are also calculated and presented. Nonlinear acoustic solutions for baffled combustion chambers are found by using a series of linear modes, with time-dependent amplitudes as coefficients to express the nonlinear behavior. A system of second-order ordinary differential equations in terms of the time-varying amplitudes is solved to yield information regarding nonlinear phenomenon such as limit cycles, whose behaviors are observed for several mode combinations. Unlike the unbaffled chamber, however, the envelope of the time-varying amplitude is shifted, causing fluctuations of the limit cycle due to the strong inter-modal coupling in the baffled system.

While this research offers investigation of the detailed wave structures, and

some nonlinear behaviors within the baffled combustion chambers, some aspects require further attention in future research. First of all, the mean flow Mach number is considered to be constant throughout the chamber since concentrated combustion is assumed in this analysis. Consideration of distributed combustion may provide a more accurate and realistic solution for this problem. Second, the study of vortical structures by Wicker<sup>32</sup> shows that considerable amounts of vorticity can be generated by the acoustic wave from the baffle blade. Viscous energy dissipation and kinetic energy convection by these vortices are plausible explanations of the other stabilizing effects of baffles and are worthy of continued pursuit. Third, flow turning effects may be important in the baffled chamber analysis, since this is a mechanism of acoustic energy loss due to the turning of flow by the acoustic wave. Placing baffle blades inside the chamber can change the direction of the flow to generate energy loss in a chamber. Fourth, present nonlinear analysis considers only the second-order nonlinear gasdynamics terms in the formulation. An extension to the higher-order terms may be able to handle more realistic situations. The further consideration of these four points can aid in the construction of a more realistic and complete model of actual baffled systems.

## REFERENCES

1. Swenson, L. S. Jr., Grimwood, J. M., and Alexander, C. C., *This New Ocean: A History of Project Mercury*, NASA SP-4201, 1966.
2. Hacker, B. C., and Grimwood, J. M., *On the Shoulders of Titans: A History of Project Gemini*, NASA SP-4203, 1977.
3. Bilstein, R. E., *Stages to Saturn: A Technological History of the Apollo/Saturn Launch Vehicles*, NASA SP-4206, 1980.
4. Brooks, C. G., Grimwood, J. M., and Swenson, L. S. Jr., *Chariots for Apollo: A History of Manned Lunar Spacecraft*, NASA SP-4205, 1979.
5. *Gemini Midprogram Conference*, Manned Spacecraft Center, Houston, Texas, NASA SP-121, 1976.
6. Douglass, H. W., *Liquid Rocket Engine Injectors*, NASA SP-8089, 1976.
7. Douglass, H. W., *Liquid Rocket Combustion Stabilization Devices*, NASA SP-8113, 1974.
8. Douglass, H. W., *Liquid Rocket Engine Nozzles*, NASA SP-8120, 1976.
9. Culick, F. E. C., and Yang, V., "Prediction of the Stability of Unsteady Motions in Solid-Propellant Rocket Motors," Chapter 18: *Nonsteady Burning and Combustion Stability of Solid Propellants*, Progress in Astronautics and Aeronautics, eds. L. DeLuca, E. Price and M. Summerfield, 1992.
10. Preklik, D., and Spagna, P., "Low Frequency and High Frequency Combustion Oscillation Phenomena inside a Rocket Combustion Chamber Fed by Liquid and Gaseous Propellants," presented at the 72nd Specialist's Meeting on Combustion Instabilities in Liquid-Fueled Propulsion Systems, Propulsion and Energetics Panel, AGARD, October 1988.

11. *Development History of the 200,000-225,000 lb Thrust J-2 Rocket Engines*, Final Report, Rocketdyne Report No. R-6700, December 1966.
12. Rubin, S., "Longitudinal Instability of Liquid Rockets due to Propellant Feedback (POGO)," *AIAA Journal of Spacecraft*, Vol. 3, No. 8, pp. 1188-1195, 1966.
13. Rubin, S., Wagner, R. G., and Rayne, J. G., *POGO Suppression on Space Shuttle—Early Studies*, NASA CR-2210, 1973.
14. Scala, S. M., *Transverse Wave and Entropy Wave Combustion Instability in Liquid Propellant Rockets*, Ph.D. Thesis, Princeton University, April 1957.
15. Reardon, R. H., "Analytical Models of Low and Intermediate Frequency Instability," Chapter 5, *Liquid Propellant Rocket Combustion Instability*, NASA SP-194, eds. D. T. Harrje and F. H. Reardon, 1972.
16. *Liquid Propellant Engine Manual Data Sheet* from Rocketdyne, A Division of North American Rockwell Corp., March 1966.
17. Male, T. and Kerslake, W. R., *A Method for Prevention of Screaming in Rocket Engines*, NASA-RM-E54F28A, 1954.
18. JANNAF Workshop on Liquid-Propellant Rocket Combustion Instability, Orlando, Florida, February 1990.
19. Oefelein, J. C. and Yang, V., *A Comprehensive Review of Liquid-Propellant Combustion Instabilities in F-1 Engines*, Technical Report, The Pennsylvania State University, 1992.
20. Wieber, P. R., *Acoustic Decay Coefficients of Simulated Rocket Chambers*, NASA-TN-D-3425, 1966.
21. Torda, T. P. and Patel, B. R., *Analytical and Experimental Investigation of Oscillations in Rocket Motor Baffle Cavities*, AFOSR-68-1369, 1968.

22. Hannum, N. P., Bloomer, H. E., and Goelz, R. R., *Stabilizing Effects of Several Injector Face Baffle Configurations on Screech in a 20,000 Pound-Thrust Hydrogen-Oxygen Rocket*, NASA TN D-4515, April 1968.
23. Vincent, D. W., Sokolowski, D. E. and Bloomer, H. E., *Injector Baffles for Flame Stability in Combustion Chambers Using Nitrogen Tetroxide and Hydrazine Mixture*, NASA-TM-X-1595, 1968.
24. Hefner, R. J., "Review of Combustion Stability Development with Storable Propellants," *Journal of Spacecraft*, Vol. 3, pp. 1046-1051, 1966.
25. Harrje, D. T. and Reardon, F. H., *Liquid Propellant Rocket Combustion Instability*, NASA SP-194, 1972.
26. Crocco, L. and Cheng, S. I., *Theory of Combustion Instability in Liquid Propellant Rockets*. AGARD No. 8, Butterworths Scientific Publications, London, 1956.
27. Oberg, C. L., Wong, T. L. and Schmeltzer, R. A., *Acoustic Behavior of Baffled Combustion Chambers*, NASA-CR-72625, 1970.
28. Oberg, C. L., Evers, W. H. and Wong, T. L., *Analysis of the Acoustic Behavior of Baffled Combustion Chambers*, NASA-CR-72879, 1971.
29. Lord Rayleigh, *The Theory of Sound*, Vol. II, Dover Publications, 1945.
30. Oberg, C. L. and Schuman, M. D., *Final Report: Further Analysis of the Effects of Baffles on Combustion Instability*, NASA-CR-134832, 1975.
31. Baer, M. R. and Mitchell, C. E., *Theoretical Evaluation of Rigid Baffles in the Suppression of Combustion Instability*, NASA-CR-134986, 1976.
32. Wicker, J., *Acoustic Wave-Induced Vortical Motions in Baffled Combustion Chambers*, Master Thesis, The Pennsylvania State University, 1993.

33. Crocco, L., Gray, J., and Harrje, D. T., "Theory of Liquid Propellant Rocket Combustion Instability and Its Experimental Verification," *ARS Journal*, Vol. 30, pp. 159-168, 1960.
34. Crocco, L., Harrje, D. T., and Reardon, F. H., "Transverse Combustion Instability in Liquid Propellant Rocket Motors," *ARS Journal*, Vol. 32, pp. 366-373, 1962.
35. Reardon, F. H., *An Investigation of Transverse Mode Combustion Instability in Liquid Propellant Rocket Motors*, Ph.D. Thesis, Princeton University, 1961.
36. Reardon, F. H., Crocco, L., and Harrje, D. T., "Velocity Effects in Transverse Mode Liquid Propellant Rocket Combustion Instability," *AIAA Journal*, Vol. 2, No. 9, pp. 1631-1641, 1964.
37. Oberg, C. L., Evers, W. H., Schuman, M. D., and Huebner, A. L., *Final Report: Analysis of the Effects of Baffles on Combustion Instability*, NASA CR-134614, 1974.
38. Levine, R. S., and Bambanek, R., *A Sustaining Mechanism for a Transverse Mode of Combustion Instability*, Rocketdyne Report No. R-326, 1956.
39. Peoples, R. G., and Pickford, R. S., *Analytical and Experimental Scaling of Thrust Chambers*, Aerojet-General Report TN-40 (AFOSR 677), 1960.
40. Sirignano, W. A. and Crocco, L., "A Shock Wave Model of Unstable Rocket Combustors," *AIAA Journal*, Vol. 2, No. 7, pp. 1285-1296, July 1964.
41. Crocco, L. and Mitchell, C. E., "Nonlinear Periodic Oscillations in Rocket Motors with Distributed Combustion," *Combustion Science and Technology*, Vol. 1, 1969.
42. Powell, E. A., *Application of the Galerkin Method in the Solution of Combustion Instability Problems*, Ph.D. Thesis, Georgia Institute of Technology, 1970.

43. Zinn, B. T. and Powell, E. A., "Nonlinear Combustion Instability in Liquid Propellant Rocket Engines," *Proceedings of the Thirteenth Symposium on Combustion*, The Combustion Institute, 1971.
44. Culick, F. E. C., "Nonlinear Growth and Limiting Amplitude of Acoustic Oscillations in Combustion Chambers," *Combustion Science and Technology*, Vol. 3, 1971.
45. Krylov, N. and Bogoliubov, N., *Introduction to Nonlinear Mechanics*, Princeton University Press.
46. Culick, F. E. C., "Nonlinear Behavior of Acoustic Waves in Combustion Chambers," *Acta Astronautica*, Vol. 3, pp. 715-734, 1976.
47. Yang, V. and Culick, F. E. C., "On the Existence and Stability of Limit Cycles for Transverse Acoustic Oscillations in a Cylindrical Combustion Chamber. 1: Standing Modes," *Combustion Science and Technology*, Vol. 72, pp. 37-65, 1990.
48. Kim, S. I., *Nonlinear Combustion Instabilities in Combustion Chambers*, Ph.D. Thesis, The Pennsylvania State University, 1989.
49. Marble, F. E., "Dynamics of a Gas Containing Small Solid Particles," *Combustion and Propulsion*, 5th AGARD Colloquium, Pergamon Press, pp. 175-213, 1963.
50. Marble, F. E., "The Dynamics of Dusty Gases," *Annual Reviews of Fluid Mechanics*, Vol. 2, pp. 397-446, 1970.
51. Priem, R. J. and Heidmann, M., "Propellant Vaporization as a Design Criterion for Rocket Engine Combustion Chambers," NASA TR R-67, 1960.
52. Crocco, L. and Sirignano, W. A., *Behavior of Supercritical Nozzles under Three-Dimensional Oscillatory Conditions*, AGARDograph 117, 1967.

53. DeSalvo, G. J., and Gorman, R. W., *ANSYS Engineering Analysis System. User's Manual*, Swanson Analysis System, Inc., 1989.
54. Rupe, J. H., *An Experimental Correlation of the Nonreactive Properties of Injection Schemes and Combustion Effects in a Liquid-Propellant Rocket Motor, Part V. The Influence of Vanes on Combustion and Combustion Stability*, JPL Tech. Rept. 32-255, September 1967.
55. McBride, J. M., Hewitt, R. A., and Hefner, R. J., "Acoustic Techniques for Injector Baffle Development," Bulletin of the 7th Annual Liquid Propellant Symposium, ICRPG Combustion Conference, CPIA Pub. No. 72, November 1967.
56. Yang, V., Kim, S. I., and Culick, F. E. C., "Triggering of Longitudinal Pressure Oscillations in Combustion Chambers. 1: Nonlinear Gasdynamics," *Combustion Science and Technology*, Vol. 72, pp. 183-214, 1990.



That is,

$$[\mathbf{G}][\mathbf{B}] = 0 \quad (\text{A.3})$$

For the non-trivial solution, the determinant of the matrix  $\mathbf{G}$  should be zero.

$$|\mathbf{G}| = 0 \quad (\text{A.4})$$

All elements of matrix  $\mathbf{G}$  are functions of frequency. Therefore, frequency can be determined from the frequency characteristic equation Eq. (A.4).